ABSTRACT

Title of Document: MODELING AND EXPERIMENTAL
ANALYSIS OF PHASED ARRAY
SYNTHETIC JET CROSS-FLOW
INTERACTIONS

Zohaib Hasnain, Doctor of Philosophy, 2014

Directed By: Professor Alison B. Flatau, Department of
Aerospace Engineering

Synthetic Jet Actuators (SJAs) are fluidic devices capable of adding momentum to static or non-static bodies of fluid without adding mass. They are therefore categorized as zero-net-mass-flux (ZNMF) momentum source. In its simplest compact form a SJA consists of an oscillatory surface connected to a cavity with a single exit orifice through which the fluid enters and exits. SJA technology has been utilized in applications ranging from boundary layer control over aerodynamic surfaces to fluidic mixing in dispersion applications. The ZNMF nature of the technology means it is not subject to constraints experienced by traditional momentum sources that require the addition of mass in order to impart momentum. The momentum that can be added by a single SJA is limited by the energy transfer capabilities of the oscillating surface. In modern SJAs this surface usually is a piezoceramic/metal composite subjected to a high voltage AC signal. For applications such as flow control over aerodynamic surfaces, modern SJAs are used in an array configuration and are capable of altering the flow

momentum by values ranging from 0.01-10%. While it is possible to build larger actuators to increase this value the benefits associated with the compact size would be lost. It is therefore desirable to tune other parameters associated with SJA arrays to increase this value. The specific motivation for this study comes from the desire to control the momentum addition capacity of a specific SJA array, without having to alter any geometric parameters. In a broader sense this study focuses on understanding the physics of SJA interaction in array configuration through experiments which are then used to guide in the design of modeling technique that predicts SJA array behavior in cross-flows.

The first half of the project focused on understanding SJA behavior through modeling. Numerical techniques were initially used to model SJA and SJA arrays in cross-flows. Reduced numerical models were then developed from the full momentum equations. Analytical methods to solve these reduced order models were then implemented in order to cut down on solution time. A wave equation based solution to the stream and vorticity formulation of the momentum equations was implemented to predict SJA behavior.

For the experimental component of the project, a finite span high aspect ratio orifice SJA was designed and characterized through Constant Temperature Anemometry (CTA). Two of these SJA were then placed in close proximity to one another. The relative phase of operation between the two jets was altered and the resulting flow field was measured through Particle Image Velocimetry (PIV). This process was repeated for different sets of array spacing, and SJA to cross-flow velocity ratio. For specific choices of these parameters a 40% increase in momentum addition was observed. The experimental results were used to validate the modeling techniques. In general reasonable agreement between the modeling and experiment was observed in specific domains of the flow field.

MODELING AND EXPERIMENTAL ANALYSIS OF PHASED ARRAY SYNTHETIC JET CROSS-FLOW INTERACTIONS

By

Zohaib Hasnain

Dissertation submitted to the Faculty of the Graduate School of the
University of Maryland, College Park, in partial fulfillment
of the requirements for the degree of
Doctor of Philosophy
2014

Advisory Committee:
  Professor Alison B. Flatau, Chair
  Professor James E. Hubbard, Jr.
  Professor Anya R. Jones
  Professor Kenneth T. Kiger
  Professor Allen E. Winkelmann

Dedication

To my mother and father.

Acknowledgements

First and foremost I would like to acknowledge and thank my parents and my family for their endless material and emotional support. Without their sacrifice my work would have been extremely hard to accomplish. My mother's unparalleled hard work was my motivation through some of the hardest hours I spent working on this project. My father's intellectual contributions were critical in helping my understanding the underlying mathematics involved. For their help and love, I will be forever grateful.

I would like to thank my friends and colleagues beginning with Lina Castaño. Her meticulous and extremely detailed way of analyzing things was invaluable to my project. I would also like to thank Andrew Hume Lind for assisting me at various stages of project. A special thanks to Jose Mondragon, Aaron Sassoon and Brian Pinto, who helped me at various stages of the experimental aspect of the project. Last but not least, I would like to acknowledge the help of Rose Weinstein, Vera Klimchenko, Ganesh Raghunath, David Mayo, Lauren Trollinger, Samatha Walters, Hana Viennu and Koji Yanaga amongst many others.

Of course no project can be completed without the support and guidance of the faculty advisor. I would therefore like to acknowledge the efforts and guidance of Dr. Alison B. Flatau whose guidance was instrumental throughout the entire process. I would also like to extend special thanks to Dr. James E. Hubbard Jr. for his unconditional support during and after the project. Dr. Hubbard's guidance was crucial for some of the most critical aspects of this project. I would like acknowledge and thank

Dr. Kenneth T. Kiger and Dr. Anya R. Jones for their advice as well as their generosity in agreeing to let me use their lab equipment for the experimental aspect of the project. Finally I would like to acknowledge the National Science Foundation for Award # 1031077 through which the project was made financially possible.

Table of Contents

Dedication ii
Acknowledgements iii
Table of Contents v
List of Tables viii
List of Figures ix
Chapter 1: Introduction 1
  1.1 Flow Control Overview 1
    1.1.1: Background and Definition 1
    1.1.2: Categories of Flow Control 2
  1.2 Flow Control through Synthetic Jet Actuators 3
    1.2.1: Synthetic Jet Actuator Overview 3
    1.2.2: Formation of a Synthetic Jet 4
    1.2.3: Evolution of a Synthetic Jet 5
  1.3 Synthetic Jet Applications and Motivation 11
    1.3.1: Separation Control 11
    1.3.2: Dynamic Virtual Shaping 13
    1.3.3: Other SJA applications and motivation 16
  1.4 Literature Review: Synthetic Jet Actuator modeling 17
    1.4.1: SJA Analytical Modeling: Previous studies and state of the art 17
    1.4.2: SJA Numerical Modeling: Previous studies and state of the art 19
  1.5 Literature Review: Synthetic Jet Actuator Experimental analysis 25
    1.5.1: Fundamental physics of SJA flow 25
    1.5.2: SJA cross-flow interactions 28
    1.5.3: SJA application based experiments and state of the art 30
    1.5.4 Summary of Literature Review 31
  1.6 Important Synthetic Jet and array parameters 32
    1.6.1: Single actuator operating and geometric parameters 32
    1.6.2: Array geometric and operational parameters 35
    1.6.3: Synthetic Jet non-dimensional parameters 36
  1.7 Objectives and organization of the dissertation 40
    1.7.1: Goal and objectives 40
    1.7.2: Organization of the dissertation 43
Chapter 2: Modeling Synthetic Jet Arrays interacting with cross-flow 46
  2.1 Introduction to modeling 46
    2.1.1: Modeling Approaches 46
    2.1.2: Modeling SJA: Selection of parameters 51
    2.1.3: Parameter space for modeling matrix 55
  2.2 Details of modeling techniques 56
    2.2.1: CFD Solution 56
    2.2.2: Perturbation Solution 65

    2.2.3: Analytical Solution ... 70
  2.3 Qualitative results from modeling: Flow features ... 79
    2.3.1: CFD prediction and analysis of flow features ... 79
    2.3.2: Perturbation prediction of flow features ... 93
    2.3.3: Analytical solution prediction of flow features ... 94
    2.3.4: Summary of qualitative analysis of modeling results ... 95
  2.4 Quantitative analysis of modeling results ... 96
    2.4.1: Quantifying the magnitude, direction and decay rate ... 96
    2.4.2: Quantitative analysis of the effects of Velocity Ratio (R) ... 100
    2.4.3: Quantitative analysis of the effects of Spacing (s) ... 103
    2.4.4: Quantitative analysis of the effects of Phasing (φ) ... 104
  2.5 Summary of modeling ... 110
Chapter 3: Design, Build and Characterization of a Synthetic Jet Actuator ... 112
  3.1 Developing SJA for model validation ... 112
    3.1.1: Design criteria ... 112
    3.1.2 Synthetic Jet Actuator design ... 112
  3.2 Characterization of synthetic jet actuators ... 117
    3.2.1: Frequency and voltage characterization of the synthetic jets ... 117
    3.2.2: Power Spectra analysis ... 122
  3.3 Summary of design and characterization process ... 125
Chapter 4: PIV Measurements for Model Validation and Flow Field Characterization ... 126
  4.1 PIV and experimental setup ... 126
    4.1.1: PIV specifics ... 126
    4.1.2: Experimental setup ... 127
  4.2 PIV vs CTA comparison of Synthetic Jet flow fields ... 129
    4.2.1: Comparison of velocities ... 130
    4.2.2: Comparison of frequency content ... 131
  4.3 PIV study of the 3 dimensionality of a SJA ... 134
  4.4 Model validation and flow analysis through PIV ... 136
    4.4.1: Validating model predictions of spacing effects ... 136
    4.4.2: Validating model predictions of velocity ratio effects ... 139
    4.4.3: Flow analysis and model validation of phasing and coupling effects ... 143
    4.4.4: Validation of modeling prediction for initial trajectory angles ... 150
    4.4.5: Dynamic virtual shaping through phasing ... 151
  4.5 Summary of model validation and experimental analysis ... 154
Chapter 5: Summary, Conclusions and Future Work ... 155
  5.1 Summary and conclusions ... 155
    5.1.1: Summary of contribution to the field ... 155
    5.1.2: Modeling summary and comparison, conclusions and limitations ... 157
    5.1.3: Experimental results and conclusions ... 162
  5.2 Future work ... 163
Appendices ... 167
  A1: Error analysis for PIV ... 167
  A2: Calculating array momentum coefficient from experimental data ... 168
Bibliography ... 170

List of Tables

Table 1 Rectangular orifice types 6
Table 2 Coarse parameter space matrix for modeling 55

List of Figures

Figure 1 Formation of a Synthetic Jet 5
Figure 2 Commonly used orifice geometries 5
Figure 3 Phase-locked schlieren images of the synthetic jet (xy) plane (Smith & Glezer, 1998) 9
Figure 4 Phase-locked schlieren images of the synthetic jet (xz) plane (Smith & Glezer, 1998) 10
Figure 5 Time averaged streamlines over an airfoil for (a) Unforced flow (b) Forced Flow $F^* = 0.5$ (c) Forced Flow $F^* = 1$ (Raju, et al., 2008) 13
Figure 6 Time averaged velocity vectors illustrating stationary recirculation domain created by passive object-synthetic jet interaction (Chatlynne, et al., 2001) 15
Figure 7 Schlieren flow visualization of synthetic jet actuator array operating (a) In-phase (b) Out of phase with right actuator leading by 60 degrees (Smith & Glezer, 2005) 15
Figure 8 Velocity contours for an SJA (Left) Laminar flow model prediction (Right) Turbulent flow model prediction (Kral, et al., 1997) 20
Figure 9 Vorticity contours illustrating vortex switching (Li & Sahni, 2014) 23
Figure 10 Contour maps of velocity in the yz-plane at (a) $x/b = 19.7$ (b) $x/b = 39.4$ (c) $x/b = 78.7$ first contour at $1 m/s$, increments of $0.5\ m/s$ (Smith & Glezer, 1998) 27
Figure 11 CAD drawings depicting actuator geometric parameters 34
Figure 12 Schematic illustrating array parameters with excitation voltage to SJA1 (upstream actuator) shown lagging excitation voltage to SJA2 36
Figure 13 SJA numerical modeling domains 47
Figure 14 Comparison of jet trajectory analytical prediction with experimental data (Ugrina, 2007) 51
Figure 15 Parameter space for modeling 54
Figure 16 Simulated domain dimensions and coordinate system (illustration only not to scale) 58
Figure 17 Mesh schematic with boundary conditions 60
Figure 18 Time averaged velocity history at $x = 0$, $y = 5b$ 62
Figure 19 Vorticity contours for simulated case $R = 2.4$, $\varphi = 0$, $s = 2.5$ b at $t/T = 56$ and element growth rate of 1.1 63
Figure 20 Vorticity contours for simulated case $R = 2.4, \varphi = 0, s = 2.5\ b$ at $t/T = 56$ and element growth rate of 1.05 64
Figure 21 Vorticity contours for simulated case $R = 2.4, \varphi = 0, s = 2.5\ b$ at $t/T = 56$ and element growth rate of 1.01 65
Figure 22 Mesh and boundary conditions for perturbation model 70
Figure 23 Least squares fit of a hyperbolic cosine to experimental velocity at height $y = 20\ b$ (Smith & Glezer, 1998) 75
Figure 24 Schematic of ideal boundary conditions and interaction domain for analytical model 77
Figure 25 Modified boundary conditions used for analytical modeling 77
Figure 26 Plot of the ideal boundary condition along $y = 0$ for $s = 2.5b$, $\varphi = 0$, and $t/T = 0.0560$ (No dependency on velocity ratio, R) 78

Figure 27 Plot of the $\boldsymbol{v}$ velocity for modified boundary condition along $y = 0$ for $s = 2.5b$, $\varphi = 0$, and $t/T = 0.0560$ ($\theta = 30°$ obtained from PIV; magnitude dependency on R) 78
Figure 28 Plot of the $\boldsymbol{u}$ velocity for modified boundary condition along $y = 0$ for $s = 2.5b$, $\varphi = 0$, and $t/T = 0.0560$ ($\theta = 30°$ obtained from PIV; magnitude dependency on R) 79
Figure 29 Vorticity contours for single SJA @ $t/T = 0.25$ (midway through ejection cycle) 81
Figure 30 Vorticity contours for single SJA @ $t/T = 0.52$ (beginning of suction phase) 81
Figure 31 Vorticity contours for single SJA @ $t/T = 0.94$ (close to the end of the ejection cycle) 83
Figure 32 Vorticity contours for single SJA @ $t/T = 1.23$ 83
Figure 33 Vorticity contours for single SJA @ $t/T = 2.25$ 84
Figure 34 Vorticity contours for single SJA @ $t/T = 37.52$ 84
Figure 35 Vorticity contours for single SJA @ $t/T = 37.68$ 85
Figure 36 Vorticity contours for single SJA @ $t/T = 38.26$ 86
Figure 37 Vorticity contours for dual SJA operating in phase @ $t/T = 78.28$ 87
Figure 38 Vorticity contours for dual SJA operating in phase @ $t/T = 78.40$ 88
Figure 39 Vorticity contours for dual SJA operating in phase @ $t/T = 78.51$ 89
Figure 40 Vorticity contours for dual SJA operating in phase @ $t/T = 78.95$ 90
Figure 41 Vorticity contours for dual SJA operating at $\varphi = 30°$ @ $t/T = 78.28$ 91
Figure 42 Vorticity contours for dual SJA operating at $\varphi = 30°$ @ $t/T = 78.45$ 92
Figure 43 Vorticity contours for dual SJA operating at $\varphi = 30°$ @ $t/T = 78.89$ 92
Figure 44 Vorticity contours for dual SJA operating at $\varphi = 30°$ @ t/T = 79.22 93
Figure 45 Vorticity contours as predicted through numerical perturbation method for dual SJA operating at $\varphi = 30°$ @ $t/T = 78.30$ 94
Figure 46 Velocity contours as predicted by analytical solution to perturbation method for dual SJA operating at $\varphi = 30°$ @ $t/T = 78.30$ 95
Figure 47 Depiction of jet centerline trajectory and reference coordinate system 97
Figure 48 PIV measured Decay of velocity along centerline trajectory for $R = 2.4$, $\varphi = -120°$ and $s = 2.5b$ 98
Figure 49 Modeling predictions for jet centerline trajectory for $R = 2.4$, $s = 2.5b$ and $\varphi = 0°$ 100
Figure 50 Modeling predictions for jet centerline trajectory for $R = 0.95$, $s = 2.5$b and $\varphi = 0°$ 101
Figure 51 CFD predictions for jet centerline trajectory for $R = 0.95$ & 2.4, $s = 2.5b$ and $\varphi = 0°$ 102
Figure 52 CFD predictions of normalized velocity decay for $R = 0.95$ & 2.4, $s = 2.5b$ and $\varphi = 0°$ 102
Figure 53 CFD predictions for jet centerline trajectory for $R = 2.4$, $s = 2.5b$ and $4.5b$, $\varphi = 0°$ 103
Figure 54 CFD predictions of normalized velocity decay for $R = 2.4$, $s = 2.5b$ and $4.5b$, $\varphi = 0°$ 104
Figure 55 CFD and Perturbation predictions of momentum coefficient for $R = 2.4$, $s = 2.5b$ and $\varphi = 0°$ 105

Figure 56 Modeling predictions for jet centerline trajectory for $R = 2.4$, $s = 2.5b$ and $\varphi = -180°$ 106
Figure 57 Modeling predictions for jet centerline trajectory for $R = 2.4$, $s = 2.5b$ and $\varphi = -120°$ 107
Figure 58 Modeling predictions for jet centerline trajectory for $R = 2.4$, $s = 2.5b$ and $\varphi = -60°$ 107
Figure 59 Modeling predictions for jet centerline trajectory for $R = 2.4$, $s = 2.5b$ and $\varphi = 0°$........ 108
Figure 60 Modeling predictions for jet centerline trajectory for $R = 2.4$, $s = 2.5b$ and $\varphi = 60°$........ 109
Figure 61 CFD predictions of normalized velocity decay for $R = 2.4$, $s = 2.5b$, $\varphi = -120°$ and 0°........ 110
Figure 62 External dimensions of the synthetic jet actuator........ 113
Figure 63 Internal dimension of synthetic jet actuator 114
Figure 64 Synthetic jet actuator assembly 115
Figure 65 Piezo ceramic brass disc used as driver for Synthetic Jet Actuators........ 116
Figure 66 Assembled array of two Synthetic Jet Actuators........ 117
Figure 67 CTA frequency characterization setup 119
Figure 68 Frequency response of synthetic jet actuators........ 119
Figure 69 Voltage response for actuator characterization at $f = 1120$ Hz........ 122
Figure 70 Frequency content analysis of CTA measured velocity 2 mm above the orifice 123
Figure 71 Frequency content analysis of CTA measured velocity 4 mm above the orifice 124
Figure 72 Frequency content analysis of CTA measured velocity 8 mm above the orifice 124
Figure 73 Convergence of the residual of the sum of time averaged velocities for the flow field........ 127
Figure 74 Schematic of wind tunnel showing direction of flow, test section and coordinate system........ 128
Figure 75 Expanded view of test section showing laser sheet, PIV camera and actuators 128
Figure 76 Illustration of PIV field of view and actuator setup 129
Figure 77 Comparison of RMS velocities measure by CTA (hotwire) vs. PIV 130
Figure 78 Frequency analysis of PIV data obtained at 2 mm above the orifice (red line indicates average magnitude)........ 132
Figure 79 Frequency analysis of PIV data obtained at 4 mm above the orifice (red line indicates average magnitude)........ 132
Figure 80 Frequency analysis of PIV data obtained at 8 mm above the orifice (red line indicates average magnitude)........ 133
Figure 81 Time averaged velocity vector and magnitude plot (*yz*-plane along the span of the orifice)........ 134
Figure 82 *z*-component of time averaged PIV velocity at varying locations........ 135
Figure 83 PIV validation of predicted jet centerline trajectories with PIV for $R = 2.4$, $s = 2.5b$, $\varphi = 0°$........ 136

Figure 84 PIV validation of predicted jet centerline trajectories with PIV for R = 2.4, s = 4.5b, φ = 0° 137
Figure 85 Perturbation predictions for jet centerline trajectory for R = 2.4, s = 2.5b and 4.5b, φ = 0° 139
Figure 86 PIV validation of predicted jet centerline trajectories with PIV for R = 0.95, s = 2.5b, φ = 0° 140
Figure 87 Velocity decay predictions and PIV measurements R = 2.4, s = 2.5b and φ = 0° 141
Figure 88 Velocity decay predictions and PIV measurements R = 0.95, s = 2.5b and φ = 0° 142
Figure 89 Momentum coefficient validation and analysis R = 2.4 & s = 2.5b 143
Figure 90 Model validation and flow field analysis for phasing effects φ = -180° .. 146
Figure 91 Model validation and flow field analysis for phasing effects φ = -120° .. 146
Figure 92 Model validation and flow field analysis for phasing effects φ = -60° 147
Figure 93 Model validation and flow field analysis for phasing effects φ = 0° 147
Figure 94 Model validation and flow field analysis for phasing effects φ = 60° 148
Figure 95 Modeling predictions vs. experimental results for initial jet trajectory deflection angle 150
Figure 96 Streamlines for R = 2.4, s = 2.5b and φ = (a) -120° (b) 0° and (c) 120° .. 153

Chapter 1: Introduction

1.1 Flow Control Overview

1.1.1: Background and Definition

Flow Control can be described as: “An attempt to alter the character or disposition of a flow field favorably” (Gad-el-Hak, 2000). Some specific definitions of the term exist based on specific flow types, for instance Flatt’s definition pertaining to wall bounded flows states: “Boundary Layer Control includes any mechanism or process through which the boundary layer of the fluid is caused to behave differently than it normally would were the flow developing naturally along a smooth straight surface” (Flatt, 1961). Flow control was introduced in the early 1900s in the form of boundary layer theory when it was used to explain and modify the mechanics of steady separation. Modern flow control was first implemented the 1950s in the form of laminar flow control created through boundary layer suction. It was first used to delay transition on the swept wing of the X-21 up to a chord Reynolds number of 4.7×10^7. Since then it has been suggested and researched for a variety of applications, which range from construction of super-maneuverable fighter planes, to the need of controlling emissions of greenhouse gases. Pre-determined flow control refers to application of steady or unsteady energy input, without regard to the particular state of flow. This is a well suited technique for inducing change in a flow of known and or steady character (such as boundary layer removal through suction). However for any aerodynamic surface that undergoes a range of conditions, one would desire a more adaptable, controlled system.

It is therefore important to understand the physics of the interaction of the flow control system with the surrounding flow.

1.1.2: Categories of Flow Control

Flow control techniques can be divided into two major categories: passive management and active control. Passive techniques are defined as methods requiring no auxiliary power, or no control loop. Passive methods are designed for a very particular objective and require no power. They cannot adapt to the changing flow conditions and are therefore are ineffective and sometimes even detrimental at off-design condition. Examples of passive management include large-eddy breakup devices such as riblets (small flow-aligned grooves), which can be used to delay flow separation, and reduce viscous drag, over aerodynamic surfaces. They work by severing or altering the large vortices that form the convoluted outer edge of a turbulent boundary layer. Active control usually requires some sort of control loop, or at the least some form of power input. Examples of active flow control include steady boundary layer control (BLC) techniques, such as removal through suction and unsteady BLC techniques, such as the periodic addition of momentum with SJAs. A significant number of modern aircraft have been built, which convincingly demonstrates the effectiveness of steady BLC such as Lockheed's F-104 and the MIG-21 (Greenblatt & Wygnanski, 2000). However these steady methods of active flow control systems have an unusually high cost of energy input and inert mass associated with them. The boundary layer removal technique used on the MIG-21 for instance requires auxiliary compressor or excessive compressor bleed in order to function. Also the associated plumbing system adds considerable complexity and weight. In comparison to steady methods, momentum addition through periodic excitation can be achieved at relatively low input energy-inert mass cost.

1.2 Flow Control through Synthetic Jet Actuators

1.2.1: Synthetic Jet Actuator Overview

Advances in smart materials such as piezoceramics now allow for a much more compact/efficient method of adding energy to the flow. Synthetic Jet Actuators (SJAs) are compact fluidic devices consisting of an oscillating surface embedded in a cavity that can add energy at critical locations to any relevant flow. They provide a method of periodic addition of energy to the flow. In fact it has been shown that periodic addition of energy can attain the same degree of control authority as is achieved by steady energy input, with an important difference: The cost of unsteady methods is less than that of steady methods, in some instances this difference is observed to be an order of magnitude (Wygnanski, 1997). Ingard first discovered in the 1950s that connecting a cavity with an exit orifice at one end to a source of acoustic waves at the other end results in the emergence of a steady stream of fluid from the orifice (Ingard & Labate, 1950). With the advent of low cost mass commercialization of smart structures over the last few decades, the modern form of synthetic jet actuators has become a viable method of flow control for many applications. In modern flow control applications, SJAs are used in two different modes. For fully attached high momentum flows over aerodynamic bodies, operating SJAs at frequencies significantly higher than any frequency associated with any feature of the flow results in formation of recirculation regions. This mode is useful for applications such as fluidic mixing or virtually altering the path taken by the fluid around the body (Glezer, 1998). For low momentum flows that are about to undergo separation, actuation at frequencies similar to those of the unforced flow structures results in a delay of the separation (Hassan, 2005).

1.2.2: Formation of a Synthetic Jet

The concept of creating a turbulent shear flow through controlled coalescence of its fundamental coherent vertical structures e.g., turbulent spots in a transitional boundary layer or vortex rings in a round jet was proposed by Coles in the early seventies and was later tested in a flat plate boundary layer experiment **(Savas & Coles, 1985)**. While in their boundary layer experiments, turbulent spots were triggered by hairpin vortices induced by the periodic protrusion of a spanwise array of small pins into the flow, in general, synthetic jets are characterized by the formation and interaction of discrete vortical structures which are formed by time-periodic ejection of fluid out of an orifice at the flow boundary. Jet flows without net mass addition can be produced by an oscillatory flow having a zero time-averaged mean velocity through an orifice, provided that the amplitude of oscillations is large enough to induce flow separation at the orifice and the time-periodic rollup of a train of vortices. This mechanism is depicted in

Figure **1**. Upon expulsion a slug like mass of fluid surrounded by discrete vortical structures is ejected from the orifice. If the ejection velocity is sufficient, this mass detaches from the body of fluid inside the cavity and propagates away from the orifice. The cavity then draws in low momentum (or stationary) fluid from its immediate surroundings and the process starts over.

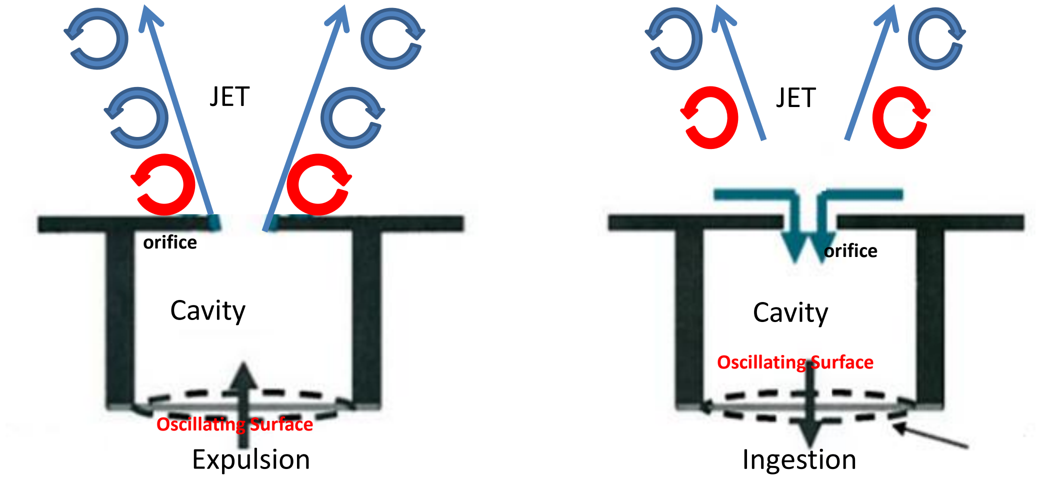

Figure 1 Formation of a Synthetic Jet

1.2.3: Evolution of a Synthetic Jet

The formation of a synthetic jet is characterized by a train of central masses of fluid propagating away from the orifice surrounded by vortices. The evolution of the flow field in regions close to and far away from the orifice is highly dependent on the orifice geometry (Vasile & Amitay, 2013). Orifice geometries for synthetic jets vary based on application and other constrains however in general can be broadly divided into the categories of high and low aspect ratio. Both categories cover all geometries such circular (ellipse of aspect ratio 1), elliptic (small to high aspect ratio possible) and rectangular (also, small to high aspect ratio possible).

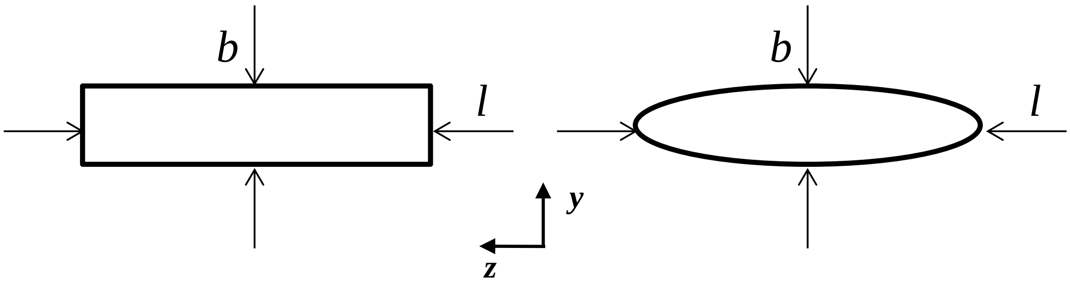

Figure 2 Commonly used orifice geometries

In general rectangular high aspect ratio rectangular geometries tend to lead to flow fields that are 2D dimensional in nature within some vicinity of the orifice. The exact extent of this region depends on the exact aspect ratio but in general for aspect ratios of above 20 we observe a 2D flow field up to a height of about 20 orifice widths **(Hasnain, et al., 2013)**. For a rectangular orifice, the physics of the flow is closely tied to the aspect ratio. The aspect ratio is defined as the ratio of the orifice width (*b*) to the orifice length (*l*). For rectangular orifice three sub-categories can be defined based on the range of the aspect ratio **(Sahni, et al., 2011)**. These categories are shown in Table 1. For the purposes of this study the geometries were generally limited to rectangular, finite span high aspect ratio.

Aspect Ratio (*b/l*)	**Orifice Type Description**
< 10	Low Aspect Ratio
$75 > b/l \geq 20$	Finite Span High Aspect Ratio
≥ 75	High Aspect Ratio

Table 1 Rectangular orifice types (based on (Sahni, et al., 2011))

The development and evolution of a synthetic jet issuing from this specific type of orifice is characterized by a core of steady flow surrounded by a pair of symmetric vortices. Understanding the formation and evolution of these vortex pairs is the first step in predicting how a jet will interact with another jet, or any other surrounding body of fluid. The evolution of the synthetic jet can be divided into two distinct domains.

Near the jet orifice, the flow is dominated by the periodic formation and advection of the vortex pairs which then undergo transition to turbulence, slowing down in the process as they lose their coherence. This transition process is followed by the second domain. Here we observe the emergence of a fully-developed turbulent jet which is similar in some respects to a conventional 2D jet (Smith & Glezer, 1998).

The formation of a synthetic jet as observed by Smith and Glezer (Smith & Glezer, 1998) is shown in a sequence of phase locked schlieren images in Figure 3 each of which are taken phase-locked to the actuator driving signal at 27 equal time intervals 33.8 μs apart during the oscillation cycle. The time period associated with a complete cycle of membrane oscillation, T, is 877 μs. The images are at acquired at the mid-span location (l / 2) of the orifice. The sequence begins with the expulsion motion of the actuator diaphragm ($t / T = 0$) which results in the ejection of fluid from the jet cavity. The coordinate system they used is shown for reference in the image corresponding to $t / T = 0.481$ (repeated on the bottom right hand side for reference). The streamwise distance, x, is normalized by orifice width b. While the images in Figure 1.3 are phase locked to the actuator's driving signal, the video frame rate is a submultiple of the actuation frequency, and therefore successive images do not show the same vortex pair. The front end of the fluid slug that is ejected out of the orifice and leads to the formation of the vortex pair is apparent on the left at time $t / T = 0.11$. Some traces of the previous vortex pair are still discernible near $x / b = 11$ and the emerging turbulent jet is visible farther downstream. In subsequent images ($0.15 < t / T < 0.41$), the new vortex pair continues its rollup as it is moves downstream while the previous vortex pair becomes indistinguishable from the background flow and is no longer phase locked to the excitation signal. The newly formed vortex pair and the remainder of the ejected fluid behind it appear to be laminar after the rollup process is completed and while the vortex core is advected through $x / b = 8.5$ ($t / T = 0.407$). The cores of the vortex pairs begin to exhibit small scale motions and undergo transition to turbulence around $t / T = 0.5$ which is accompanied by a reduction in their advection velocity. This transition process begins with the development and quick amplification of a spanwise instability of each primary vortex that leads to the formation of spanwise (along the length of the orifice) counter-rotating streamwise vortex pairs that are wrapped around the cores of the primary vortices and ultimately lead to a disintegration of their cores as shown in the spanwise view of the process in Figure 1.4.

The images in Figure 1.4 (a) - (d) show a spanwise section of the jet that is approximately 30 b wide at $z = 0$ and are captured at $t / T = 0.5$, 0.625, 0.75, and 0.875, respectively. Figure 1.4 (a) shows a new spanwise vortex on the left and the previous vortex which is in the final stages of the breakdown process. The image clearly shows the formation of spanwise periodic rib shape secondary vortical structures connecting the core of the primary vortices on the left with an average spanwise spacing of 2.5b. As the primary vortex is advected downstream in Figure 1.4 (b), for $t / T = 0.625$ and Figure 1.4 (c), for $t / T = 0.75$, the secondary vortical structures intensify and very quickly appears to lead to the disintegration of the core of the primary vortex shown Figure 1.4 (d), $t / T = 0.875$.

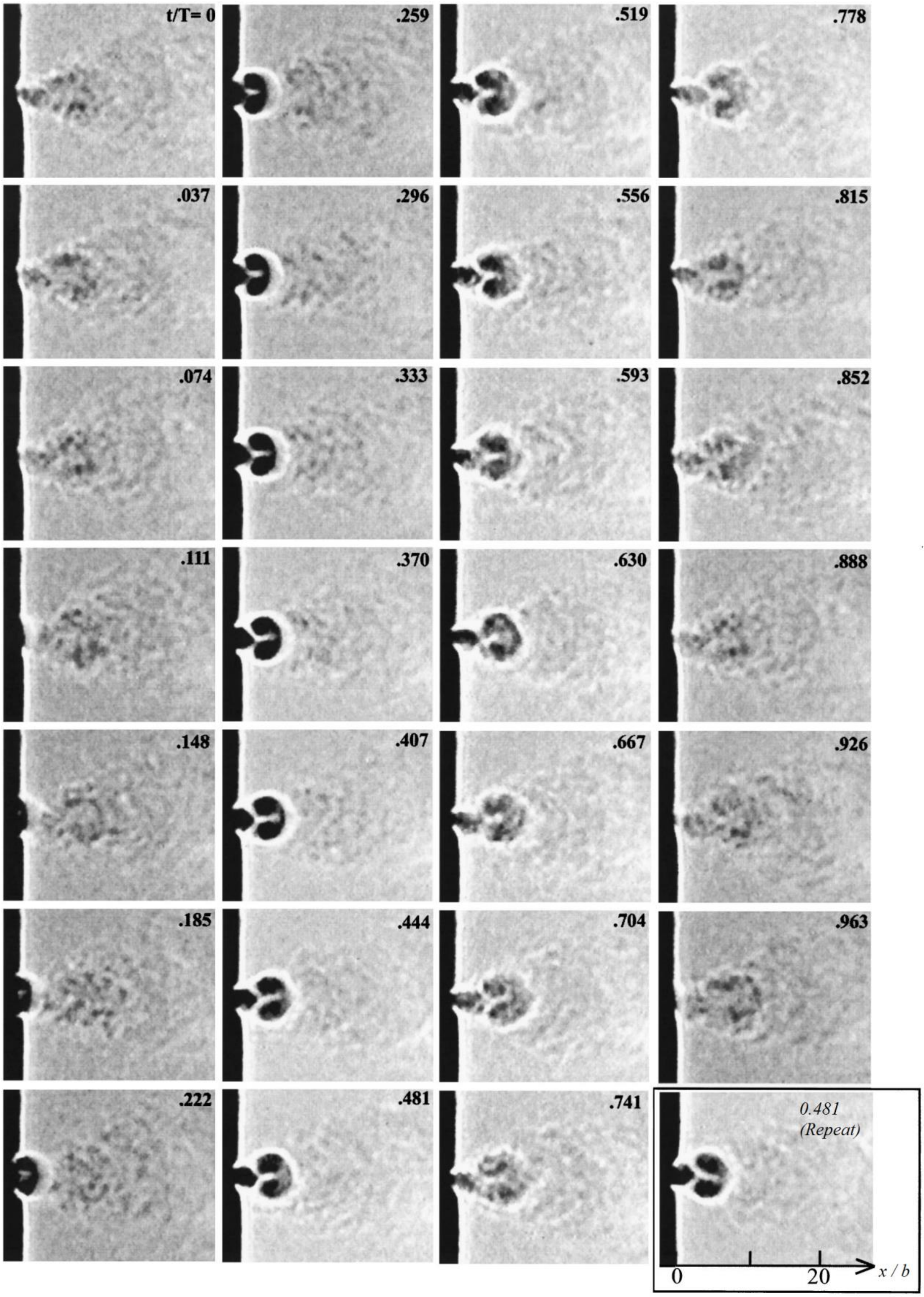

Figure 3 Phase-locked schlieren images of the synthetic jet (*xy*) plane (Smith & Glezer, 1998)

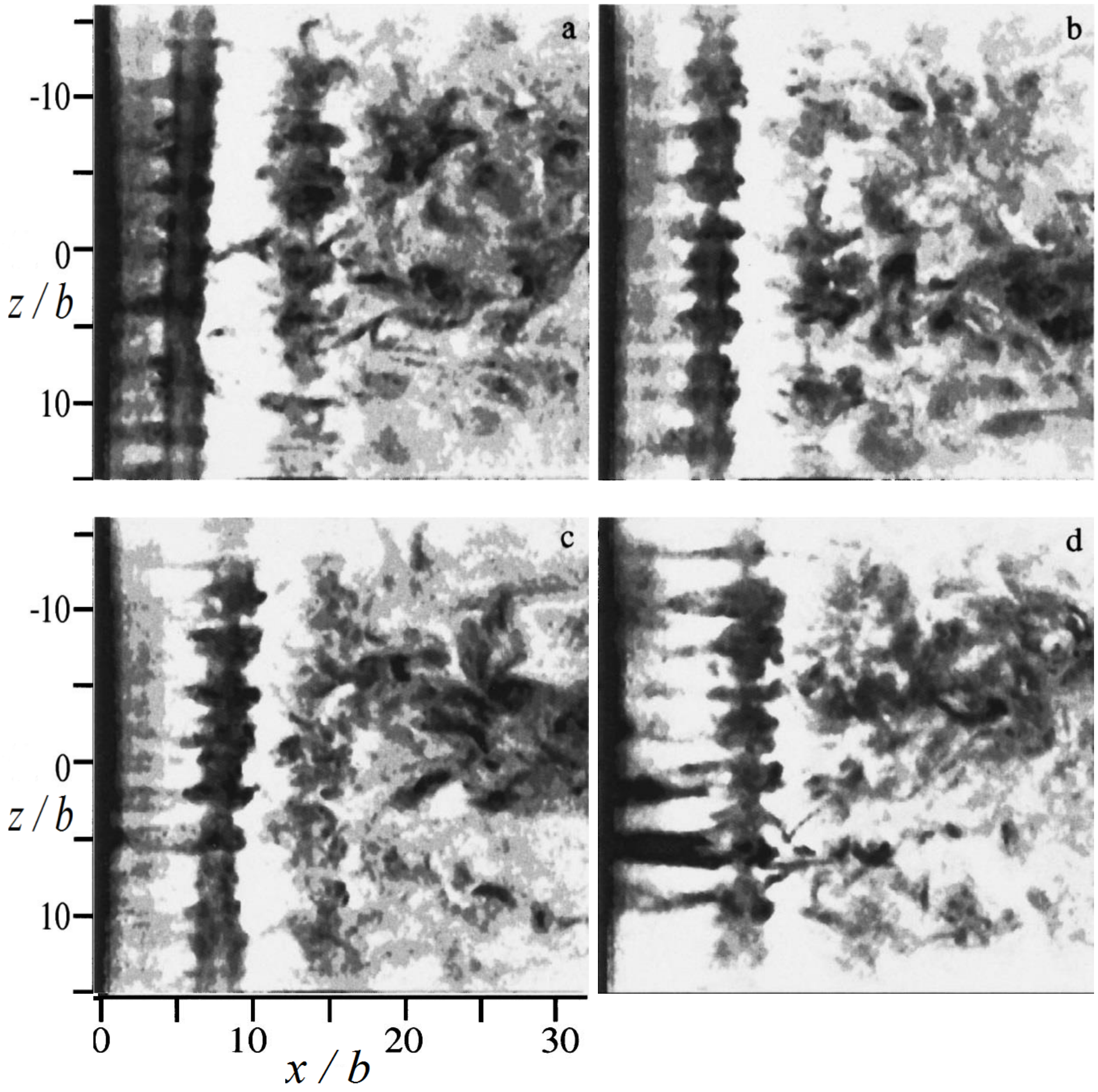

Figure 4 Phase-locked schlieren images of the synthetic jet (*xz*) plane (Smith & Glezer, 1998)

The formation, evolution and eventual decay of both streamwise and spanwise structures is responsible for the transition of the synthetic jet from a laminar fluid flow (surrounded by vortex pairs) to a highly turbulent 2D jet. The production of these structures is in turn dependent on the geometry of the exit orifice and the jet exit velocity. For this study the geometry of the exit orifice is generally fixed as high aspect ratio finite span. However performance parameters associated with jet operation are studied as parameters contributing to the results of the end goal. These parameters will be discussed in subsequent sections.

1.3 Synthetic Jet Applications and Motivation

1.3.1: Separation Control

A synthetic jet actuator is a zero net mass flux device that is capable of adding momentum to a body of fluid. Since SJAs provide a periodic unsteady method of excitation they can add energy to fluid at a cost that is much lower than that of steady momentum addition techniques. In some cases this difference can be as much as an order of magnitude (Greenblatt & Wygnanski, 2000). Modern SJAs are compact devices (Hasnain, et al., 2012; Bottomley & Packwood, 2014; Bhatt, et al., 2014; Jabbal, et al., 2013) that weigh less than more complex steady flow control systems having similar performance characteristics. This is mainly due to the fact that they do not require plumbing and a separate source to create the flow. Due to this major advantage SJAs are a well-studied solution to the problem of separation control of aerodynamic bodies. SJA have been applied to scale as well as full size flight tested wings, and have been shown to have a significant impact on drag and stall limits. Studies conducted at Georgia Tech and other institutions successfully used SJA to delay the onset of separation. They also used separation control to induce rolling moments on a swept wing UAV at angles of attack of 15° and above (Amitay, et al., 2004). Poisson-Quinton (Poisson-Quinton, 1948) demonstrated that the key principle for separation control is momentum addition to the boundary layer. One of the important dimensionless parameter used in quantifying momentum addition is the momentum coefficient, C_μ, this will be discussed in detail in subsequent sections. It is essentially a ratio of the actuator momentum flux to cross-flow momentum flux. Poisson-Quinton also showed that the critical value of C_μ beyond which the control mechanism changes from boundary layer to circulation based is 5% meaning that for the separation control application, operating actuators at their peak output velocity may not be appropriate. The largest values of $\frac{dC_L}{dC_\mu}$ (change in lift coefficient with respect to momentum coefficient) were observed when C_μ was less than 5%. Another important parameter in determining the type of application a specific SJA is suited to, is the non-dimensional frequency, *F**, (also to be discussed in detail in subsequent sections). *F** is the ratio of the actuation frequency to the frequency associated with any relevant instability in the flow (e.g. vortex shedding or shear layer mixing). An *F** value of around 1 is considered ideal for purposes of separation control. This result is confirmed by detailed analysis performed by Raju et al. (Raju, et al., 2008) who used numerical simulations to predict flow over an airfoil at an angle of attack of 18°. They concluded that there are three noteworthy characteristics about structure of the uncontrolled flow over the airfoil; the shear layer, the separation bubble and the wake region. By performing actuation at frequencies closer to natural shedding frequencies associated with each of these structures, they observed a significant change in aerodynamic performance. The most noticeable and positive response was obtained when the forcing frequency was closer to the separation bubble shedding frequency. They also concluded that the most adverse case of separation was seen when the actuation was performed close to frequencies associated with the shear layer. In most cases this actually caused an early onset of separation. Time averaged streamline results obtained as part of their study are shown in Figure 5.

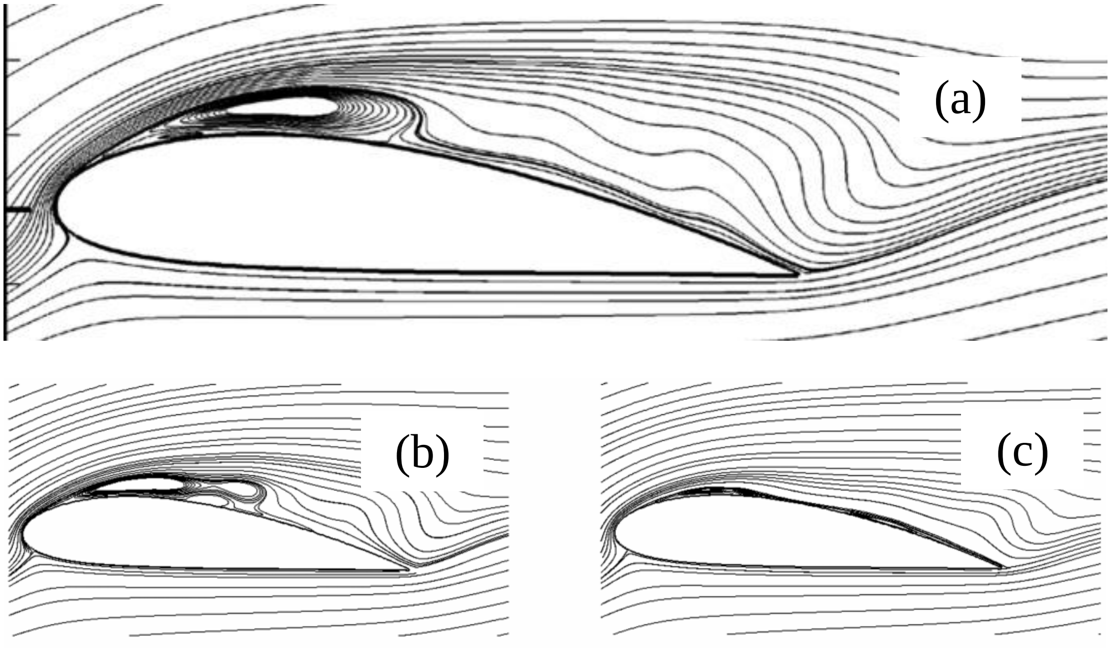

Figure 5 Time averaged streamlines over an airfoil for (a) Unforced flow (b) Forced Flow F* = 0.5 (c) Forced Flow F* = 1 (Raju, et al., 2008)

More recent studies involving the use of SJAs for separation control include work done by Rathay (Rathay, et al., 2014) who used SJA for separation control on aircraft tail rudder, Bottomley (Bottomley & Packwood, 2014) who studied the effect of actuation on a NACA0015 airfoil, and Tang (Tang, et al., 2014) who demonstrated lift improvement on different airfoil sections through actuation.

1.3.2: Dynamic Virtual Shaping

The other major application of SJA is virtual shaping of aerodynamic bodies. The idea of using flow control to create virtual aerodynamic shape change to induce a desired pressure distribution was first analyzed in the 1940s and 1950s. Perkins & Hazen were the first to demonstrate increased lift at zero angle of attack using a stationary, trapped vortex that virtually changed the local surface curvature (Perkins & Hazen, 1953). When interacting with an external cross flow (under very specific circumstances) a SJA can create a virtual shape change by generating a recirculation region near the jet orifice (Glezer, 1998). To the local streamlines, this region would appear as a new physical boundary, substantially modifying the flow field around the aerodynamic lifting surface thus changing its aerodynamic behavior.

Current mechanical systems used on aircraft and other aerodynamic bodies have complexity and weight associated with the control surfaces. Under very specific circumstances SJA activity can change the pressure distribution in a desired way. Chatlynne et al. (Chatlynne, et al., 2001) first demonstrated the capability of a single synthetic jet actuator to induce a desired shape change. By situating a SJA downstream of a passive obstruction, they were able to create a stationary recirculation domain downstream of the orifice. The streamlines of the cross-flow were deflected over this region effectively changing the pressure distribution on the airfoil. An illustration of this effect is shown in Figure 6. By varying the location of the SJA with respect to the passive obstruction, they were able to alter the induced pressure distribution. While their study demonstrates the ability to locally shape an airfoil, in order to be able to dynamically alter the global flow, it is desirable to have control over how and where the SJA injects momentum. With a single SJA the extent of this flexibility is limited to control over the magnitude of the output velocity (by adjusting the jet operating power). However, with an array of two or more actuators we can achieve control over the direction and location of the added momentum as well as its magnitude. This effect was first demonstrated by Smith and Glezer (Smith & Glezer, 2005). Schlieren image visualization showing the ability to vector SJA array flow is presented in Figure 7.

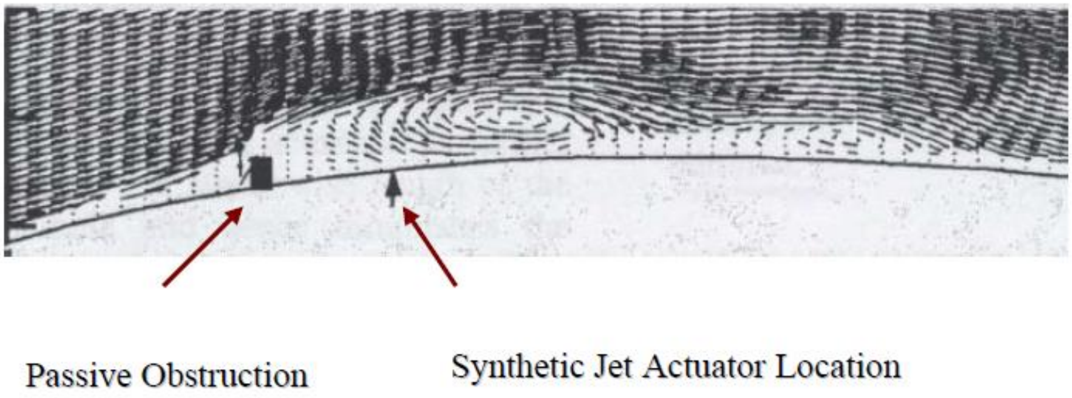

Figure 6 Time averaged velocity vectors illustrating stationary recirculation domain created by passive object-synthetic jet interaction (Chatlynne, et al., 2001)

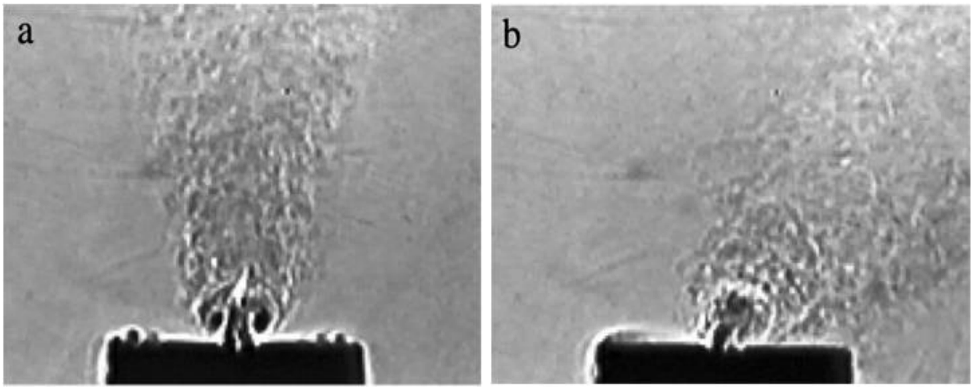

Figure 7 Schlieren flow visualization of synthetic jet actuator array operating (a) In-phase (b) Out of phase with right actuator leading by 60 degrees (Smith & Glezer, 2005)

Studying the ability to control the magnitude and direction of momentum for an SJA array is one of the objectives of this study. It will be discussed in detail in subsequent sections. The studies referenced in this section are a foundation upon which a major aspect of this study is built.

Virtual shaping using SJA has been studied in great detail. Some of the more modern applications include work done by Sassoon et al. (Sassoon, et al., 2013) who demonstrated the ability of SJA to alter the pressure distribution over backward facing step in a cross-flow. More recently Feng and Wang (Feng & Wang, 2014) demonstrated the ability of SJA to alter the flow over a cylinder changing its lift and drag properties.

1.3.3: Other SJA applications and motivation

SJAs have been used for a variety of applications that range from mixing control to acoustic noise reduction. Due to advancements in technology and availability of smart materials, SJA they are now being applied to a broader spectrum of fluid dynamics. In 2014, Jin et al. (Jin, et al., 2014) demonstrated how SJA can be used to alter the cooling rate of flat plate, therefore reducing the rate at which ice developed on the surface of the plate. Zelenyak et al. (Zelenyak, et al., 2013) reduced noise produced by turbulent steady jet by surrounding the periphery of the exit orifice with 8 synthetic jet actuators and performing actuation at specific frequencies. Xia and Zhong (Xia & Zhong, 2014) demonstrated that SJA can be used to enhance mixing of two laminar, parallel streams of water. Mahalingam et al. (Mahalingam, et al., 2013) recently demonstrated that SJA can be used to replace conventional cooling components with moving parts such as fans. LiQun and LiHao (LiQun & LiHao, 2013) applied synthetic jet actuators at stagnation points on a cylinder (bluff-body) under the influence of the cross-flow and demonstrated control over vortex shedding by altering the frequency of actuation.

The motivation for studying arrays of synthetic jet actuators comes from analyzing all the applications discussed above and in previous sections. All these applications revolve around using synthetic jet actuators as point design devices. In other words the behavior, location and other characteristics of the SJA are tuned so that they provide positive effect for a very narrow range of operating conditions. Operating the SJA with these tuned parameters under flow conditions different from those which the system was optimized for, could lead to detrimental effects. With a single SJA control is limited to the magnitude and frequency of the excitation, limiting the number of parameters available to circumvent the point design constraint. By using an array of synthetic jet actuators, as will be demonstrated by this study, one can control and increase the magnitude of the momentum added to the cross-flow. In addition to this the direction can also be altered (allows for dynamic virtual shaping) as well as the rate at which the added momentum decays. This observation is one of the cornerstones of this study and provides the motivation behind studying the interaction of arrays of synthetic jets with cross-flows.

1.4 Literature Review: Synthetic Jet Actuator modeling

1.4.1: SJA Analytical Modeling: Previous studies and state of the art

In general modeling of synthetic jets can be divided in two categories: analytical and numerical. While the specifics and subcategories of each will be discussed in later sections, the purpose of this section is to highlight some of the important work done in the field. In 1996 Rathnasingham and Breuer (Rathnasingham & Breuer, 1996) coupled a circular plate model with a control volume model and developed a system of five nonlinear first order differential equations to estimate the vibration characteristics of the diaphragm, properties of the fluid in the cavity and the jet exit velocity. They used this model to address the importance of flow features inside the cavity and the orifice. Their work also identified important non-dimensional parameters that have significant influence on the formation and evolution of the synthetic jet. In 2003 Gallas and Cattaffesta (Gallas, et al., 2003) modeled an SJA using a lumped parameter system. They modeled the components of a single SJA as components of an electric circuit. This allowed them the flexibility of studying the geometric parameter space associated with the cavity and orifice as well the electro-mechanical behavior of the piezo disc with relative ease. Due to the transformation from the mechanical/fluidic domain to the electrical domain, their model was unable to incorporate any unsteady effects which are important when considering array interaction. An improved lumped parameter was developed by Tang and Zhong (Tang & Zhong, 2006) which takes into account the unsteady nature of the flow and predicts the temporal variation of the synthetic jets, but only when the actuator was operating away from the Helmholtz frequency. Both these models were developed in order to predict the flow field inside the cavity and the orifice in response to the surface oscillation.

Several analytical models have been developed since the early 1970s e.g. Campbell and Schetz, (Campbell & Schetz, 1972) that look at the interaction of turbulent steady jets with environments that they are injected into. Kral et al. (Kral, et al., 1997) were the first to show that the time averaged behavior of synthetic jet flow field was very similar to that of turbulent steady jets. Using this fact Ugrina (Ugrina, 2007) developed a model that predicted how a synthetic jet behaves under the influence of a cross-flow. The jet was modeled as stream of turbulent flow entering and traveling through a body of uniform laminar flow. By using entrainment coefficients she was able predict how the jet would evolve in the presence of a cross-flow. The model was dependent upon entrainment and blockage values that needed to be determined experimentally or numerically. More recent attempts of modeling synthetic jet actuators analytically involve work done by Persoons (Persoons, 2012). Using a lumped parameter model with fluidic as well as electro-magnetic elements he predicted the fluidic response of the jet to varying electrical input.

1.4.2: SJA Numerical Modeling: Previous studies and state of the art

Analytical models present a distinct advantage in the fact that the computational requirements are minimal, however they are limited in their ability to predict the flow accurately over a broader range of operating conditions. This constraint usually presents itself in the form a dependency on some experimental/numerical information for the model to function accurately. Numerical models on the other hand are much more versatile and flexible. This is why the majority of literature on modeling synthetic jet actuators involves numerical methods. While the cost associated with time and computational resources is significantly higher, numerical simulations have been shown to accurately capture important flow features associated with SJAs. There exists a vast amount of research that has been performed on numerical simulation of SJA dating back to the 1990s. Kral et al. were the first to simulate actuators that have geometries relevant to this study (Kral, et al., 1997). They used an incompressible CFD solver (INS2D) to simulate synthetic jets. They were successfully able simulate important features that are associated with the rectangular orifice geometry, such as the vortex pair produced at the lip. They observed that while a laminar incompressible unsteady solution was adequate to capture the formation of the vortex pair, it failed to predict the breakdown and therefore the correct diffusion rate. By using a one equation Spalart–Allmaras turbulence model they were able to improve the prediction. The difference between the two models is illustrated by the velocity vectors shown in Figure 8. One of the important conclusions of their study was the fact that they were able to prove that the time averaged behavior of an unsteady SJA was very similar to that of a steady synthetic jet.

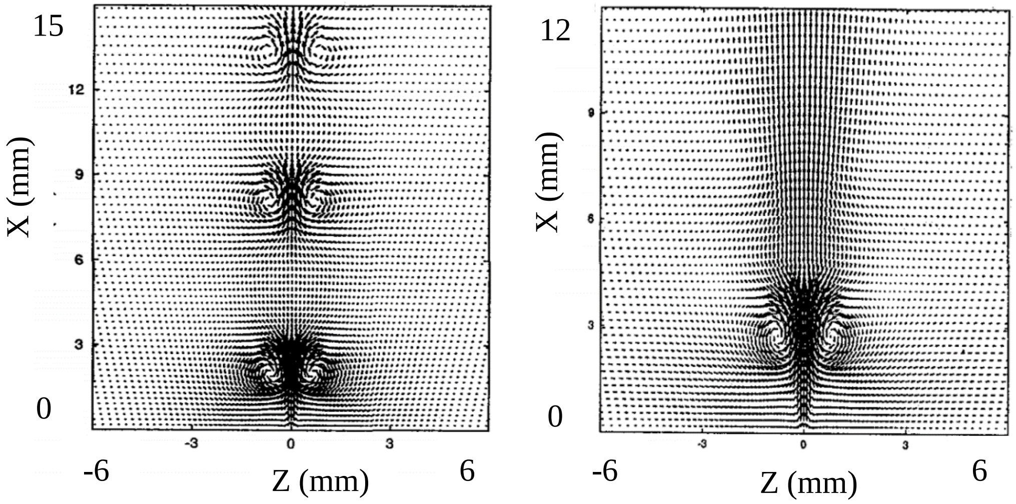

Figure 8 Velocity contours for an SJA (Left) Laminar flow model prediction (Right) Turbulent flow model prediction (Kral, et al., 1997)

While Kral was able to successfully capture the behavior of synthetic jet flow field outside the cavity, the first complete numerical study for flow inside and outside the cavity was performed by Rizzetta et al. (Rizzetta, et al., 1999). Their results predicted the existence of vortex fields inside as well as outside the cavity (complete SJA field). Several noteworthy numerical studies have been performed on complete SJA fields. They include work done by Utturkar et al. (Utturkar, et al., 2003) who demonstrated that the details of the SJA cavity design and the placement of the diaphragm do not play a significant role in synthetic jet flow characteristics such as vortex formation.

Mittal et al. (Mittal & Rampunggoon, 2001) were the first to study in detail the full synthetic jet interaction with an external cross-flow. They numerically simulated the interaction and demonstrated the formation of large recirculation bubbles for the case when the average jet velocity was at least three times greater than the cross-flow velocity. This result is significant because it explains how synthetic jet actuators can create instabilities in flows that can be manipulated to direct momentum from regions of high value (free stream cross-flow) to that of low values (boundary layer). In 2003 Orkwis and Filz (Orkwis & Filz, 2003) first simulated the internal and external flow on two high speed actuators interacting with a subsonic high speed (M = 0.3) cross-flow, using a compressible flow solver. They determined that the performance of the two individual actuators was influenced by the way they were situated and operated with respect to one another.

A majority of recent numerical research performed on SJA is application oriented however there are some studies that focus on the fundamental physics associated with synthetic jet flows. Goh and Lee (Goh & Lee, 2013) studied the influence of operating two actuators completely out of phase (one actuator is ingesting while other is expelling) in a channel flow. They determined that such operation resulted in higher turbulence levels associated with the mean flow in the channel. Tang and Huang (Tang & Huang, 2013) investigated how the flow predicted by numerical simulation is dependent upon modeling technique used. Using this information they were able to establish a relation between the physics of the flow and the solution technique that would allow for the fastest and most accurate solution. Li and Sahni (Li & Sahni, 2014) conducted a numerical investigation to study flow structures and interactions that were caused by a pitched synthetic jet placed in a laminar (Blasius) boundary layer with zero pressure gradient. Using 2D and 3D unsteady CFD they studied the dependence of several flow features on the pitch angle and other operational parameters. These features included the train of vortex pairs, sub-harmonics associated with flow, vortex pair switching, vortex splitting, and complex vortex interactions. They observed a strong relation between the rate of breakdown of vortex pairs and the pitch angle. Their study of the sub-harmonics concluded that there were non-present for pitch angles of less than 90°. They observed for a higher jet-to-cross-flow velocity ratio and lower operating frequency the generated vortex pairs would ‘switch partners’. With a higher velocity ratio, the jet exerts a stronger wall like (or local blockage) effect against the cross-flow. This causes a recirculation zone to form just downstream of the jet. The clockwise vortex of a newly formed pair is formed within this recirculation zone and travels with a slower velocity compared to the cross-flow. However, the counter-clockwise vortex experiences faster cross-flow, causing it to move with the cross-flow and accelerate over the clockwise vortex. Thus, the counter-clockwise vortex surpasses and separates from the clockwise vortex and pairs with the clockwise vortex from the previous jet cycle. They concluded that this separation and pairing of individual vortices also contributed to the observed sub-harmonic behavior (under specific conditions) because these phenomena occur at a frequency that is half of that of the jet actuation frequency. An illustration of this process is shown in Figure 9 which shows the vorticity contours from three consecutive cycles (named A, B and C) at different phase instances (0° being the start of the expulsion cycle). The vortices are labeled counter-clockwise (CCW) and clockwise (CW) accordingly.

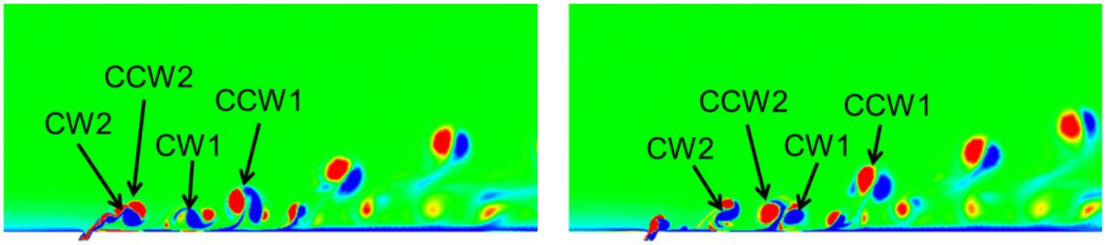

(a) Cycle A, Phase 192

(b) Cycle B, Phase 72

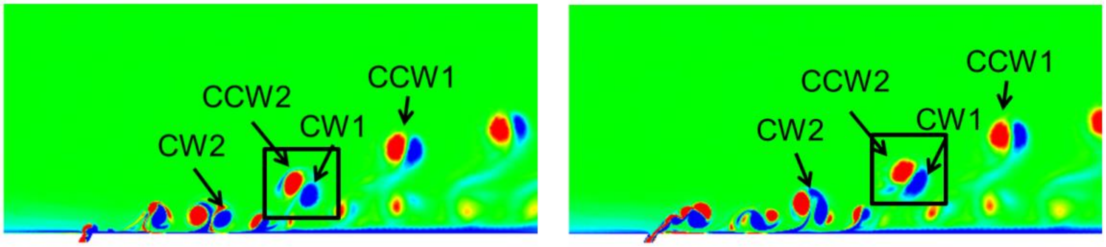

(c) Cycle C, Phase 48

(d) Cycle C, Phase 192

Figure 9 Vorticity contours illustrating vortex switching (Li & Sahni, 2014)

In addition to studying fundamental flow physics numerical simulations have been used to study applications of synthetic jets to full scale problems. These problems range from flow separation over full scale 3D aircraft wing to flow control over ground vehicles. Performing experiments on such problems is usually too costly. Jee et al. (Jee, et al., 2013) numerically investigated SJA for rapidly maneuvering airfoils that were regulated by a closed-loop control system. To support the active flow-control simulations that they performed, they developed a closed-loop system coupled with the vehicle dynamics and the computational fluid dynamics. By simulating forced and unforced high-frequency sinusoidal pitching, they showed that SJAs were able to provide bidirectional change in aerodynamic forces during rapid maneuvers. The time scales of these maneuvers were of the same order as the flow instability time scales. Hu et al. (Hu, et al., 2013) also used numerical simulations to control the internal flow through an S-inlet. They concluded that by tuning the actuation parameters a specific way, it was possible to have significant control over the pressure distribution at the exit. The potential of synthetic jets to be used for novel applications such as heat transfer has led to an interest in simulating and understanding their influence on canonical geometries. For instance, Silva and Ortega (Silva & Ortega, 2013) used 2D CFD to study the flow and heat transfer properties of an oscillatory jet. The goal of their study was to observe the dependency of cooling effectiveness of SJA impinged flow on the parameters of actuation. They used scaling analysis of the governing equations, identified non-dimensional groups and proposed a correlation between heat transfer properties and actuation parameters. They concluded that a fundamental frequency, in addition to the jet forcing frequency, exists in the flow and attributed it to the coalescing of consecutive vortex pairs. They demonstrated using time-averaged data that the merging of these vortices was responsible for a lower heat transfer. Naggapan et al. (Nagappan, et al., 2013) also computationally analyzed the heat transfer properties of SJA influenced flow; however they were after the opposite effect. They conducted a parametric search to investigate a novel approach to icing control that employed an array of thermally-activated SJAs embedded in a surface subjected to a super-cooled flow. They studied the effects of actuation on a flow over wedge geometry. They demonstrated that using heated SJAs led to partial as well as complete reduction in the amount of ice accumulating on the wedge surface. They also studied the effects of upstream flow conditions and SJA parameters on the ice thickness profiles.

Finally applications such as mixing have also been the subject of extensive numerical research. Recent studies include work done by Wu and Ahmed (Wu & Ahmed, 2012), who numerically simulated the flow of air in a full scale aircraft cabin.

The studied the effect of actuation on the ventilation performance in the cabin. By applying periodic air supply and SJA control they demonstrated that the flow pattern became oscillatory and the fresh air swept a wider region reducing the mean age of air in the cabin and improving air quality. By performing actuation close to the air supply inlet, they vectored the ventilation jet, which demonstrated the potential to more actively control the fresh air direction.

1.5 Literature Review: Synthetic Jet Actuator Experimental analysis

1.5.1: Fundamental physics of SJA flow

Modeling synthetic jet actuators through numerical or reduced order methods is generally the preferred and least costly method of studying them. However as determined by Tang and Huang (Tang & Huang, 2013), modeling in general, must often be tailored to the problem. Some empirical knowledge is usually required e.g. displacement and/or velocity profile of the oscillating surface. A vast amount of research has thus been devoted to experimentally analyzing SJA. One of the most comprehensive studies performed on experimentally characterizing a single SJA was done by Smith and Glezer (Smith & Glezer, 1998). They used Schlieren visualization to detail the formation, advection and breakdown of the vortex pair ring which is one of the most important features of SJA flow. They concluded that the breakdown of the vortex pair in the streamwise direction (Figure 3) is influenced by the vortex ring that forms along the span of the orifice (Figure 4). In addition to this they determined that there were two important types of flow that composed the overall flow field. The *near field* which exists in the vicinity of the orifice was dominated by unsteady flow. For their geometry this region was in the range of $x / b < 20$. Within this region the vortex pair fully develops ($x / b < 4$) and separates from the cavity flow. Further away from the orifice the vortex pair continues downstream and its downstream motion induces an unsteady component in the velocity along the jet centerline ($4 < x / b < 10$). The second type of flow constitutes the *far field*, $x / b > 20$. Here the vortices are no longer coherent structures, as they undergo transition to turbulence, and the induced unsteady component has diminished to a small value. At these heights they observed unsteady component was less than 5% that of the mean value.

The other important aspect of their study was understanding development of the jet in three-dimensions. In section 1.2.2 the formation and development of a synthetic jet were discussed under a high aspect ratio assumption. Smith and Glezer showed that jet cross-section maintained an aspect ratio of approximately, 10 as far out as $x = 20\,b$. Their velocity contour results which are shown in Figure 10 show the expansion of the jet in *yz*-plane. The jet expands in the *y*-direction as it contracts in the *z*-direction. In addition to diffusion and advection the vorticity created at the spanwise ends of the orifice is responsible for this effect. From Figure 10 we observe that even at a height of $x = 20\,b$ above the orifice the distance from the spanwise end of plume to the center is around 10 times the width of the jet in the *y* direction. Since vorticity induced effects scale inversely to the distance from the source, for a jet of this aspect ratio, it can be assumed that any vorticity induced effects at the center of the orifice are small. This observation is crucial to the modeling aspect of this study as will be discussed in subsequent sections. In contrast to a SJA a steady turbulent produces vorticity in way that leads to formation of horse shoe structure as opposed to a dog bone structure observed in Figure 10. For a steady turbulent jet this structure is responsible for longitudinal streamwise mixing.

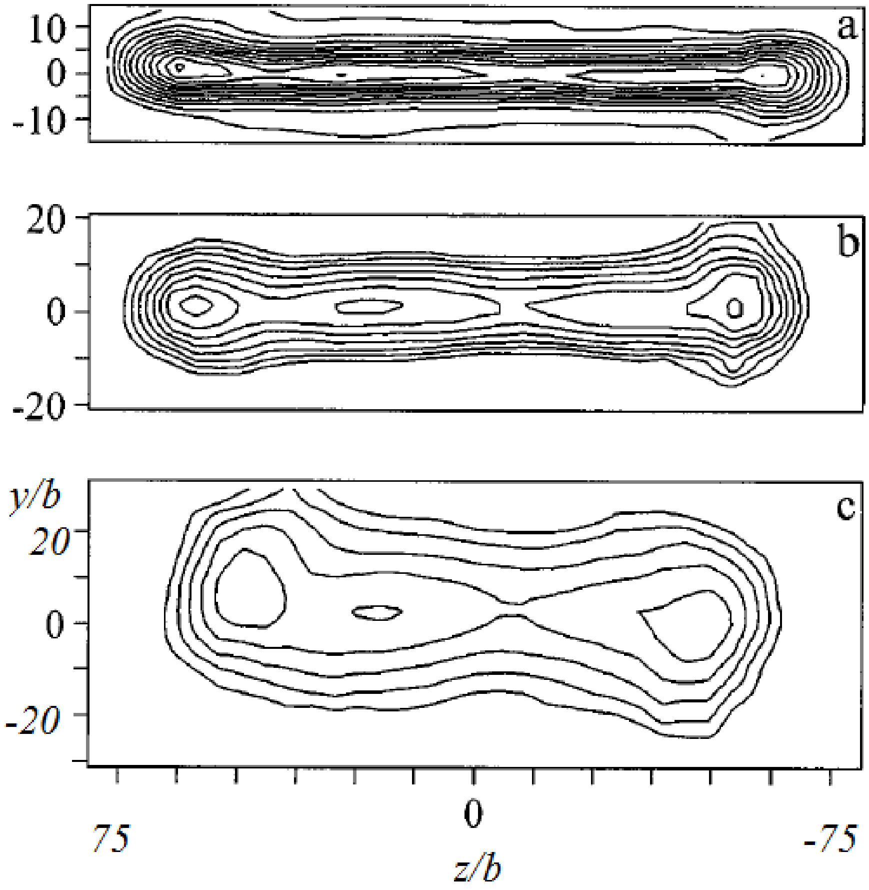

Figure 10 Contour maps of velocity in the *yz*-plane at (a) *x/b* = 19.7 (b) *x/b* = 39.4 (c) *x/b* = 78.7 first contour at 1*m/s*, increments of 0.5 *m/s* (Smith & Glezer, 1998)

While the external flow field produced by a synthetic jet has been well characterized by several studies, the internal cavity flow has not received much experimental attention. The reason for that is the difficulty associated with obtaining measurements inside the cavity. Some work has been done in regards to pressure and velocity measurements. In 2004 Yao et al. (Yao, et al., 2004) performed Particle Image Velocimetry (PIV) and Laser Doppler Velocimetry (LDV) to study the flow produced inside and outside the cavity of single high aspect ratio geometry actuator. They correlated the flow characteristics to actuators operating parameters such as diaphragm displacement, internal cavity pressure and temperature. Also in 2005 Smith and Glezer characterized the pressure fluctuation as a function of input voltage by drilling small pressure taps (Smith & Glezer, 2005) into the cavity. By measuring the velocity at the orifice using a hotwire anemometer they determined that at resonance the pressure and velocity function were 90° out of phase.

Since most applications involve the use of more than one synthetic jet, it is imperative to understand the array dynamics of jet-jet interaction. While most research involving synthetic jet arrays is application focused there is some literature which deals with how two jets interact with one another. Smith and Glezer (Smith & Glezer, 1997) studied the interaction of two synthetic jets with a steady turbulent jet. They showed that by adjusting the relative strength of the synthetic jets they were able to vector the trajectory of the steady jet. Their conclusions were important because of the fact that the steady jet length scaling was two to three orders of magnitude larger than that of the synthetic jet dimensions. In 2005 they (Smith & Glezer, 2005) demonstrated that this vectoring effect can be reproduced by altering the phase of operation, this time for the merged trajectory of two synthetic jets. The significance of these studies is that they established the relative phase of operation as an important parameter governing SJA array interaction.

1.5.2: SJA cross-flow interactions

The interaction of a single synthetic jet with cross-flow has been the subject of many studies that focus on a specific application e.g. work done by Amitay et al. (Amitay, et al., 2001), (Amitay, et al., 1998) who studied experimentally the effect of actuation for flow control over airfoils and other aerodynamic bodies. However in order to design systems which extract maximum benefits of actuation it is necessary to understand the mechanisms which are responsible for inducing desired effects. This section is therefore dedicated to the review of some of the important studies that deal with experimentally analyzing the fundamental physics of jet-cross-flow interactions.

Smith, Glezer (Smith & Glezer, 1997) and Amitay et al. (Amitay, et al., 1998) were the first to analyze the effect synthetic jet actuators in cross-flows. They concluded that actuation performed at a frequency that was one or two orders of magnitude larger than any other frequency associated with the flow (e.g. natural shedding) would result in a local displacement of streamlines in cross-flow. Their work helped establish that the non-dimensional frequency F^* is the parameter that determines whether the effect of actuation is to modify local shape ($F^* \sim 10$), or enforce local instabilities ($F^* \sim 1$). In 2002 Smith (Smith, 2002) investigated the interaction of synthetic jets with a turbulent boundary layer over a flat plate. He studied the effect of orientation of the orifice on the interaction with cross-flow. He observed that when the orifice was normal to the mean flow direction, the boundary layer was characterized by a wake like region in the downstream vicinity of the jet due to a blockage effect. However when the orifice was aligned with the mean flow direction, the flow structure indicated the presence of longitudinal vortices embedded in the boundary layer. By aligning the orifice in the direction of the flow Smith demonstrated a completely different flow behavior than what is observed for an orifice that is normal to the flow. Actuation in this form had effects similar to passive vortex generators (such as riblets). In 2003, Schaeffller (Schaeffler, 2003) studied the effect of orifice geometry on the ability to penetrate the boundary layer of cross-flow. He observed through analysis of the mean flow pattern that for the case of a circular synthetic jet interacting with a cross-flow that the interaction is most significant at the highest ratio of jet velocity to cross-flow velocity. He also observed that for the elliptical jet, even at a higher velocity ratio, penetration was not as strong as it was for the circular orifice. Milanovic and Zaman (Milanovic & Zaman, 2005) also performed a detailed analysis of the effect of the orifice geometry on the interaction.

1.5.3: SJA application based experiments and state of the art

Most recent experimental studies performed on SJA analyze the effect of actuation for flow control over an aerodynamic body. This includes work done by Rathay et al. (Rathay, et al., 2014) who applied high frequency actuation at specific location on a scaled model of a tail rudder. They observed that by situating the array of actuators at a specific location they could improve the side force on the model by up to 18%. They concluded that actuators located at mid-span provide the greatest contribution at moderate rudder deflections, and actuators located at the root provided the greatest contribution at high rudder deflections. Jabbal et al. (Jabbal, et al., 2013) used an inclined configuration actuator array on an aircraft wing to improve lift production. By experimentally studying the parameter space associated with an array of 30 actuators they determined an optimum arrangement for installation of the actuators to achieve a specified lift configuration. Kourta and Leclerc (Courta & Leclerc, 2013) applied synthetic jet actuation to 0.7 scale Ahmed Body (bluff body vehicle model). They examined the topology of the longitudinal vortices produced in the wake. By performing actuation under very specific conditions they demonstrated drag reductions of up to 8.5%. They concluded that the SJA control allows the dynamic reattachment in the separated region and balanced the torus vortex structure created at the base of the model.

In addition to modifying aero properties of flows over airfoils (or other aerodynamic bodies) SJA have been used for mixing applications. The mixing capability of synthetic jets allowed Jin et al. (Jin, et al., 2014) to perform more effective heat transfer for controlling the rate of the icing process over a flat plate. Montoya et al. (Montoya, et al., 2010) used SJA to control particle dispersion in a closed chamber. Their results demonstrated the application of SJA for controlling indoor air quality in confined spaces. By situating arrays of synthetic jets on either side of an aerosol inlet they were able to control the direction of flow through the inlet. They demonstrated the effectiveness of the synthetic jet-based flow control for aerosol dispersion and removal in their closed chamber. They also demonstrated the possibility of using SJA in smart buildings for improving indoor air quality while minimizing the energy burden on heating, ventilating, and air conditioning systems.

1.5.4: Summary of Literature Review

In summary all the studies quoted as part of Chapter 1 Section 5 provide valuable information about the mechanisms associated with jet formation and development. In addition to this observations of the *yz*-plane growth of the jet indicate a 2D flow close to the SJA orifice. This information was used to simplify the modeling aspect of the project. Since one of the objectives of this study is to understand the fundamental physics associated with array-cross-flow interactions, some of the methods used in the studied literature are also used to characterize the interaction.

1.6 Important Synthetic Jet and array parameters

1.6.1: Single actuator operating and geometric parameters

Amplitude (A)

Actuator operating amplitude is a direct function of the driving voltage, and directly influences the maximum output velocity. For a single actuator the velocity characterization as a function of voltage is shown to have an almost linear behavior, up to a certain point. For an array of actuators this parameter will be adjusted in a way that allows for similar Reynolds number (Re) for both actuators.

Frequency (f)

Actuator operating frequency is controlled via the drive signal. It influences the physics of the synthetic jet actuator in several ways. In the simplest case of a single actuator if f has a value close to the cavity acoustic resonance frequency it allows for maximum exit velocity for fixed amplitude A. In the sections to follow this phenomenon is referred to as jet mode resonance.

For the case of arrays the frequency can couple with other geometric parameters to determine the aggregate behavior of the array. A more thorough analysis of how the frequency affects actuator behavior would involve studying the modulation effects. Modulation allows for the effective actuation to be performed at frequencies much lower than the jet mode resonance. For the purposes of this study, the frequency of the drive signal is fixed well below resonance. The rationale behind this choice is explained in the experimental analysis section.

Orifice and Cavity Geometric Parameters (l, b, H_o, D_c and H_c)

The parameters associated with the orifice and the exit plane were explained in Figure 2. They are the orifice length (l) and the orifice width (b). In addition to these two dimensions, the orifice has a height (distance separating the exit plane of the orifice with a plane that connects to the cavity). This dimension is often referred to as orifice lip thickness and is denoted by H_{o}. For the purposes of this study all these dimensions are fixed. In addition to orifice dimensions the cavity dimensions and shape are critical in determining what the resonance frequency of the acoustic system is. It is therefore important to design the SJA so that the cavity dimensions lead to an acoustic resonance frequency that is close to the resonance frequency of the driving mechanism (Ugrina, 2007). While there are many efficient designs for SJA for the purpose of this study a cylindrical cavity with an asymmetric exit orifice was chosen. The cavity diameter D_c, and the cavity height H_c, are shown in Figure 11. Selection of values associated with these dimensions will be presented in the experimental results section. Note that the shape of the actuator is such that H_o varies along y. The maximum thickness for the boundary layer associated with flow inside the cavity would be where H_o is maximum and therefore for that reason it is measured at the edge of the cavity.

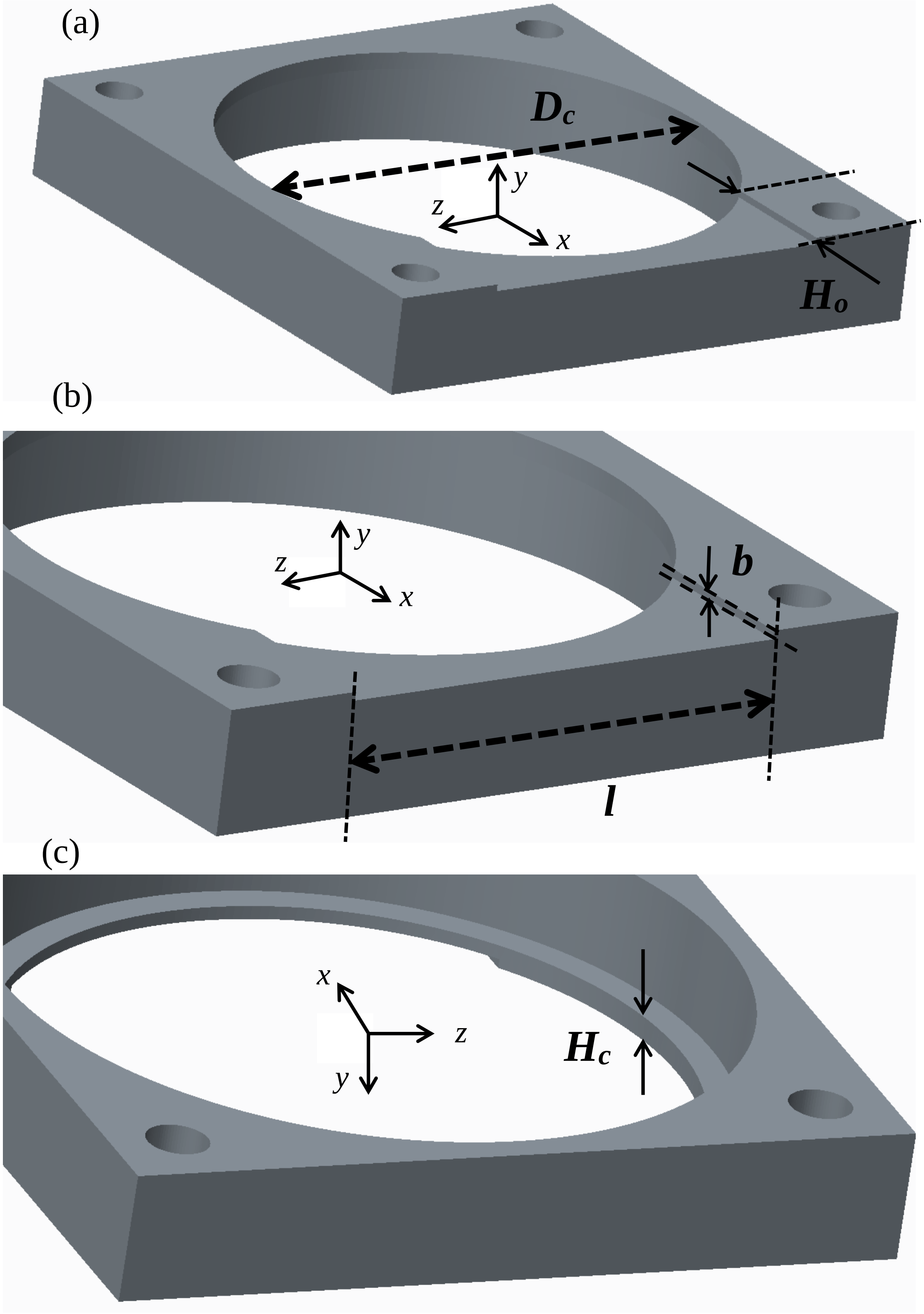

Figure 11 CAD drawings depicting actuator geometric parameters

1.6.2: Array geometric and operational parameters

Array Spacing (*s*)

Since this study focuses on understanding the fundamental physics of the interaction of synthetic jets with one another, the simplest array was chosen. This consisted of two actuators aligned with one another as shown in Figure 12. In an array of two actuators the interaction between the two jets will depend on how far they are from one another. Actuator spacing, s is therefore defined as the distance from the center line of the orifice of one actuator to the second.

Relative Phase Angle (φ)

Actuator interaction with other actuator and cross-flow in a 1-D array does not only depend on how far apart they are spaced, but also on the characteristics of any quantity being emitted by the actuators at any given instant in time. The phase difference φ is defined as the difference in degrees or radians of operating cycle between the 1st and the 2nd actuator (Figure 12). It can assume positive and negative values depending on which of the two actuators leads. For the purposes of this study the convention is defined such that φ is positive when the upstream actuator leads in phase and negative when it lags.

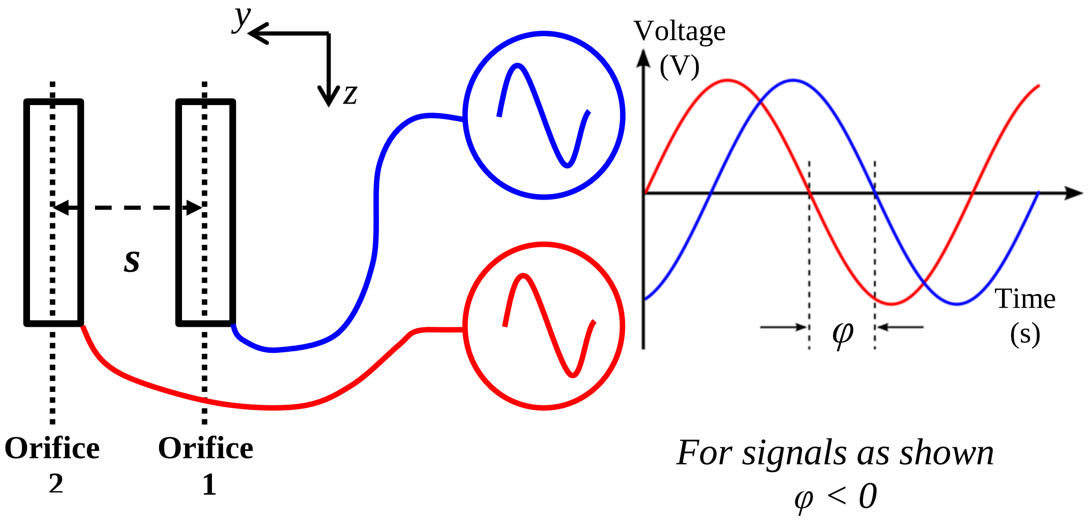

Figure 12 Schematic illustrating array parameters (for quiescent conditions) with excitation voltage to SJA1 (upstream actuator) shown lagging excitation voltage to SJA2

1.6.3: Synthetic Jet non-dimensional parameters

In order to study the behavior and compare it between two different sources of a synthetic jet it is common to characterize the jet using non-dimensional parameters. Such parameters are not only useful when comparing one jet to another, but also when comparing the interactions of two different synthetic jets under the influence of cross-flow. Important SJA non-dimensional parameters are discussed below.

Jet Reynolds Number (Re_J)

The Jet Reynolds Number has formulation similar to the classic Reynolds number. The length scale involved is usually the width of the orifice (*b*) (in the case of a rectangular orifice). Since the velocity of the exiting fluid varies over a cycle, based on the definition given by Utturkar (Utturkar, et al., 2003) we define the Jet Reynolds Number according to Equation 1. Here $\overline{U}_J$ is the velocity of the jet, calculated over the expulsion phase and averaged in time and space. Also, υ is the dynamic viscosity of the operating fluid (for the purposes of this study this will be air).

$$Re_J = (\bar{U}_J b)/v$$

Equation 1

The Jet Reynolds number is indicator of strength of the emerging vortex elements with respect to viscous forces the elements undergo. Beyond a certain threshold value of Re_J the vortices generated during ejection phase will have sufficient momentum to break away from the fluid body inside the cavity and propagate downstream, remaining unaffected by the suction phase of the cycle. The critical Re_J below which suction and ejection are identical in magnitude and opposite in direction, as determined by Wu and Breuer (Wu & Breuer, 2003) is 50. For this study the jet Reynolds number was held constant at 340.

Strouhal number (*Sr*)

The Strouhal number is the ratio of the unsteady inertial forces that exist due to oscillation inside the cavity to the inertial forces that are associated with the acceleration that cause convection of the fluid element away from the orifice. Wu and Breuer (Wu & Breuer, 2003) define it as a comparison of the excitation frequency to the amount of time it takes a fluid element to pass through the orifice. The mathematical expression for calculating the Strouhal number is given in Equation 2. Strouhal number is what determines how many cycles of oscillation a fluid element undergoes before it manages to advect away from the orifice. According to Ugrina (Ugrina, 2007) Strouhal numbers of approximately two or greater indicate the dominance of inertial effects associated with the local oscillations in the flow. Under these circumstances the actuator undergoes several suction-blowing cycles before the fluid manages to advect away from the orifice region. For Strouhal numbers of less than two an element of fluid passes through the orifice in fewer cycles. All the jets analyzed in this study are of Sr less than or equal to 1. For such jets the expulsion phase of fluid occurs at least once per cycle.

$$Sr = fH_o/\bar{U}_J$$

Equation 2

Momentum Coefficient and Velocity Ratio (C_μ and R)

The momentum coefficient is one of the most important parameters of analysis that this study relies on. One of the benefits of using SJA as opposed to other steady sources of flow control is their ability to add momentum without adding mass. Since the desired effect is the addition of momentum, it is imperative to define a standard by which to measure it. For a single synthetic jet operating in quiescent conditions this can be done through calculating the jet momentum flux, J. For the type of actuator geometry this quantity is given by Equation 3.

$$J = \int_0^b \bar{U}(y)(\rho\bar{U}(y))dz\, l$$

Equation 3

Here $\bar{U}(y)$ is the time averaged velocity expressed a function of location along the orifice width, and ρ is the density of the operating fluid. The momentum flux given in Equation 3 is the 3D momentum flux calculated upon the assumption the velocity of fluid coming out of the orifice varies only along the y-direction. For a high aspect ratio synthetic jet this is generally the case along the orifice span except for close to the orifice ends, therefore the momentum flux for such an actuator can also be studied as momentum-flux per unit span (2D quantity).

For a synthetic jet operating in cross-flow it is desirable to scale this quantity by the cross-flow momentum flux calculated over the area upon which actuator influence is desired. This scaled non-dimensional quantity is referred to as the momentum coefficient, C_μ and is calculated as given by Equation 4.

$$C_\mu = \frac{\rho \overline{U}_J{}^2 b}{\frac{1}{2}\rho U^2 c}$$

Equation 4

The numerator in above equation represents the momentum flux per unit span associated with the synthetic jet. The denominator represents the momentum flux per unit span associated with a uniform cross-flow having a velocity *U*, over a length scale of *c*. This formulation of momentum flux is the most common one observed in literature. The momentum coefficient is an extremely important parameter for characterizing SJA-cross-flow interaction. It is the key parameter that predicts when the influence of the jet will be strong enough to induce a desired change. A closely related parameter to the momentum coefficient is the velocity ratio (often referred to as the blowing ratio) *R*. Mathematically, it is represented as the ratio of jet-averaged velocity, $\overline{U}_J$ to cross-flow velocity, *U*. Physically; it represents the penetration ability of the SJA in a cross-flow.

Non-dimensional Frequency (*F**)

The non-dimensional frequency is a measure of how long it takes for a specific flow feature to advect a specific length, *c*, in relation to the frequency of actuation. It is another important parameter that governs the physics associated with problem. For $F*$ values of close to 1, the SJA is operating such that the frequency of operation is close to any natural frequency associated (e.g. vortex shedding) with the flow in the region of interest (which has characteristic length c). The effect of actuation at this value of non-dimensional frequency is that of enforcing the natural structures. This range of operation is beneficial for separation control applications (Seifert & Wygnanski, 1996). If the actuator is operated at much higher frequencies ($F*$ close to 10) the jet frequency is now decoupled from that of any natural instability. Operating the jet under these conditions results in shape modification of cross-flow streamlines in the vicinity of the orifice. The mathematical expression for non-dimensional frequency is given by Equation 5.

$$F^* = \frac{fc}{U}$$

Equation 5

1.7 Objectives and organization of the dissertation

1.7.1: Goal and objectives

The motivation for this study stems from the application potential of synthetic jet actuators in systems that are designed to operate over a variety of conditions. In order to accomplish this it is necessary to have control over the flow field created by the SJA. By understanding this flow field and its dependence on the parameters discussed in previous sections, it would be possible to implement a single SJA or an array of SJA in a manner such that they have control authority over a range of conditions. While flow control using a single SJA has been studied extensively, the applications of it are very limited. The reason for this is the limited control authority associated with a single SJA. The control authority is loosely defined as a measure of the SJAs ability to induce a desired change in the flow (Ugrina, 2007). These measures can include qualitative quantities such as field streamline displacement, and, quantitative parameters such as the momentum coefficient. For the purposes of this study we will analyze both kinds of measures, with a specific focus on the momentum coefficient. Looking at the definition of the momentum coefficient as given by Equation 4, it is easy to observe that if two actuators operate in the region characterized by length, *c*, the numerator term would double. In other words we would observe twice the momentum of a single actuator over the region. And for *n* actuators installed in the region the momentum value would be *n* times that of a single SJA. It will be shown in subsequent sections that this is not entirely the case. To understand why this occurs, it is important to look at the momentum coefficient of an array of actuators and its dependency on the individual actuators. Since the total momentum imparted by an array is simply the sum of momentum associated with individual actuators the array momentum coefficient is given as by Equation 6.

$$C_\mu^{Array} = \sum_{i=1}^{n} C_\mu^i = \frac{\rho {\overline{U}_{J,1}}^2 b_1}{\frac{1}{2}\rho U^2 c} + \frac{\rho {\overline{U}_{J,2}}^2 b_2}{\frac{1}{2}\rho U^2 c} + \cdots + \frac{\rho {\overline{U}_{J,n}}^2 b_n}{\frac{1}{2}\rho U^2 c}$$

Equation 6

From this formulation we observe that if the average jet velocity $\overline{U}_J$, is the same for all actuators, and they all have similar geometry (*b* is same for all actuators), then $C_\mu^{Array} = n * C_\mu$, however this is generally not the case. While *b* is a geometric parameter and easy to fix, $\overline{U}_J$ is a function of not only what happens inside the cavity but also what occurs outside of it. The impedance experienced by the flow exiting the cavity is a significant factor in determining the magnitude and direction of the jet flow. It is therefore almost always the case that $\overline{U}_J$ will be different for each member of the array. This concept will be discussed in detail in following sections. The goal of this study can now be summarized.

Goal: *The goal of this study is to identify the parameters that have significant influence over the control authority of an SJA array. Once identified, the effect of these parameters on array operation is studied.*

This goal is achieved by breaking down the overall task into objectives, which are summarized as follows:

1) Advancement of the understanding of array behavior that is associated with interacting SJAs. This is accomplished in two sub-stages.
    a. Stage 1: Develop numerical, reduced order and analytic models to predict array behavior of interacting SJAs in cross-flows. This objective allows us to study the entire parameter space without having to perform experiments.
    b. Stage 2: Obtain experimental results useful for validation of models and for studying sensitivity to SJA operational parameters.
2) Studying the dependency of control authority of SJAs arrays: This includes a characterization of the sensitivity of momentum produced to phase, spacing and velocity ratio through experiments as well as modeling. The choice of these parameters will also be explained.
3) Demonstration of the use of SJA array for dynamic virtual shaping

1.7.2: Organization of the dissertation

Chapter 1

An introduction to synthetic jet actuators as applied to flow control is provided. An explanation of the mechanisms which produce the synthetic jet is detailed. The physics behind the evolution of the jet and features such as the vortex pairs is explained. The motivation behind the use of synthetic jets is explained from an application perspective. A literature review of the past and recent work is provided to ensure that this study has a contribution to the field with minimal overlap. Modeling techniques involving numerical and analytical solutions were briefly discussed with a specific focus on aspects pertinent to this study. Experimental studies from literature were discussed that detailed the physics of jet cross-flow interaction. Important synthetic jet and array operational parameters were identified based upon literature studies. Non-dimensional parameters relevant to characterizing the jet and its control authority were discussed. Lastly the contributions of this study to field were highlighted.

Chapter 2

The behavior of an array of two interacting synthetic jet actuators in the presence of a cross-flow was simulated. Three modeling methods were used. The first method involved a numerical solution of the 2D unsteady Navier-Stokes equations through a commercial flow solver. Two complete actuators (cavity and orifice nozzle) were simulated. The second method involved a numerical solution to the stream and vorticity formulation of the Navier-Stokes equations. Instead of modeling the complete actuator, the effect of actuation was modeled as a sinusoidal perturbation applied at the bottom of a nozzle. A third method involving a linearized solution to the stream-vorticity equations was utilized. The actuators were modeled as perturbation boundary conditions. The effect of the actuators was spatially and temporally decaying perturbation flow superimposed on to a cross-flow. The models were used to study the physics of the interaction of an array of two synthetic jets with a cross-flow quantitatively and qualitatively.

Chapter 3

Based on a NASA design high aspect ratio finite span SJA were designed to validate the modeling techniques. The actuators were designed to have a 2D flow field in a region of at least 20 mm above the orifice and satisfy velocity ratio and geometric requirements of the modeling methods. CFD was used to calculate the appropriate cavity depth and aspect ratio to meet these requirements. The final design was used to build two actuators that were than characterized for frequency, voltage and velocity characteristics using CTA measurements.

Chapter 4

Quiescent and cross-flow synthetic jet actuator flow fields were characterized to validate the models studied in Chapter 2. PIV measurements were first validated against hotwire results, then used to verify the 2D nature of the synthetic jet. PIV was then used to validate the three models. In addition to validation the PIV results were also used to study the effects parameters on the flow field. Sensitivity to each of the selected parameters were analyzed. The ability of SJA arrays to dynamically virtually shape streamlines over a flat plate was demonstrated.

Chapter 5

The major contributions to the field are summarized and modeling validation results are summarized. Conclusions based on modeling predictions for SJA flow field features are discussed. The applicability of the experimental data for validation purposes is discussed. Limits in which the validation is valid are presented. Finally a potential path in which the project can be extended is outlined.

Chapter 2: Modeling Synthetic Jet Arrays interacting with cross-flow

2.1 Introduction to modeling

2.1.1: Modeling Approaches

Synthetic jet flows have important features associated with them. The prediction of these features is critical in accurately capturing the entire flow field. It is therefore desired that any model being considered should to capture these flow features. At minimum that model should be capable of capturing the time averaged effect of the jet on the cross-flow to be considered viable. Three specific classes of models are now defined: numerical modeling, reduced order methods, analytical methods. Each of these classes represent a different degree of trade-off between the accuracy and time in which the solution is obtained.

Numerical Methods

Under most circumstances, numerical methods are the most accurate category of methods. Starting with the full unsteady Navier-Stokes equations in differential form, a numerical approximation is made to each of the terms. The accuracy of the approximation depends on the solution scheme used to approximate each derivative. Once the derivatives are obtained the solution is usually marched in time (for unsteady flows), thus allowing to obtain a time history of the flow starting from initial conditions. For modeling a complete SJA in cross-flow it is necessary to model the cavity, orifice and the interaction domain. Several studies were discussed in section 1.4.2 that used full 3D unsteady modeling to predict SJA. This particular method requires the least amount of empirical data. The unsteady Navier-Stokes equations are generally solved over three fluid domains. The first domain consists of the flow inside the cavity. The actuation itself is usually represented as a velocity boundary condition applied to one of the walls of cavity. The second domain consists of the orifice nozzle; this connects the cavity to the third domain, which is the jet cross-flow interaction domain. The size and shape of the third domain depend upon the application or type of study. A representation of this setup is shown in Figure 13.

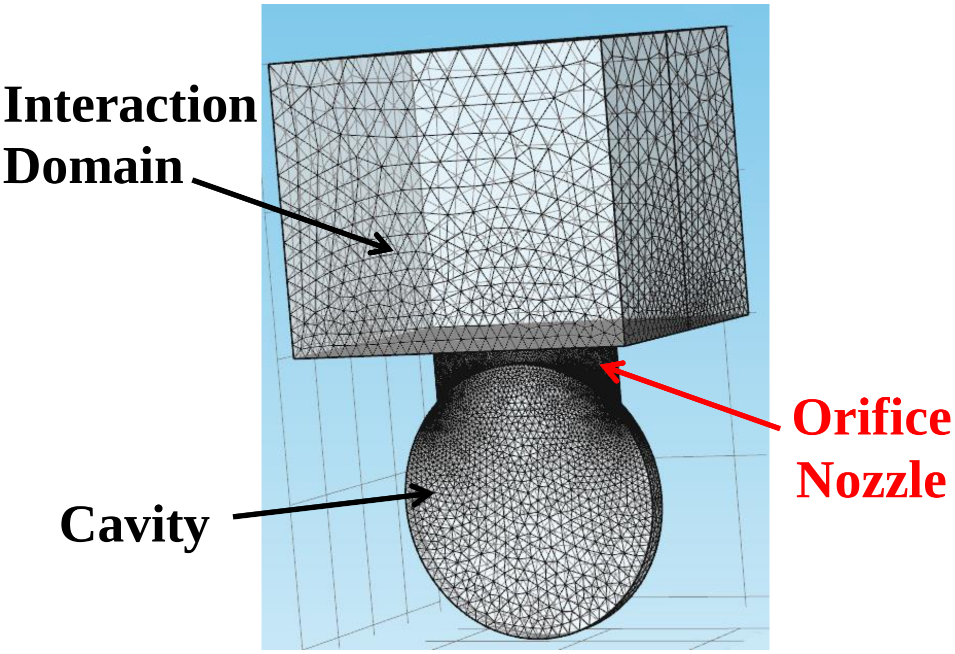

Figure 13 SJA numerical modeling domains

Within the class of numerical methods, 3D unsteady represents the most accurate subset. Unfortunately they are also the most expensive, requiring large amounts of computational resources. A typical solution for a jet interacting with cross-flow over a simple geometry (e.g. flat plate) requires multi-core processing to obtain a converged time averaged solution. Such a result often takes several days to obtain, and has limited statistical convergence. The meshing requirements for 3D methods are very memory intensive. In order to resolve features such as vortices a very fine mesh is required in and around the nozzle. Also a sufficiently large control volume must be considered in order to fully observe the interaction. This results in a high density, large mesh. This problem can be alleviated to a certain extent by using features such as symmetry, however even the simplified 3D unsteady simulation is hard to solve on a commercial desktop computers. A significant reduction in processing and memory requirements can be achieved by reducing the problem to a 2D problem. For the case of finite span high aspect ratio rectangular orifice actuators previous studies (referenced in section 1.4 and 1.5) demonstrate a 2D flow towards the center of the span of the orifice. Using this approximation, the memory and processing power demands can be bought to levels which are manageable by most modern commercial desktop PCs. The 2D flow approximation for SJA is only valid up to specific height above the orifice. 2D simulations are therefore constrained with respect to the size of interaction domain.

In addition to predicting the formation of flow features, numerical simulations are capable of accurately predicting the evolution and decay of these features. By adding components such as turbulence modeling they can accurately predict phenomenon such as vortex breakdown. Numerical methods are currently the most used class of methods for predicting jet flow.

Reduced Order Methods

Reduced order methods (ROM) which include certain perturbation techniques represent a class of methods which are usually dependent upon a reduced or limited form of the conservation laws. They usually involve an approximation to the full conservation laws or boundary conditions associated with the problem, solved by some form of numerical solution which is often faster than full Navier-Stokes 2D CFD alone. Such methods include work done by Schroeder et al. (Schroeder, et al., 1989) and Yamaleev et al. (Yamaleev, et al., 2005). The former simplified the stream-vorticity formulation of the Navier-Stokes equations through a small perturbation assumption. This resulted in two sets of PDE which modeled the disturbance effects as small and localized. The later used a quasi-1D formulation of the unsteady Euler equations to satisfy the continuity requirements. They then numerically solved the simplified equations to identify resonance characteristics of synthetic jets.

Since ROM and perturbation methods involve equations that are simplified versions of the full conservation equations they present a distinct advantage over pure numerical methods. Solutions times are shorter by orders of magnitude and computational resources are within the scope of dekstop PCs. In contrast to some zero-dimensional (Yamaleev, et al., 2005) methods perturbation and ROM techniques satisfy continuity requirements for mass, momentum and energy. Due to the simplification process, these techniques have disadvantages. In general they have reduced accuracy in comparison to numerical simulations. They also require more empirical information than numerical methods.

Analytical Modeling

The third and final class of modeling techniques covers methods that are purely analytical. Analytical models make use of some flow characteristics to simplify the PDEs associated with the full conservation laws to reduced versions. Such modifications can be based on geometry (e.g. assume an entrainment rate proportional to geometric size of the plume, or symmetry about a plane) or physics (e.g. potential flow). Analytical models have the distinct advantage of being several orders of magnitude faster than any numerical method. This quality makes them particularly suitable for parametric studies. The fidelity of an analytic model is generally dependent upon two factors. The first is the reduction process which used to obtain the governing equations for the model. The second factor is the amount and quality of the empirical information that is required for the model to operate. Generally analytical models require some form of empirical information to function. The accuracy of the experiments that are used to create this information plays a crucial part in governing the accuracy of the model. In addition to the minimum amount of information that is required for such a model to function, supplementing an analytical model with additional empirical information leads to improved accuracy. Ugrina (Ugrina, 2007) demonstrated this while modeling a single (low aspect ratio elliptic orifice) synthetic jet in a cross-flow. By using pre-measured entrainment values, she was able to predict the growth of the jet plume, direction of the jet trajectory and its blockage effect on the cross-flow. An example from one her study is presented in Figure 14 along with experimental results for comparison. The dependency of analytic models on empirical information is one of the disadvantages of using them. The efficiency and closed form exact solutions make these methods extremely attractive for purposes of control loop implementation, in spite of the sacrificed accuracy.

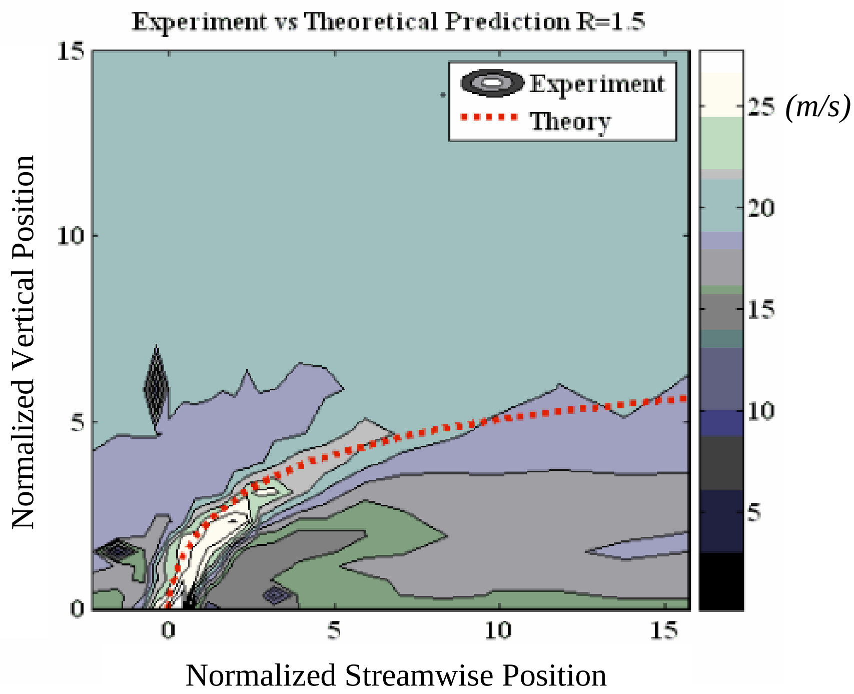

Figure 14 Comparison of jet trajectory analytical prediction with experimental data (Ugrina, 2007)

2.1.2: Modeling SJA: Selection of parameters

In order to meet the first objective specified in Section 1.7.1 it was necessary to identify an initial parameter space consisting of variables that had the most significant impact on the behavior of the jet. For a single actuator operating parameters such as frequency and amplitude govern the behavior for a specified cross-flow. By adding another actuator the number of degrees of freedom in the parameter space increases significantly. The first set of additional parameters is the operational amplitude and frequency of the second actuator. This adds two degrees of freedom to the parameter space. Also, for such an array the placement of the second actuator with respect to the first one is an important parameter. This adds three degrees of freedom (three Cartesian coordinates). In addition to this the orientation of the two actuators with respect to one another is also an important factor which could possibly add up two degrees of freedom (yaw angle with respect to cross-flow for each actuator). How the two actuators operate relative to one another is also a critical parameter, adding another degree of freedom. In order to limit the size of the parameter space and to focus on the jet-jet-cross-flow interaction this study is limited to two actuators in cross-flow.

By adding a second actuator the parameter space goes from 2 degrees of freedom to 8. It would be extremely costly to consider such as large parameter space and test for sensitivity using even the most efficient modeling techniques. The parameter space was therefore reduced to the most significant parameters based on previous studies. Three important parameters were selected for analysis.

Velocity Ratio (*R*)

Hassan et al. (Hassan, 2005) and DeMauro et al. (DeMauro, et al., 2013) performed experiments and concluded that while the behavior sensitivity to velocity ratio for various ranges of *R* is not high within each range, for the different ranges different kinds of behavior is observed. In general for *R* close to 1, the jet does not have sufficient energy to penetrate the boundary layer and usually results in mixing within the boundary layer. For *R* close to or greater than 2 the jet is capable of exiting the boundary layer and displace the streamlines associated with cross-flow. The optimal value of *R* is determined by the type of application the SJA is being considered for. For the purposes of this study we operate around the $R = 2$ range since deflection of the streamlines is one of the characteristics we wish to observe.

Phase Angle and Spacing (φ and s)

Smith and Glezer (Smith & Glezer, 2005) were the first to determine the importance of these two parameters. The reason why they play a critical role in determining the flow field is that the vorticity distribution at any given instant in time will change if the phase angle is changed. The primary conclusion of their study was that having two synthetic jets operating in close vicinity would lead to single observed plume. Instead of having two observable and distinct plumes flow from two closely spaced orifices leads to a single large plume. The volume flux associated with this plume is significantly larger than two times that of a single jet, indicating that the entrainment has more than doubled. Operating a closely spaced array out of phase leads to vectoring of the merged trajectory in the direction of the jet that leads in phase signal. Their results indicated that significant changes in the flow trajectory occurred for phase angle increments of 30°, providing an estimate of the sensitivity of the flow field to phase increment.

Phasing and spacing effects are closely tied to one another since phasing effects are caused by time dependent vorticity effects. Vorticity effects not only depend on the magnitude of the source but also distance of the source from any point of interest in the field. This coupled effect will be explored in greater detail as well in the modeling results section. In general Smith and Glezer observed that for any increase in volume flux or vectoring to be observed, the actuators need to be spaced close to one another (less than 5*b*). In addition to this Hasnain et al. (Hasnain, et al., 2013) observed that for spacing values of around *9b* two distinct plumes begin to form, indicating that the actuators are now operating independently of one another. While for some applications it is desirable to have the actuators spaced sufficiently far apart to maximize the region of influence, for the purposes of this study we wish to study the interaction of the actuators. In the Cartesian frame the second actuator can be placed at any location with respect to the first one, e.g. on an airfoil the second actuator can have its center located at different *x*, *y* and *z* values compared to the first one. In order to limit the spatial degrees of freedom the problem was first restricted to a plane (physically a flat plate) and then to a line (physically represented by 2D actuators only allowed to move in the cross-flow streamwise direction). This results in a single spacing parameter, referred to as *s*, representing the orifice wall to wall spacing. While it is common to measure the spacing of the two orifices from the center of each orifice, for the purposes of this study the distance was measured from the walls. These parameters along with a new coordinate system, with origin located between the two orifices, are shown in Figure 15.

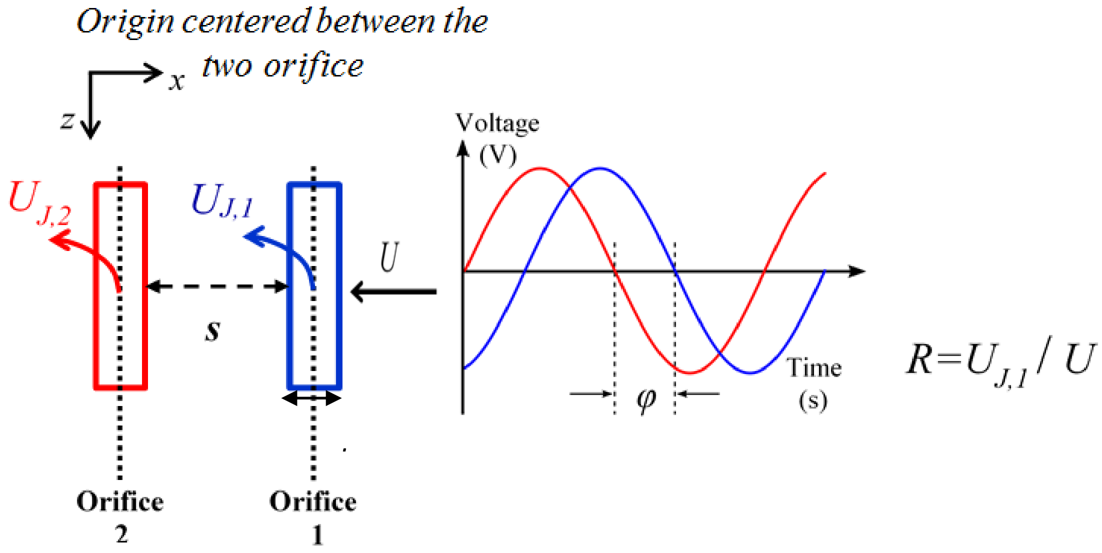

Figure 15 Parameter space for modeling with coordinate system

2.1.3: Parameter space for modeling matrix

Following the conclusions of previous studies the reduced parameter space was comprised of three degrees of freedom: the velocity ratio R, the relative phase of operation φ, and the orifice wall to wall spacing s. The strongest advantage of modeling over experiments is the ability to study a large parameter space while being able to observe sensitivities to individual parameters. With the reduced parameter space it is possible to analyze effects of individual parameters over a larger range. The coupling between parameters can also be analyzed. In order to accomplish this a test matrix was created as shown in Table 2. The purpose of this test matrix was to establish a coarse map of how the flow field behaves in response to extremes of these parameters. The increment values of each of these parameters is selected based on studies referenced in Section 1.5.

Parameter	Range	Increment
Phase (φ)	$-180° \leq \varphi < 180°$	30°
Spacing (s)	$2.5b \leq s \leq 4.5b$	b
Velocity Ratio (R)	$0.95 \leq R \leq 2.4$	1.45

Table 2 Parameter space matrix for modeling

These increments result in a total of 78 test cases. The phase increments represent values over which significant changes in flow direction and flux rates were observed. The spacing represents three regimes. The first in which the jet-jet-interaction is very strong and dominates the flow field, the second value is close to where the interaction begins to weaken, and the third and final represents the limit at which these jets have been observed to interact. Finally for the velocity ratio, the two regimes represent the jet being able to penetrate sufficiently far out of the boundary layer or not.

2.2 Details of modeling techniques

For the purposes of this study of each of the modeling techniques described in section 2.1.1 was utilized to simulate the interaction of two jets and a cross-flow. The pros and cons of each technique are presented in subsequent sections, along with details on the models.

2.2.1: CFD Solution

Methodology

For the initial stages of this study, computational fluid dynamics (or CFD) was selected as the method to simulate the flow. The reason for this choice lay in the fact that very little empirical information was available at this stage. A commercial solver package, COMSOL, was used to solve the unsteady incompressible 2D Navier Stokes equations along with a slightly modified version of the two equation (k-ω) Menter (Menter, 1994) shear stress transport (SST) turbulence model. This model was primarily chosen due to is tested and proven ability to deal with small and large scale turbulent flows, the kind of which are expected in the region of jet-jet-cross-flow interaction. The SST k-ω model does not utilize wall functions. The wall region is an important part of the interaction domain which is why the physics here needed to be completely resolved with as little approximation as possible. The discretization performed is per a finite volume method developed by Ravachol (Ravachol, 1997). Further details on the solution methodology can be found in studies published by Vazquez et al. (Vazquez, et al., 2004).

A 32 core desktop machine was utilized to perform all the numerical simulations. The machine had an available 32 GB of memory. With just over 90,000 elements, each simulation occupied 14 GB of memory at a time. While the software was capable of solving 3D models, for the case of 2 actuators and cross-flow, the memory requirements of the simulation based on a converged mesh exceeded the amount available. All such simulations were therefore limited to 2D.

Flow Domains, Boundary & Initial Conditions and Meshing

The flow domains that comprised the CFD model were a 2D version of those shown in Figure 13. The complete actuator was modeled as opposed to a reduced boundary condition. This was done to reduce the amount of empirical data needed. The domains and their dimensions are shown in Figure 16. The system consists of cavity, an orifice nozzle and control surface where the interaction occurs. The dimensions of the cavity and orifice were chosen such that they matched those of the actuators that were to be used for validation (at mid-span location). Since the problem was reduced to 2D certain features associated with the geometry of the actuator were lost e.g. cavity shape. The same domain was used to test all cases to ensure uniform mesh for all conditions. The dimensions of the interaction domain were chosen based on preliminary experimental data. The goal was to observe the nozzle near field and far field interaction. Preliminary experiments indicated that for the velocity ratios being tested the plume was fully developed within 20 mm (*40b*) of the nozzle. The maximum height of the interaction domain was chosen to be twice this value.

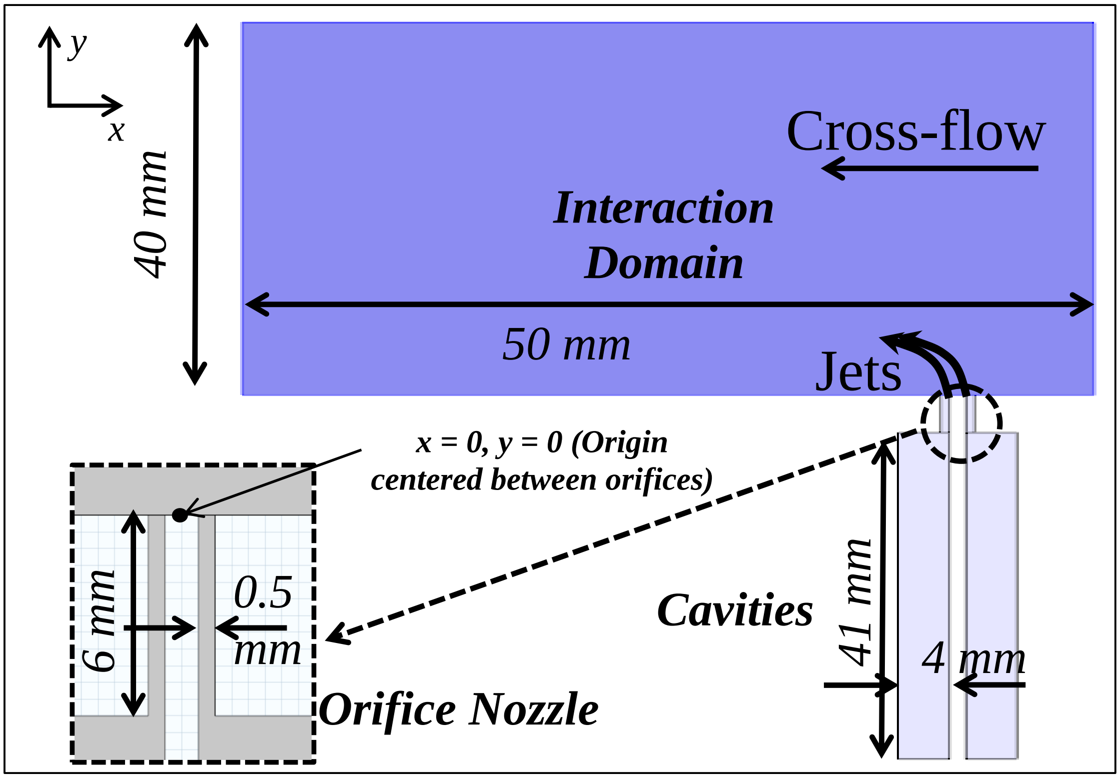

Figure 16 Simulated domain dimensions and coordinate system (illustration only not to scale)

For the domain shown in Figure 16 boundary conditions were specified along the edges of each sub-domain. The oscillating surface was modeled as spatially uniform sinusoid of frequency and amplitude matching that of the actual brass-piezo composite that was used for experimental verification. The boundary condition was applied to the side walls of the cavity. The magnitude of the sine wave was adjusted to control the velocity output from the SJA. The right edge of the interaction domain was specified as uniform velocity source and the left edge was specified as an outlet. The left edge was chosen sufficiently far (50 mm or *100b*) from the region of interaction in order to avoid convergence issues associated with reversed flow along this edge. The top edge of the interaction domain was specified to be an open boundary with zero initial pressure gradients. All other edges for the system were specified to be no slip walls. The unsteady simulation was started with both actuators off and cross-flow on. Initial conditions in the interaction domain were set to uniform laminar cross-flow to meet this objective. A zero flow velocity initial condition was specified everywhere else in the domain.

A uniform mesh was used to test all cases (even for the baseline case of zero cross-flow and single actuator). The mesh was generated using COMSOL. While the option to create a structured mesh was available, the unstructured meshing capability of COMSOL was used in order to reduce memory requirements. Although the mesh was unstructured, the software allowed control over the density of points for any specified region. The control parameters include the dimension of the longest edge of the smallest & largest element, the element growth rate, corner/sharp-edge density control and control over the number of vertical points in boundary layer. The mesh consisted of triangular elements.

Starting with the interaction domain a minimum element size of 0.02 mm was specified. This was done to ensure sufficient resolution along the exit edge of the orifice, and resulted in 25 points along the orifice. The growth rate in this region was then adjusted until time averaged solution based mesh convergence was achieved. The minimum element size inside the orifice was also set to 0.02 mm with a growth rate selected based upon mesh convergence. The minimum element size inside the cavity was also set to 0.02 mm to adequately resolve flow in region where the cavity connected to the orifice nozzle. Growth rate inside the cavity was also selected based on mesh convergence. A total of 14 heights were specified inside the boundary layer formed along the walls for all the domains, resulting in a dimensionless wall distance, y^+, of less than 5. A boundary layer stretch factor of 1.02 was selected, based upon mesh convergence of the flow field. Corner refinement was performed iteratively till the solution achieved mesh convergence. The criteria for such convergence will be discussed in the next section. A schematic illustrating the mesh and applied boundary conditions is presented in Figure 17.

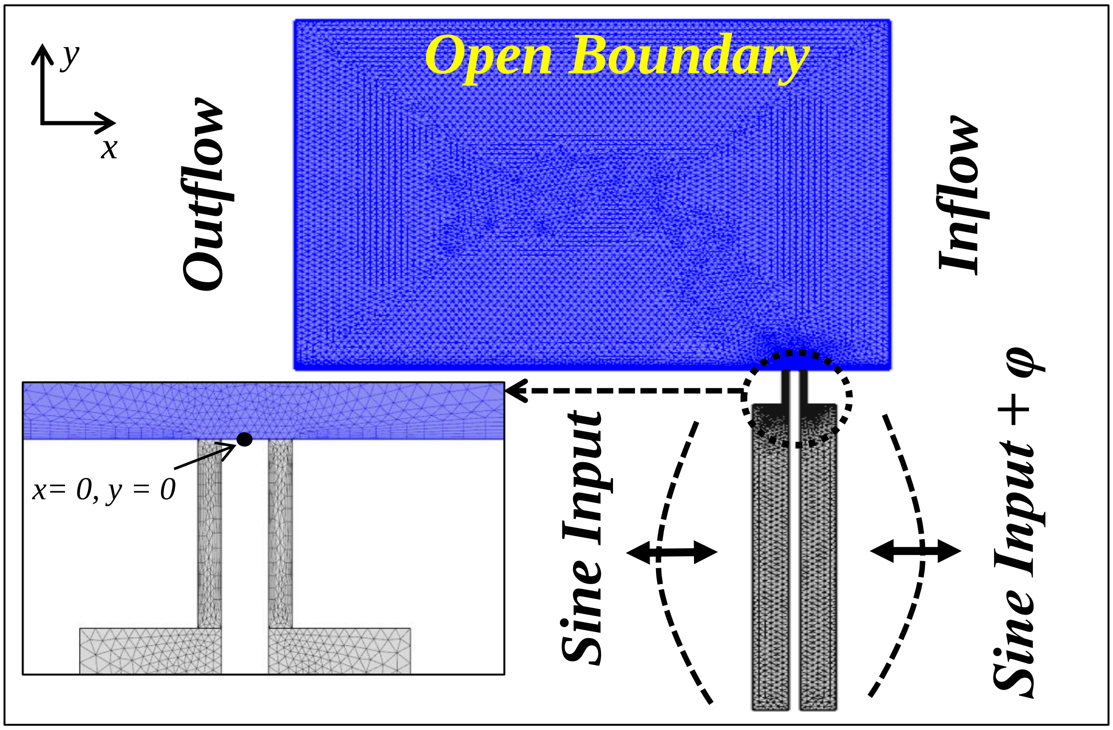

Figure 17 Mesh schematic with boundary conditions

An identical domain and mesh were selected for performing baseline tests (e.g. single actuator and quiescent). Such tests were performed initially to validate whether the model would accurately capture time dependent flow features. Once the veracity of the baseline cases were established a parametric sweep based on Table 2 was performed.

Temporal and mesh convergence analysis

Due to the high frequency oscillatory nature of synthetic jets unsteady simulations had to be performed in order to capture the time dependent effect of phasing the jets. The time step for the marching process was selected by the solver itself. Time marching in COMSOL is performed based on an adaptive step size as opposed to a fix step size. The solver has the ability to increase time step size or decrease it based on the observed temporal gradients at any instance. The maximum step size is in general limited by the time interval over which a solution output is requested from the solver. For all the simulations an actuation frequency of f = 1120 Hz was chosen based on the operational frequency of the actuators that were to be used for validation. Based on this frequency the time period of actuation is, $T = 8.9 * 10^{-4}\ s$. Since one of the objectives was to capture the time evolution of the flow features associated with interaction, a solution output was requested from the solver at an interval of 1/15 T. The purpose of doing this was to observe with adequate resolution how the flow field developed in time.

In addition to understanding the temporal evolution of the flow field, the purpose of modeling was to allow for an understanding of the behavior dependency on parameters. In order to do this the time averaged effect of the interaction had to be evaluated. For that purpose the simulation had to be run for a time that allows the average velocity results to be statistically converged. In order to establish the necessary number of cycles one of the test cases was processed and the time evolution of the average velocity at a point close to the orifice was observed. This point was chosen such that it was in the interaction domain, centered at 5*b* height between the two orifices. The time evolution of the average velocity is shown in Figure 18.

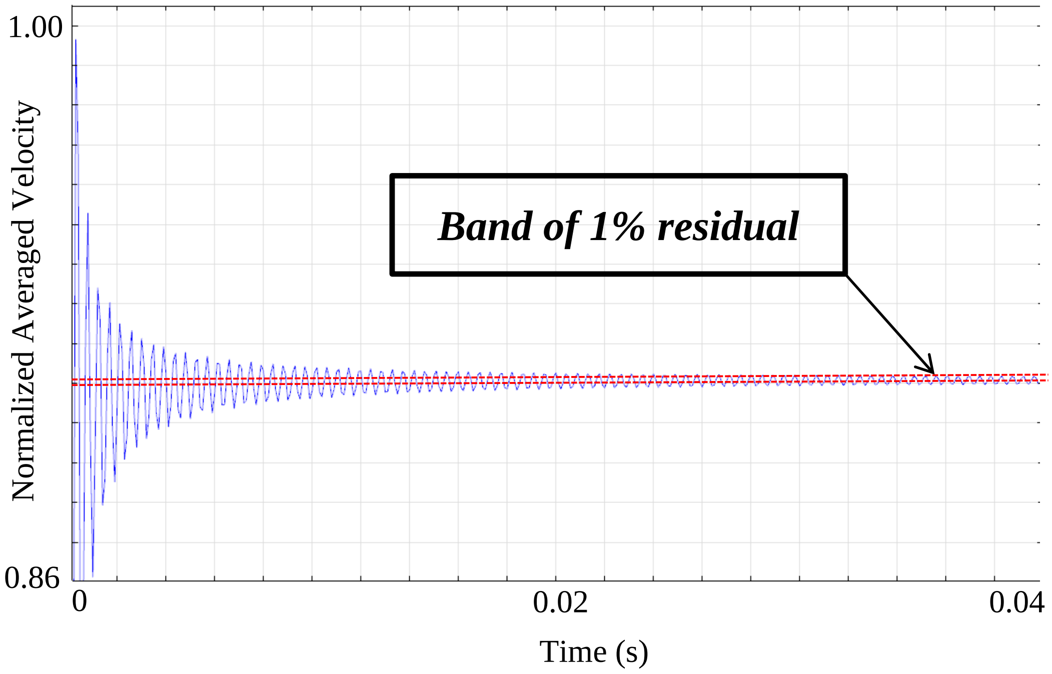

Figure 18 Time averaged velocity history at *x = 0, y = 5b*

The results show that the average converges to a residual of less than 1% (with respect to the average velocity as calculated over all time steps) within 45 cycles, (*t = 0.04s*) of actuator oscillation. Results for other test cases indicated convergence for the entire flow field nominally took up to 350 cycles or less. All simulations were therefore set to run up to 450 cycles of actuator oscillation.

In order to establish the appropriate density of mesh elements, a spatial convergence test was conducted. The growth rate of elements was adjusted to control element density as flow field results close to the orifice were observed. When the contours from successive iterations approached a difference of less than 0.1 m/s, the solution was considered mesh converged. An illustration of this process is shown below. The results for three different element growth rates; 1.01 (Figure 21), 1.05 (Figure 20) and 1.10 (Figure 19) are shown. A growth rate of 1.01 was chosen for all the simulations as it was the point at which mesh convergence for the entire field was observed and flow features throughout the computational domain were distinguishable.

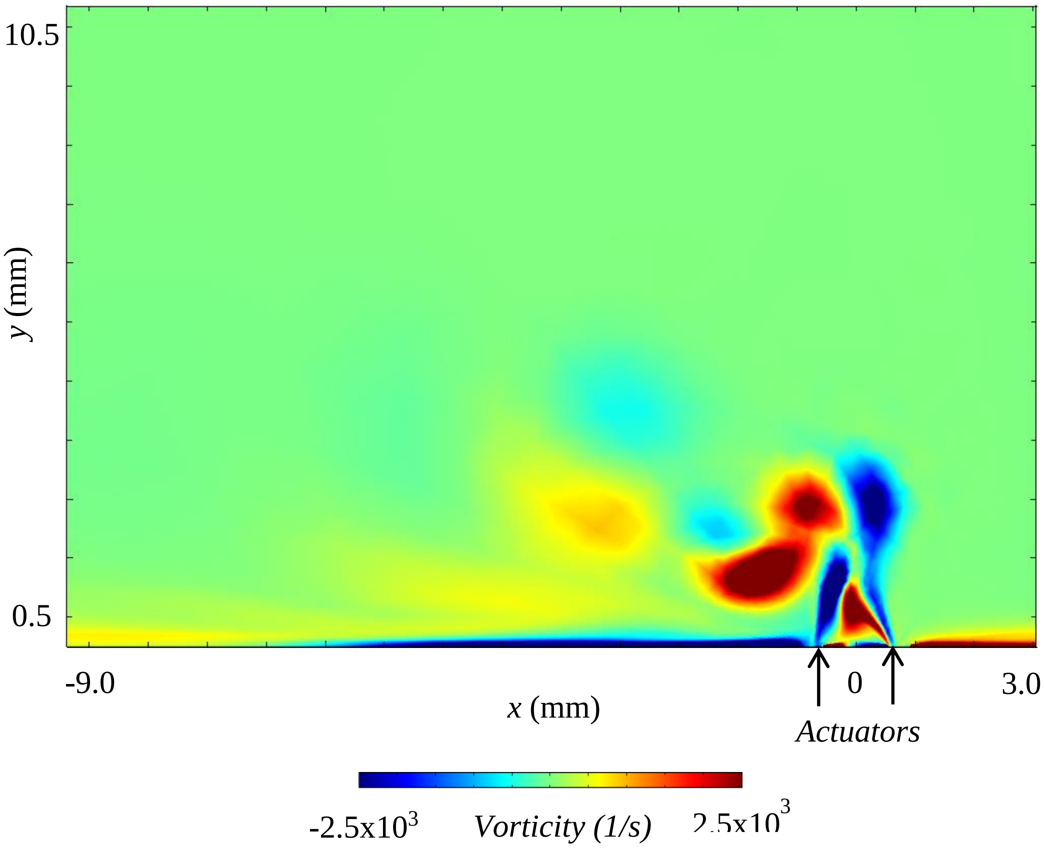

Figure 19 Vorticity contours for simulated case R = 2.4, φ = 0, s = 2.5 b at t/T = 56 and element growth rate of 1.1

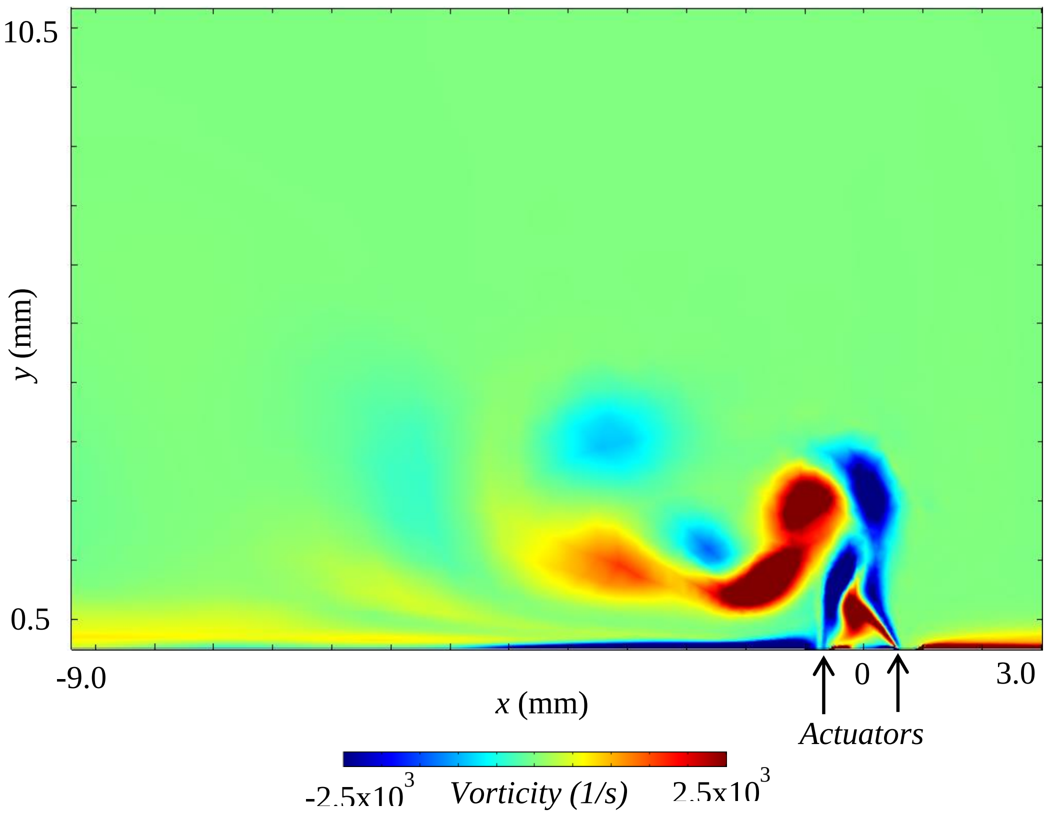

Figure 20 Vorticity contours for simulated case *R = 2.4, φ = 0, s = 2.5 b* at *t/T* = 56 and element growth rate of 1.05

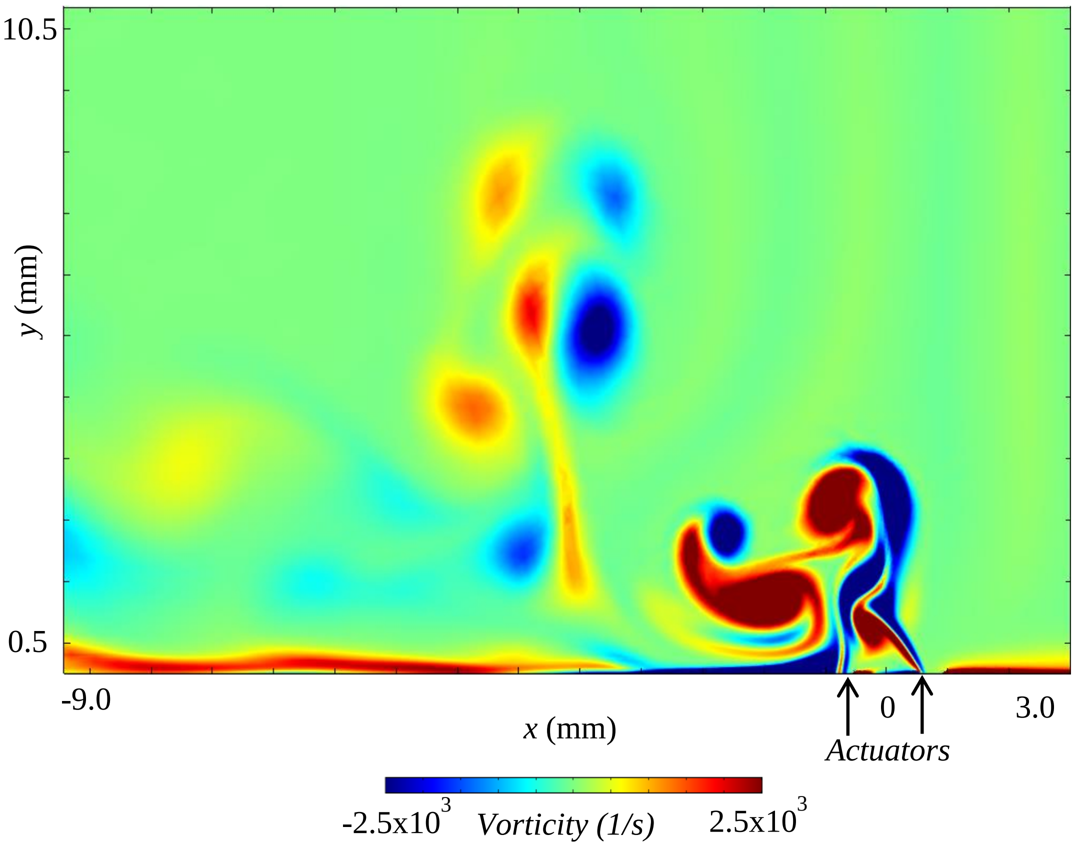

Figure 21 Vorticity contours for simulated case *R = 2.4, φ = 0, s = 2.5 b* at *t/T* = 56 and element growth rate of 1.01

2.2.2: Perturbation Solution

Methodology

The second method used as part of this study is based on a stream vorticity formulation of the Navier Stokes equation as used by Schroeder et al. (Schroeder, et al., 1989). They used the method to predict flow over an oscillating airfoil pitching at small angles. The pitching motion of the airfoil was modeled as a small perturbation boundary condition. The method uses a simplified version of the stream-vorticity formulation split into steady and unsteady components. The fluidic domain is divided into small grid elements, and the flow itself is analyzed in terms of steady and unsteady components. The steady flow field is described by the Navier-Stokes equations and is therefore non-uniform and nonlinear. In addition to this, the steady flow field is independent of the unsteady flow field. The small perturbation unsteady viscous flow is described by a system of linear (for some cases) partial differential equations which are coupled to the steady flow field. This coupling models the dependence of the unsteady flow on the steady flow.

The model developed by Fleeter and Schroeder assumed that the effect of any perturbation in the flow (such as actuation) was localized and did not influence the steady part of the flow. For the purposes of applying this method to synthetic jets in cross-flows, a slightly different approach was used. Starting with the unsteady viscous Navier-Stokes equations in their non-dimensional form we have Equation 7.

$$\bar{u}_x + \bar{v}_y = 0;\ (a)$$

$$k\bar{u}_t + \overline{u}\bar{u}_x + \overline{v}\bar{u}_y = -\bar{p}_x + \frac{\bar{u}_{xx} + \bar{u}_{yy}}{Re};\ (b)$$

$$k\bar{v}_t + \overline{u}\bar{v}_x + \overline{v}\bar{v}_y = -\bar{p}_y + \frac{\bar{v}_{xx} + \bar{v}_{yy}}{Re};\ (c)$$

Equation 7

Here $\bar{u}$, $\bar{v}$ and $\bar{p}$ denote the non-dimensional *x*-velocity component, the *y*-velocity component and the pressure, respectively. The term k represents the non-dimensional frequency and is given as $k = \frac{\omega c}{U}$; where *c* is the characteristic scaling length (on the order of the interaction domain), *ω* is the frequency of the actuation, and U is the free-stream velocity. The cross-flow Reynolds number, Re is given as $Re = \frac{Uc}{\nu}$; where *υ* is the kinematic viscosity of the operating fluid. The Stream and Vorticity functions are given by Equation 8 as follows.

$$\bar{\zeta} = \bar{v}_x - \bar{u}_y;\ (a)$$

$$\bar{u} = \bar{\psi}_y, \bar{v} = -\bar{\psi}_x; (b)$$

Equation 8

Here $\bar{\zeta}$ represents the non-dimensional vorticity function and $\bar{\psi}$ denotes the non-dimensional stream function. Using Equation 8 it is possible to reformulate Equation 7 in what is known as the standard Stream-Vorticity formulation of the Navier-Stokes equations as given by Equation 9.

$$Vorticity: \nabla^2\bar{\zeta} = \bar{\zeta}_{xx} + \bar{\zeta}_{yy} = Re\left(k\bar{\zeta}_t + \bar{\psi}_y\bar{\zeta}_x - \bar{\psi}_x\bar{\zeta}_y\right);\ (a)$$

$$Stream: \nabla^2\bar{\psi} = -\bar{\zeta}; (b)$$

Equation 9

By manipulating the Navier Stokes equations in this particular way the number of dependent variables (u, v and p) is reduced from three to a total of 2 (ζ and ψ). Assuming that any perturbations in the flow are of harmonic nature (actuation satisfies this assumption) the flow field can be decomposed into steady and unsteady components as shown below in Equation 10.

$$\bar{\zeta}(x,y,t) = \zeta(x,y) + e^{it}\xi(x,y);\ (a)$$

$$\bar{\psi}(x,y,t) = \Psi(x,y) + e^{it}\psi(x,y);\ (b)$$

$$\bar{u}(x,y,t) = U(x,y) + e^{it}u(x,y);\ (c)$$

$$\bar{v}(x,y,t) = V(x,y) + e^{it}v(x,y);\ (d)$$

$$\bar{p}(x,y,t) = P(x,y) + e^{it}p(x,y);\ (e)$$

Equation 10

The first terms on the left hand side of Equation 10 represent the steady components while the second terms represent the unsteady components of each of the quantities. We can now substitute the formulation of stream function and vorticity as described by Equation 10 back into Equation 9 to obtain Equation 11 that contains the unsteady and steady components. These components can then be separated and simplified.

$$\zeta_{xx} + e^{it}\xi_{xx} + \zeta_{yy} + e^{it}\xi_{yy}$$
$$= Re\big(kie^{it}\xi + \left(\Psi_y + e^{it}\psi_y\right)\left(\zeta_x + e^{it}\xi_x\right)$$
$$+ \left(\Psi_x + e^{it}\psi_x\right)\left(\zeta_y + e^{it}\xi_y\right)\big)$$

Equation 11

Separating the unsteady and steady components we obtain two sets of the equations that describe the steady and unsteady flow fields as shown in Equation 12.

$$Steady\ flow\ field$$
$$\nabla^2\zeta = Re(\Psi_y\zeta_x + \Psi_x\zeta_y)$$
$$Unsteady\ flow\ field$$
$$\nabla^2\xi = Re(ki\xi + \Psi_y\xi_x + \psi_y\zeta_x + \Psi_x\xi_y + \psi_x\zeta_y + e^{it}(\psi_x\xi_y + \psi_y\xi_x))$$

Equation 12

The advantage decomposing the flow field in the way as shown above is that if the perturbation is small enough (small unsteady component in the flow field) the product of the unsteady terms $\psi_x\xi_y$ and $\psi_y\xi_x$ becomes very small and can be neglected. This allows us to re-write Equation 12 as follows:

$$\nabla^2\xi = Re(ki\xi + \Psi_y\xi_x + \psi_y\zeta_x + \Psi_x\xi_y + \psi_x\zeta_y)$$

Equation 13

The formulation shown in Equation 13 can also be used to develop a linearized and locally analytic solution for each grid element. This solution can then be assembled for all grid elements to obtain the overall flow field. While the benefits of having a part analytical solution are significant, the speed improvements usually do not justify the loss in accuracy. Therefore for this section the full set of the steady and unsteady stream-vorticity equations were solved numerically. The boundary conditions for this particular formulation were slightly different from the ones used for the full CFD model. Instead of modeling the complete cavity the flow from the actuators is modeled as a sinusoidal perturbation applied as a boundary condition to a nozzle only. This simplification allows for significantly faster solutions as the flow inside the cavity is not computed. A linearized analytical solution based on this formulation will be developed and studied in following section.

Flow Domains, Boundary & Initial Conditions and Meshing

Instead of modeling the cavity, nozzle and interaction domain this particular section looks at modeling the effect of actuation as a harmonic perturbation applied on the nozzle section of the actuator only. This reduced the number of elements used in the simulation by 27%. The boundary condition was calculated from the results of the full numerical simulation. The interaction domain is identical to the one described in section 2.2.1. The advantage of modeling the nozzle as opposed to modeling the interaction domain alone is that impedance effects associated with phasing and changing the velocity ratio are still captured (as will be shown in the results section). This is due to the fact that output velocity at the orifice exit is not a fixed boundary condition. Its value therefore depends on how the flow field develops in the interaction domain. A schematic illustrating the new domain and boundary conditions is shown in Figure 22. The mesh used for this solution was exactly identical to the one used for the full actuator simulation described in section 2.2.1. All boundary conditions that are not marked in Figure 22 were modeled as no-slip walls. The temporal convergence technique used in section 2.2.1 was used to determine the number of cycles needed for a converged solution.

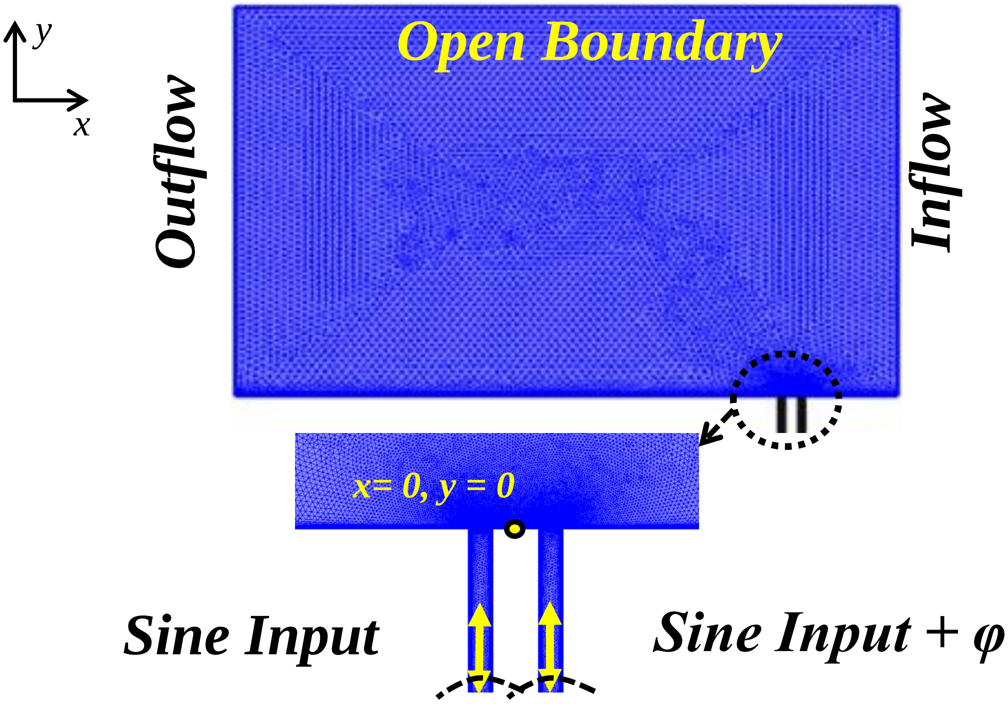

Figure 22 Mesh and boundary conditions for perturbation model

2.2.3: Analytical Solution

Methodology

A closed form analytical solution was developed based upon the Stream-Vorticity formulation of the non-dimensional Navier-Stokes equations shown in Equation 7. The solution is based on a plane wave solution originally developed by Hui (Hui, 1987) as a solution to periodic suction and blowing applied to a 2D flat plate in a cross-flow. In the physical sense Hui’s solution represents a uniform cross-flow with an exponentially decaying perturbation. Starting out with a slightly different form of the non-dimensional Stream-Vorticity formulation of the Navier-Stokes equation than that presented in Equation 9, we obtain Equation.

$$Vorticity: \nabla^2\bar{\zeta} = \bar{\zeta}_{xx} + \bar{\zeta}_{yy} = Re\left(k\bar{\zeta}_t + \bar{u}\bar{\zeta}_x - \bar{v}\bar{\zeta}_y\right); (a)$$

$$Stream: \nabla^2\bar{\psi} = -\bar{\zeta}; (b)$$

Equation 14

We now assume that the vorticity distribution is proportional to the stream function perturbed by a uniform flow value equal to that of the cross-flow, *U*. This results in Equation 15.

$$\bar{\zeta} = K(\bar{\psi} - \bar{U}\bar{y})$$

Equation 15

Here $\bar{U}$ is the non-dimensional uniform cross-flow velocity, $\bar{y}$ represents the non-dimensional *y*-coordinate and K is the proportionality constant. Our stream function now satisfies the following condition:

$$\nabla^2 \bar{\psi} = K(\bar{\psi} - \bar{U}\bar{y})$$

Equation 16

We now make a substitution. Let $\Psi = \psi - \bar{U}\bar{y}$. With this substitution the new variable Ψ will satisfy Equation 16 in the following way:

$$\nabla^2\Psi = K\Psi$$

Equation 17

The purpose of the substitution is to render Equation 16 homogenous. Now starting with the vorticity transport equation and substituting the vorticity term with $K\Psi$, to obtain the following relation:

$$\frac{\partial \Psi}{\partial t} + \overline{U}\frac{\partial \Psi}{\partial x} = K\Psi$$

Equation 18

Equation 18 is a first order partial differential equation for which the general solution is given in the following form:

$$\Psi(X, \bar{y}, t^*) = G(X, \bar{y})e^{kt^*}$$

Equation 19

Where *G* is a function of *X* and $\bar{y}$, *X* is the transformed dimensional variable such that $X = \bar{x} - \overline{U}t^*$ and $t^* = \frac{tU}{c}$ is the non-dimensional time. Any solution of Equation 18 must also satisfy Equation 17. We therefore substitute this solution into Equation 17 and obtain the reduced wave equation, also known as the Helmholtz equation.

$$\frac{\partial^2 G}{\partial x^2} + \frac{\partial^2 G}{\partial y^2} = KG$$

Equation 20

Now we consider another transformation for the function *G*. Let $g(\varsigma)$ be a function such that:

$$G(x, y) = g(\varsigma); \text{(a)}$$

$$\varsigma = Xcos(\theta) + \bar{y}sin(\theta); (b)$$

Equation 21

In the transformation in Equation 21 the variable θ represents that angle that plane wave perturbation makes with the positive *x*-axis. Using this transformation we evaluate each of the individual terms of the Helmholtz equation as follows:

$$\frac{\partial G}{\partial x} = \cos(\theta) * \frac{\partial g}{\partial \varsigma}; (a)$$

$$\frac{\partial^2 G}{\partial x^2} = \cos^2(\theta) \frac{\partial^2 g}{\partial \varsigma^2}; (b)$$

$$\frac{\partial^2 G}{\partial y^2} = \sin^2(\theta) \frac{\partial^2 g}{\partial \varsigma^2}; (c)$$

$$\frac{\partial^2 G}{\partial x^2} + \frac{\partial^2 G}{\partial y^2} = \cos^2(\theta) \frac{\partial^2 g}{\partial \varsigma^2} + \sin^2(\theta) \frac{\partial^2 g}{\partial \varsigma^2} = g''; (d)$$

Equation 22

With this transformation the Helmholtz equation (Equation 18) now becomes:

$$g''(\varsigma) - Kg(\varsigma) = 0$$

We now let the proportionality constant $K = -k^2 < 0$ and with that assumption the solution of Equation 22 is given as:

$$g(\varsigma) = A(\theta)\cos(k\{\varsigma + B(\theta)\});$$

$$-180° \leq \theta \leq 180°$$

Equation 23

A and *B* are coefficients dependent upon the value of θ. Using Equation 23 and Equation 22 we can obtain an expression for *G*.

$$G(X, \bar{y}) = A(\theta)\cos(k\{\varsigma + B(\theta)\})$$

Equation 24

Now using Equation 24 and Equation 19 we can evaluate Ψ as follows:

$$\Psi = A(\theta)\cos(k\{\varsigma + B(\theta)\}) * e^{Kt^*}; (a)$$

$$\Psi = A(\theta) * \cos(k\{Xcos(\theta) + \bar{y}\sin(\theta) + B(\theta)\}) * e^{-k^2 t^*}; (b)$$

Equation 25

Recognizing that $\Psi = \psi - \bar{U}\bar{y}$ and $X = \bar{x} - \bar{U}t^*$ it is possible now to recover the stream function ψ, as well as our velocity components using Equation 8 (b).

$$\psi(\bar{x}, \bar{y}, t^*) = \bar{U}\bar{y} + A(\theta)e^{-k^2t^*}\cos(k\{(\bar{x} - \bar{U}t^*)\cos(\theta) + \bar{y}sin(\theta) + B(\theta)\})\,; (a)$$

$$\bar{u} = \bar{U} - A(\theta)ke^{-k^2t^*}\sin(\theta)\sin(k\{\varsigma_0 + B - \bar{U}t^*\cos(\theta)\})\,; (b)$$

$$\bar{v} = A(\theta)ke^{-k^2t^*}\cos(\theta)\sin(k)\{\varsigma_0 + B - \bar{U}t^*\cos(\theta)\}; (c)$$

$$\varsigma_0 = \bar{x}cos(\theta) + \bar{y}sin(\theta); (d)$$

Equation 26

The values of A and B will be determined in the following section through application of boundary conditions. It is important to understand the physics that it is being modeled by Equation 26. The stream function as predicted by this model is a sinusoidal perturbation superimposed on steady stream value. The strength of the perturbation appears to oscillate and decay in time at a rate proportional to the non-dimensional frequency, with high frequency oscillations subjected to higher damping rates. The strength of the perturbation also varies spatially along the direction of propagation.

This analytical form of perturbation solution requires a set of boundary conditions that can be described analytically. While several analytical approximations to the velocity distribution at the orifice can be found in literature, there is very little information on modeling two closely placed synthetic jets for which the phase and spacing are variable. Most of the approximations found in literature for the single actuator case based on experimental data. For instance Smith and Glezer (Smith & Glezer, 1998) measured the velocity distribution 10 mm above the orifice using CTA anemometry (shown in Figure 23). They then fit a hyperbolic cosine function to the experimental data. Kral et al. (Kral, et al., 1997) used a smoothed top-hat function with a sinusoidal time component to do the same.

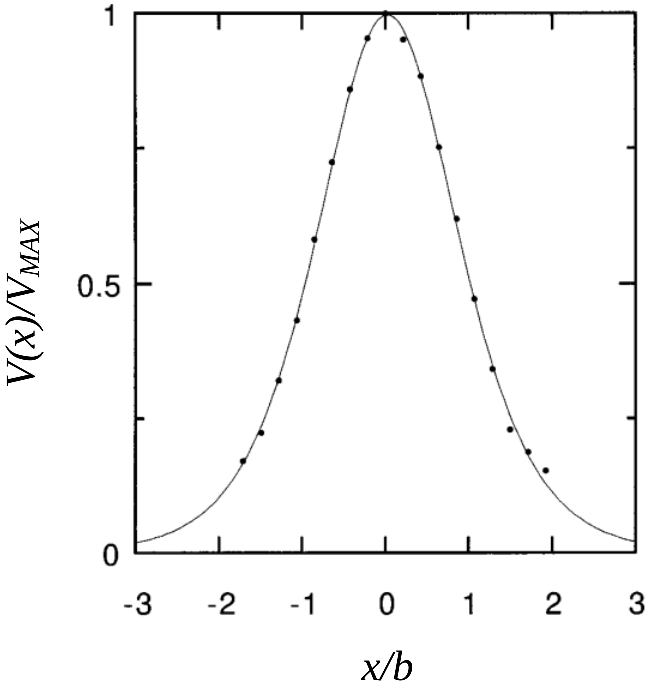

Figure 23 Least squares fit of a hyperbolic cosine to experimental velocity at height *y = 20 b* (Smith & Glezer, 1998)

Experimentally obtaining the velocity distribution at the orifice is a challenging task. The Constant temperature Anemometry (CTA) system that was available had a measuring surface that was comparable in size to the orifice dimensions. Similarly the available PIV system did not have the adequate optics to properly resolve the velocity distribution at the orifice. The strong reflection issues caused by being close to the surface also presented an issue. In addition to these challenges the approximation needed to be a continuous analytical expression that would incorporate the effect of the location of the actuators with respect to one another, as well as the effects of how they were phased.

Boundary conditions, specific solution and model limitations

In order to satisfy all the requirements mentioned in the previous section the velocity was initially modeled as normally distributed about the center of the orifice with sinusoidal oscillatory magnitude of reduced frequency *k*, amplitude V_0, and variance *p* as shown in Figure 24. Ideally at the surface of the orifice right along the wall where *x* = *0*; the jet velocity would be perfectly normal to the *x*-axis and the cross-flow boundary layer velocity (the local *u* value) would be 0 as depicted in Figure 24. The formulation of the solution presented in Equation 26 does not allow for zero velocity at *x* = 0, without restricting the type of perturbation that can be modeled. The perturbation generated by actuation initially travels at a specific angle *θ*, with respect to the positive *x*-axis. At the wall this would be very close to 90°. A strictly perpendicular perturbation is however not admissible as it results in an inconsistency close to the wall based upon the $\cos(\theta)$ term in Equation 26, if $\theta = 90°$ the $\cos(\theta)$ term vanishes.

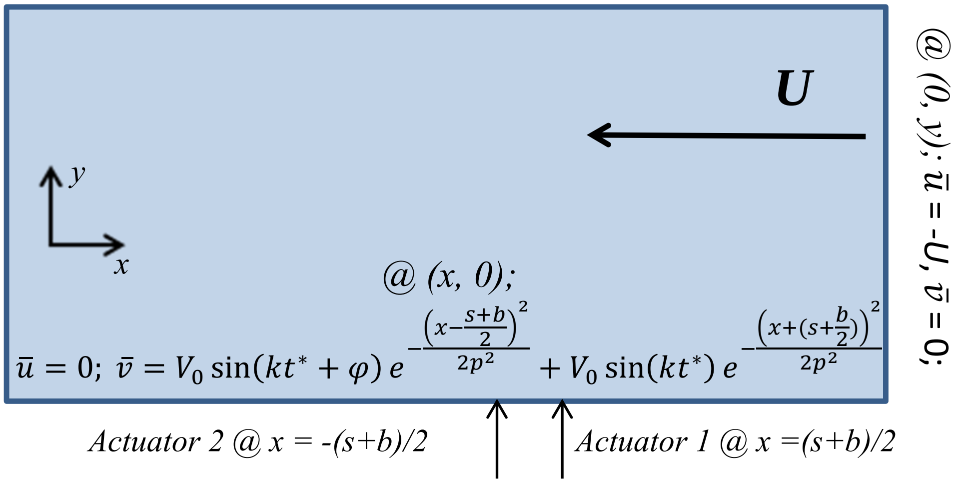

Figure 24 Schematic of ideal boundary conditions and interaction domain for analytical model

The solution to this issue highlights one of the several limitations associated with the analytical solution to the perturbation model. The velocity at the boundary condition must be corrected through the use of empirical information that was obtained through numerical simulations and experimentation. PIV was used to determine the initial trajectory of the plume to specify the angle θ along the lower boundary. The angle was used to modify the boundary conditions on the bottom edge of the interaction domain and the modified system is presented in Figure 25. Measuring the angle θ this way creates a dependency on experimental data that varies with the phase and velocity ratio.

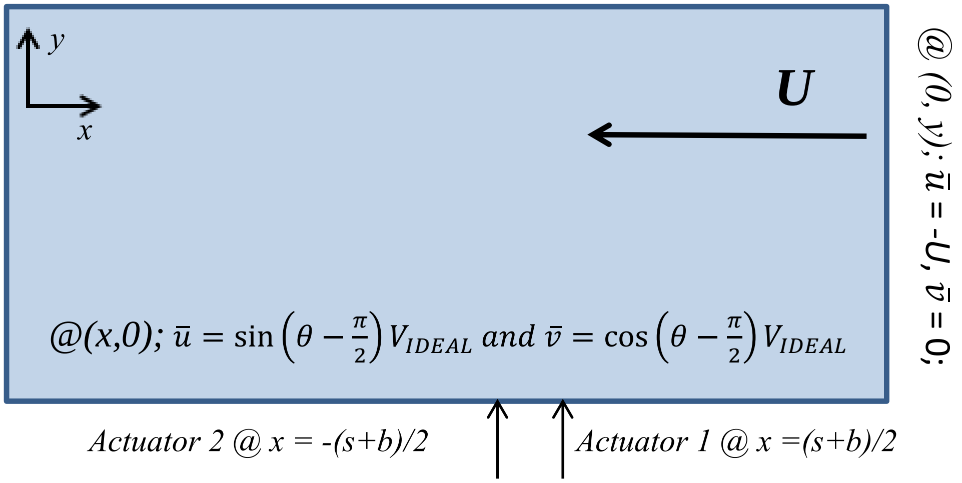

$$V_{IDEAL} = V_0 \sin(kt^* + \varphi)\, e^{-\frac{\left(x - \frac{s+b}{2}\right)^2}{2p^2}} + V_0 \sin(kt^*)\, e^{-\frac{\left(x + \left(\frac{s+b}{2}\right)\right)^2}{2p^2}}$$

Figure 25 Modified boundary conditions used for analytical modeling

The variance p was determined through CFD performed for a single actuator operating in quiescent environment. The velocity amplitude V_0 was calculated by fitting a case of simulated analytical results to PIV data. The resulting boundary conditions are shown in the Figures below.

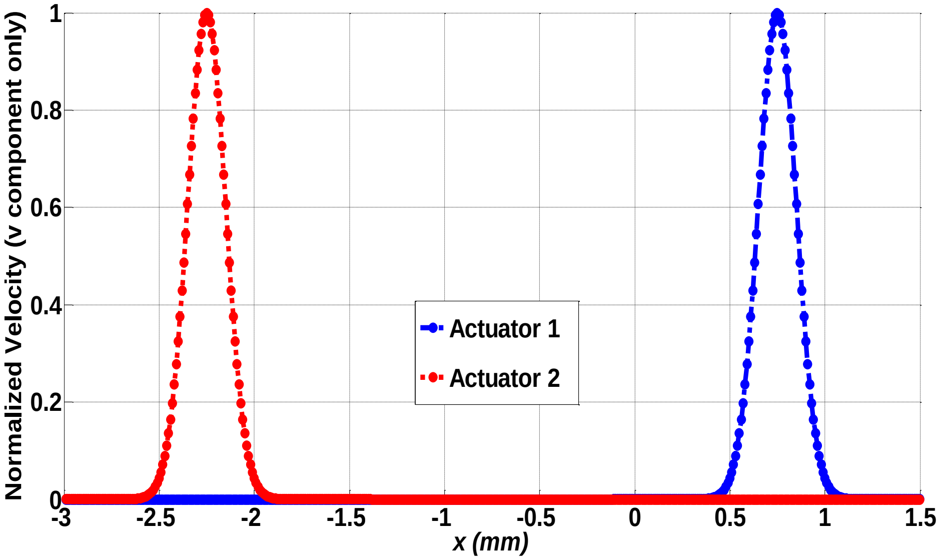

Figure 26 Plot of the ideal boundary condition along *y = 0* for *s* = 2.5*b*, *φ* = 0, and *t/T* = 0.0560 (No dependency on velocity ratio, *R*)

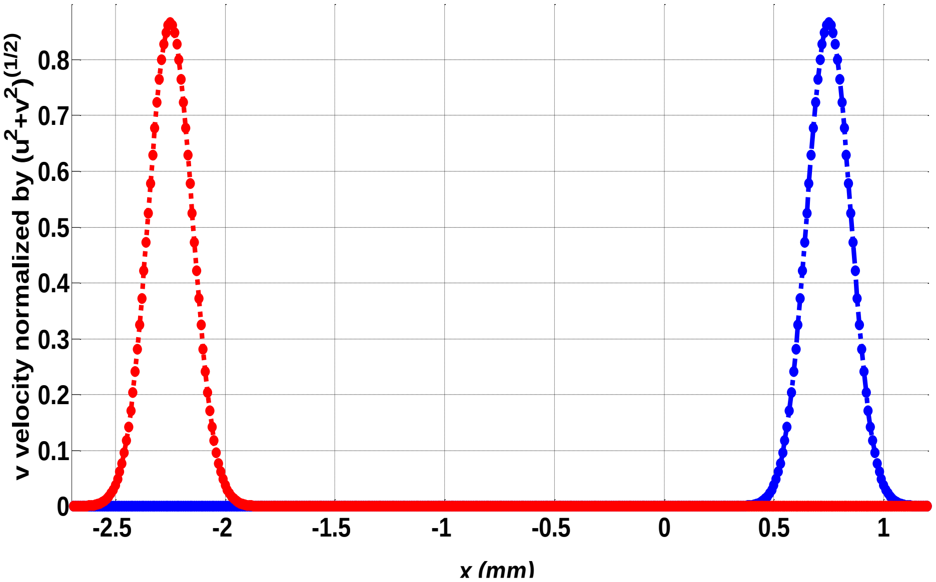

Figure 27 Plot of the $\overline{v}$ velocity for modified boundary condition along *y* = 0 for *s* = 2.5*b*, *φ* = 0, and *t/T* = 0.0560 (*θ* = 30° obtained from PIV; magnitude dependency on *R*)

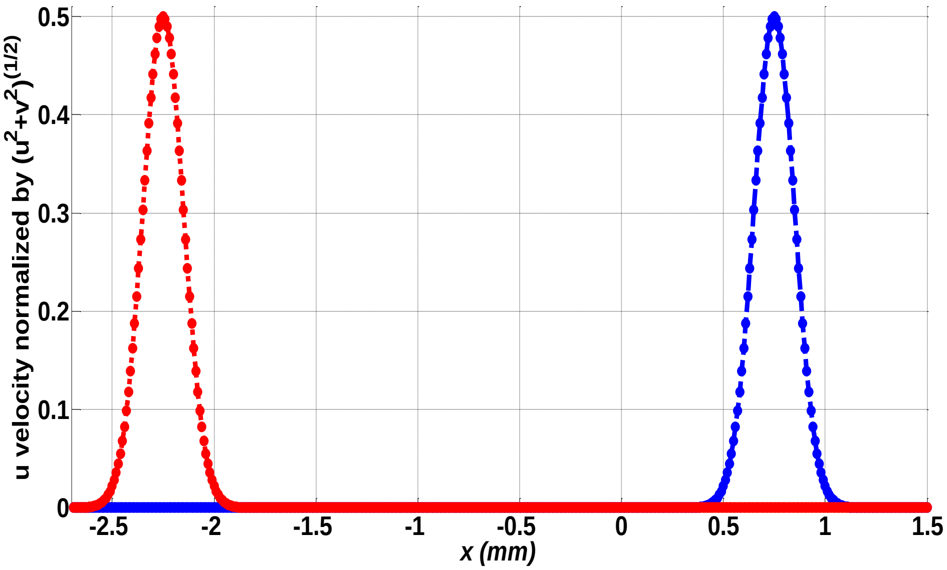

Figure 28 Plot of the $\bar{u}$ velocity for modified boundary condition along $y = 0$ for $s = 2.5b$, $\varphi = 0$, and $t/T = 0.0560$ ($\theta = 30°$ obtained from PIV; magnitude dependency on R)

With these boundary conditions it is now possible to calculate the value for the constants *A* and *B*, and hence the exact solution for each case of parameter. The dependency of the model on empirical data meant that in order to use this model to perform a complete parameter sweep as discussed in Table 2 knowledge of the initial trajectory had to be present either through CFD or experiment.

2.3 Qualitative results from modeling: Flow features

2.3.1: CFD prediction and analysis of flow features

Single Actuator in Cross-Flow

An initial approach to determining the accuracy of the models was to observe if they would qualitatively capture the flow features that have been observed by previous experimental and computational studies. In addition to this studying these flow features also provided valuable insight into important aspects of the jet-jet-cross-flow interactions. All the results presented in this section are for a fixed velocity ratio of $R = 2.4$.

The vortices created through shear roll up play an important part in determining the overall characteristics of the flow field. Starting with the results from a single actuator in a cross-flow we observe the evolution of the vorticity field in the following sequence of figures below. For the single actuator case we place the origin such that the actuator orifice center is located at $x = 1.5b$. Shown in Figure 29 is the formation of the vortex pair in its early stages. At this point the jet flow has not separated from the cavity and the vortex pair has not yet reached its peak size. Right after the end of the ejection cycle the vortex pair begins to separate and at this point it has reached its maximum size/strength. In addition to the growth the orientation of the pair is in the process of reversing as shown in Figure 30.

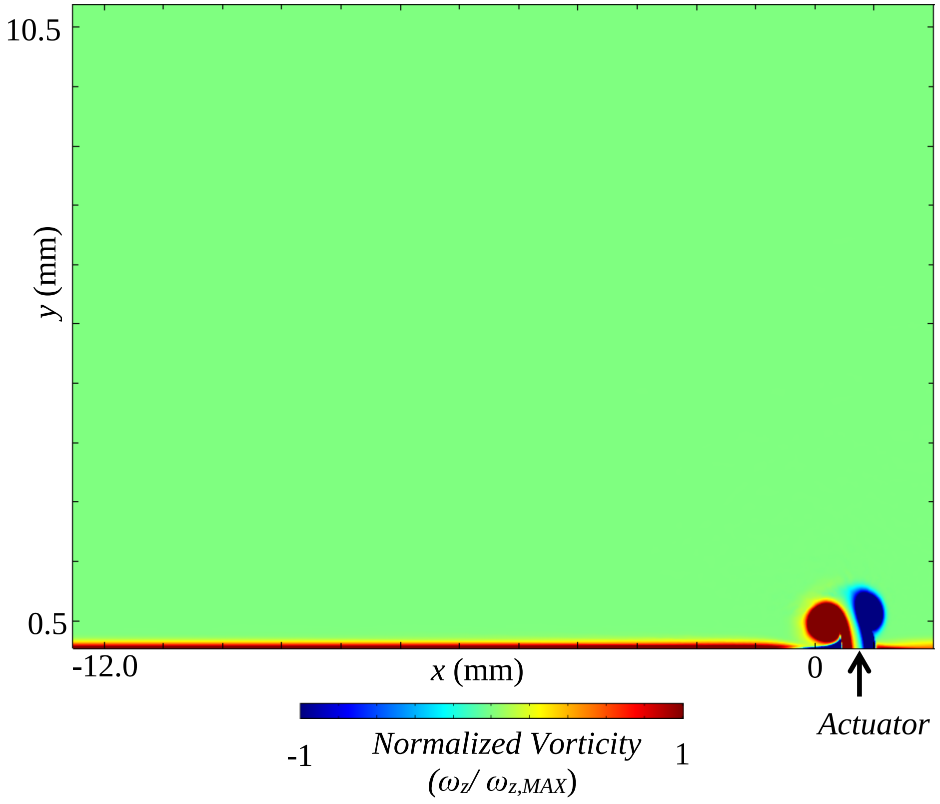

Figure 29 Vorticity contours for single SJA @ *t/T* = 0.25 (midway through ejection cycle)

Error! Reference source not found.

Figure 30 Vorticity contours for single SJA @ *t/T* = 0.52 (beginning of suction phase)

We now see that clockwise vortex (shown in blue) is further from the orifice in comparison to the counterclockwise vortex (red). The induced velocity due to this vortex is in the positive y direction and its distance from the orifice is smaller by about one core diameter making the net induced velocity at the orifice positive in the upward direction. The effect of the cross-flow is to deflect the vortex in the immediate downstream neighborhood of the jet and reverse the orientation of the pair. This vortex pair is deflected back into the boundary layer, where at the end of the suction cycle is pairs up with a negative vorticity present in the boundary layer formed in the immediate wake of the jet.

This continuing interaction is shown in Figure 31 which shows the vorticity contours at a time that is close to the end of the suction cycle. The counterclockwise vortex (red) appears to be in the process of switching its partner as the vorticity appears to recirculate in the wake. This process is complete almost a ¼ of the way into the following ejection cycle, the results for which are shown in Figure 32. This switching results in a new pair in which the vortices are asymmetric in size and strength. The process continues for several successive cycles. As time increases this transient response dies out and the jet approaches a steady cyclic response the beginning of which is shown in Figure 34. As the newly formed vortex pair advects away from the orifice it now begins to deflect in the direction of the cross-flow. During the process the inner (counterclockwise) vortex begins to stretch due to the difference in advection velocities (Figure 35).

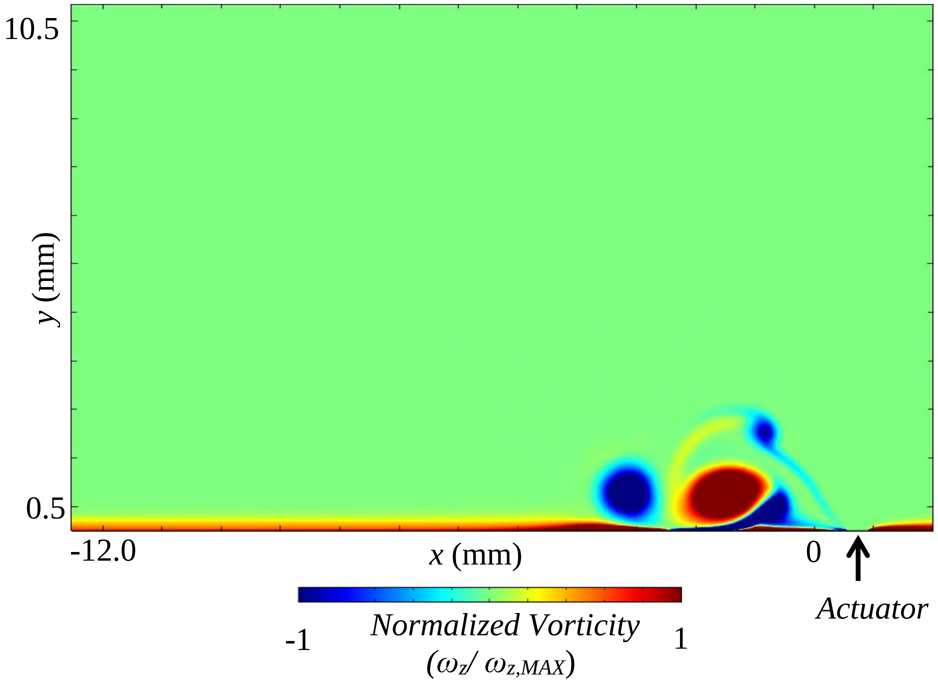

Figure 31 Vorticity contours for single SJA @ *t/T* = 0.94 (close to the end of the ejection cycle)

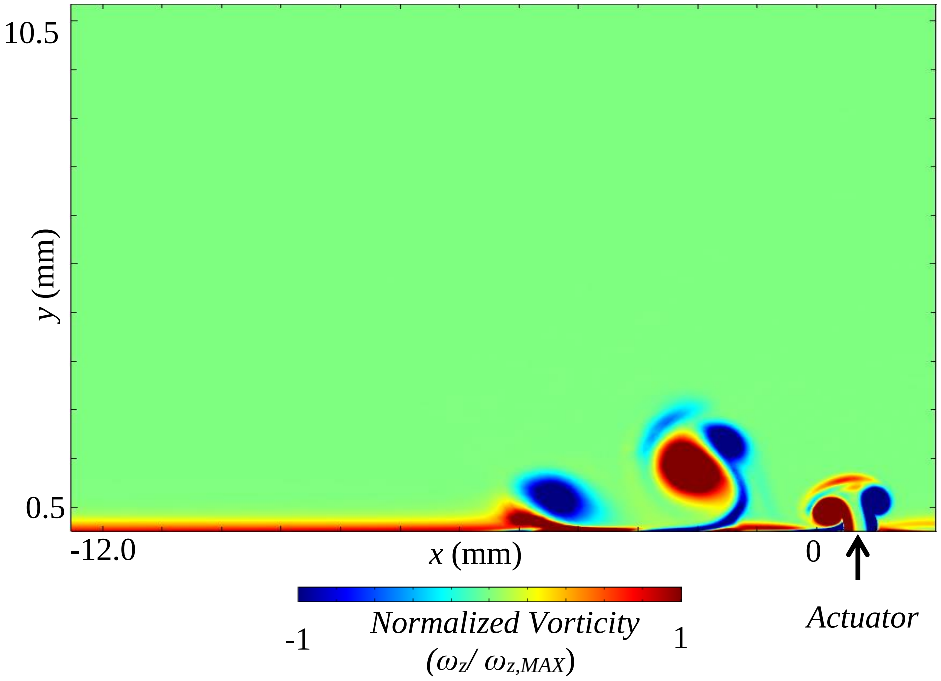

Figure 32 Vorticity contours for single SJA @ *t/T* = 1.23

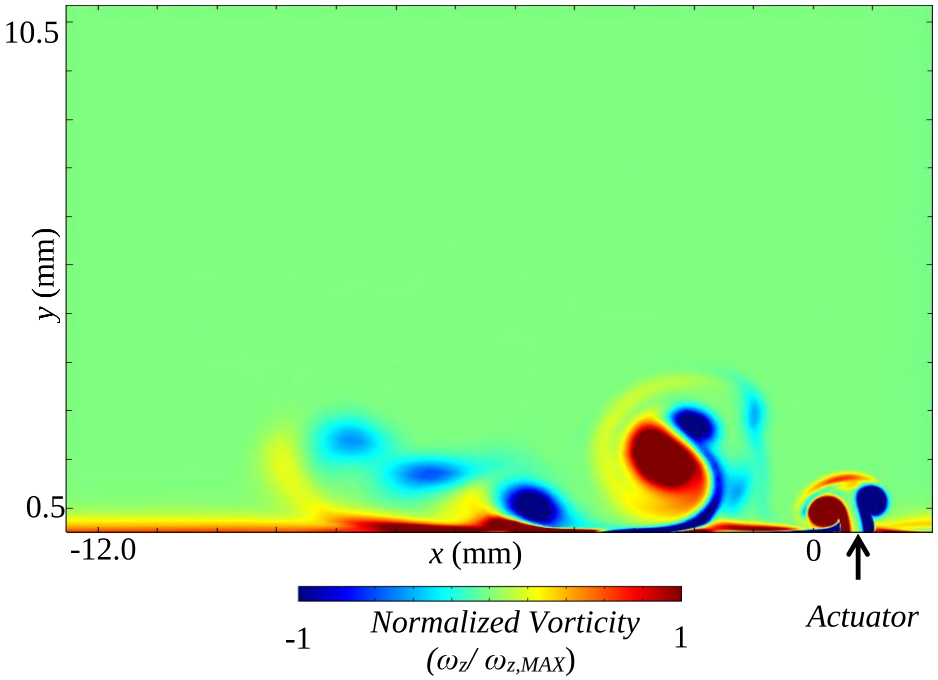

Figure 33 Vorticity contours for single SJA @ *t/T* = 2.25

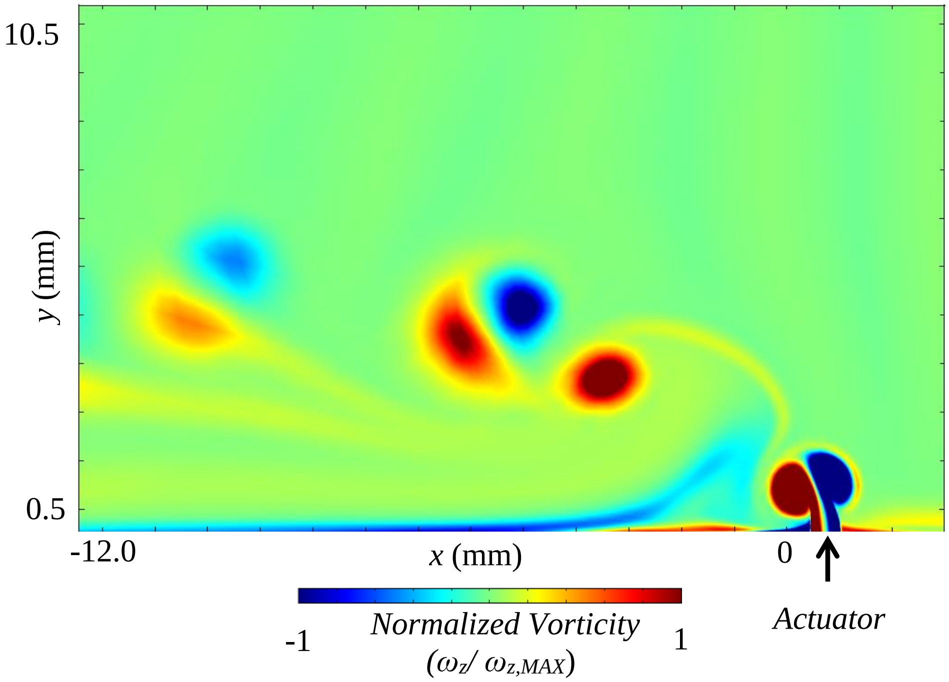

Figure 34 Vorticity contours for single SJA @ *t/T* = 37.52

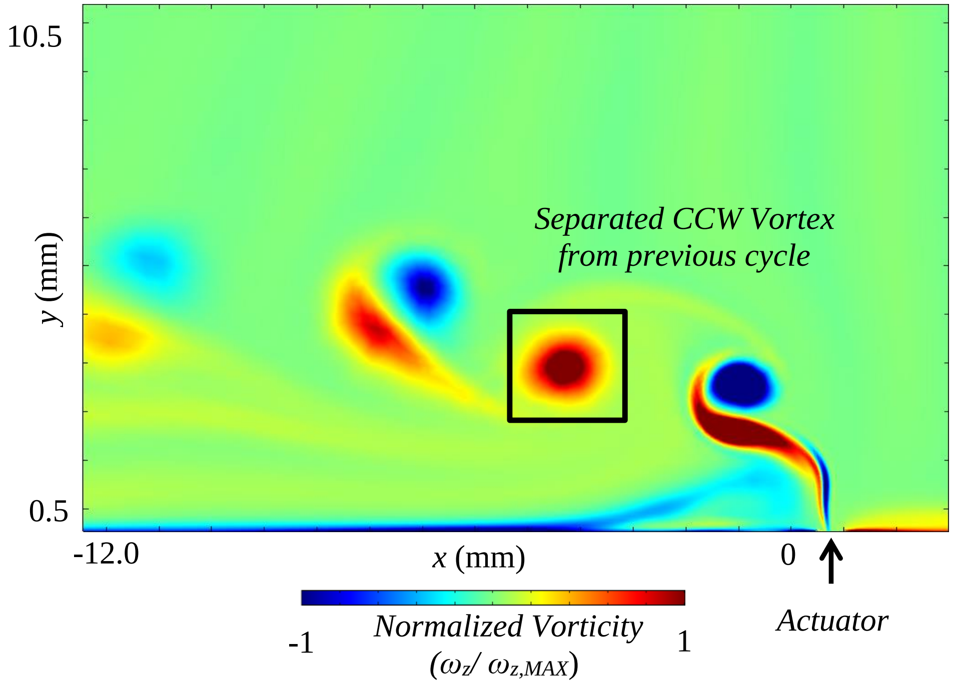

Figure 35 Vorticity contours for single SJA @ *t/T* = 37.68

As the pair advect further the clockwise vortex (shown in blue) separates and surpasses its counterclockwise counterpart (shown in red) which rolls into a separated individual counterclockwise vortex as shown in Figure 36. At this point the blue vortex pairs with the red separated vortex from the previous cycle (shown in Figure 35). The process then repeats itself and the solution has approached a steady state. The newly united pair then continues to advect along the plume weakening as it undergoes transition to turbulence.

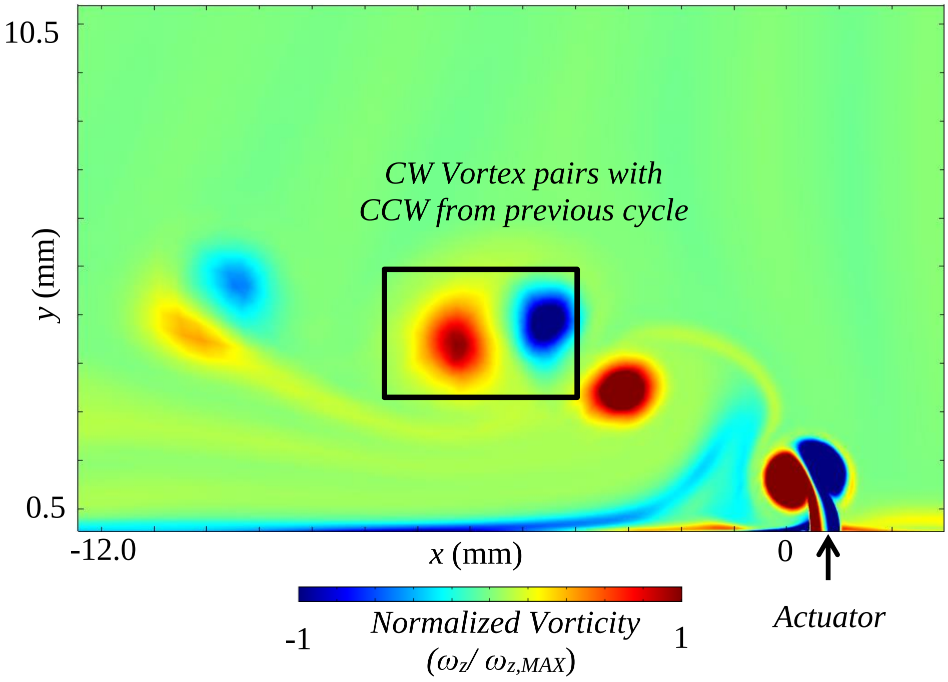

Figure 36 Vorticity contours for single SJA @ *t/T* = 38.26

Dual Actuators in Cross-Flow

After validating the CFD qualitatively for the single actuator the flow features for the two actuator case were also studied. Instead of studying the transient response we focus on the steady state response. The vorticity contours for *t/T* = 78.28 (statistical convergence was seen at 45 cycles) are shown in Figure 37. The counter rotating pairs form right above each orifice and advect away from the orifices. For purposes of convenience we introduce a new notation to identify the vortices. We refer to the counterclockwise and clockwise rotating vortices produced by actuator 1 as CCW1 and CW1. Likewise the counterclockwise and clockwise rotating vortices are referred to as CCW2 and CW2 respectively. The origin is now situated between the two orifices per the convention described in Figure 16. We start the analysis after the transients have died out a quarter of the way into the ejection cycle at $t/T = 78.28$ (Figure 37).

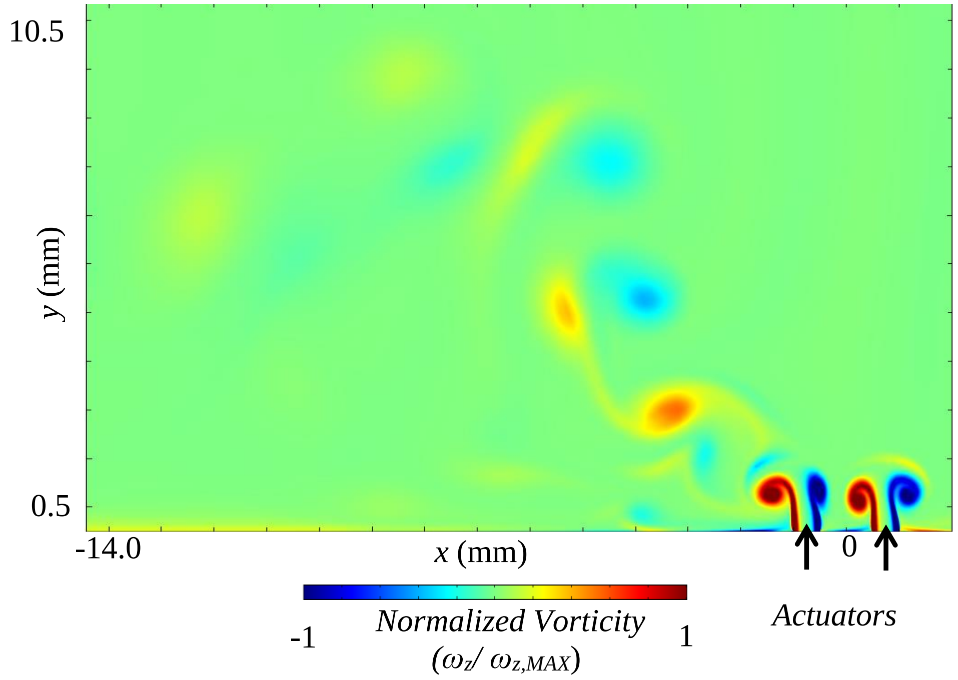

Figure 37 Vorticity contours for dual SJA operating in phase @ $t/T = 78.28$

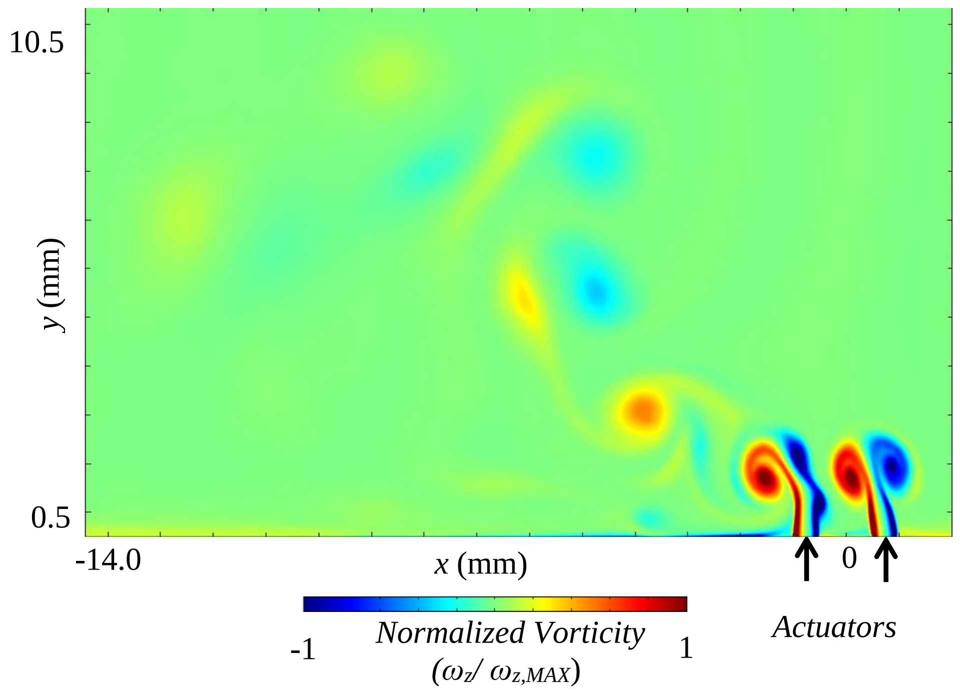

Figure 38 Vorticity contours for dual SJA operating in phase @ *t/T* = 78.40

At *t/T* = 78.400 (Figure 38) we observe that under the combined influence of CCW1, CCW2, CW1 and the cross-flow, CW2 begins to stretch and divide into two smaller vortices as shown in Figure 39. We now refer to the two smaller vortices as CW2A and CW2B.

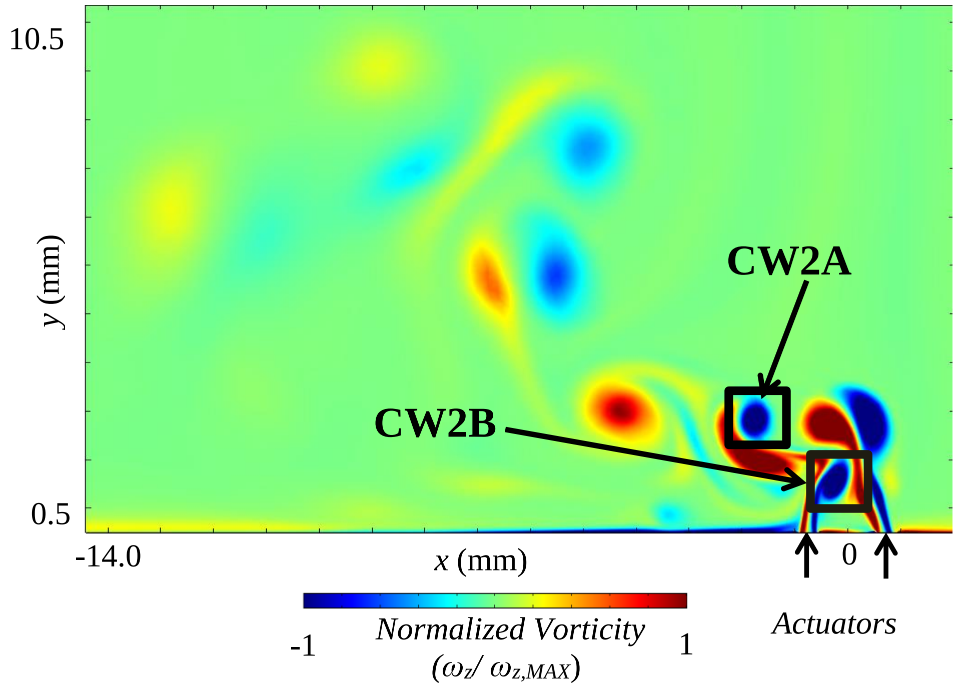

Figure 39 Vorticity contours for dual SJA operating in phase @ *t/T* = 78.51

At this point in time CW2A advects away from the orifice in the streamwise direction. CW2B advects opposite to the streamwise direction and ends up under CW1. As time progresses this leads to two counter rotating vortex pairs directly above orifice 2 (downstream orifice) as shown in Figure 40 below. The vortex splitting and realignment in this particular orientation happens within a time such that when the vortices are directly above orifice 2 it is close to the beginning of the ejection phase of actuation cycle. The induced velocity component from the initial vortices CCW1, CW1, CCW2 and the newly formed CW2B is now reinforcing the velocity of the fluid coming out of orifice 2.

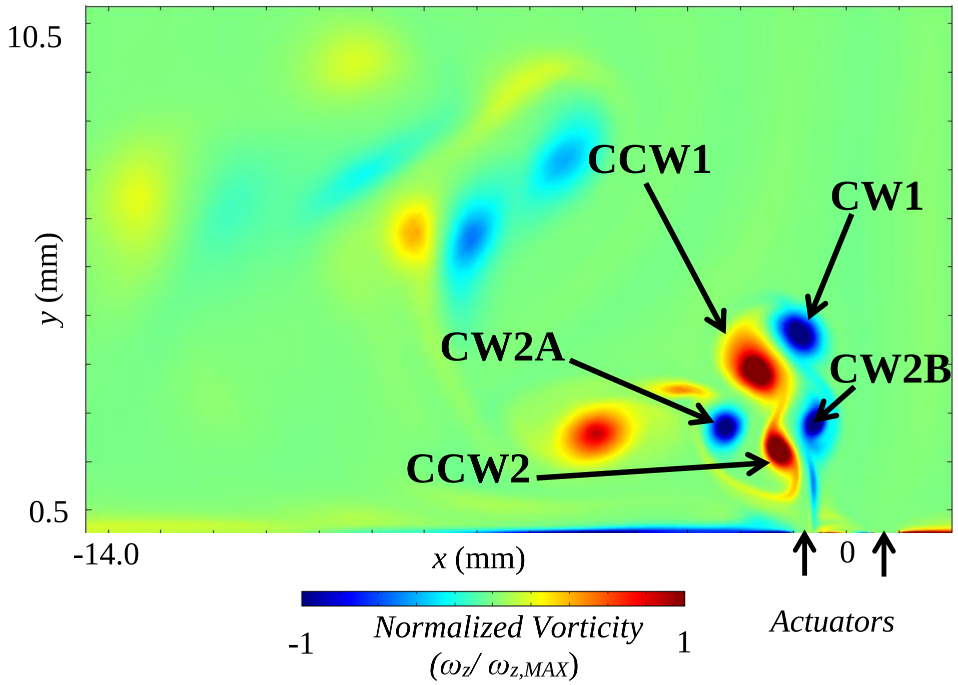

Figure 40 Vorticity contours for dual SJA operating in phase @ *t/T* = 78.95

This positive reinforcement of velocity at orifice 2 means that the impedance faced by the fluid trying to come out of the cavity is decreased. This could potentially allow for a higher than twice the momentum output of an individual actuator operating in similar condition. This phenomenon will be explored in greater detail in the quantitative modeling results section.

One of the important aspects of SJA interaction highlighted by this part of the study is the fact that the flow field is governed by the interaction of the vortices. Changing the temporal characteristics of the vorticity field changes the directional as well magnitude characteristics of the flow. This usually results in different time averaged flow features as shown will be shown in the quantitative analysis section. Shown in the sequence of figures below is the temporal progression of the vorticity field for set of actuators that are phased apart such that the upstream actuators leads by

30° (φ = 30°). The results presented are phase locked to the cycle of the downstream actuator (actuator 2). As the ejection phase for actuator 2 passes the halfway mark (Figure 41) we see the vortex pair associated with actuator 1 has already developed for and is about to begin separation from the cavity fluid. At this point both vortex pairs appear to be advecting away from the orifice in a direction normal to the cross-flow.

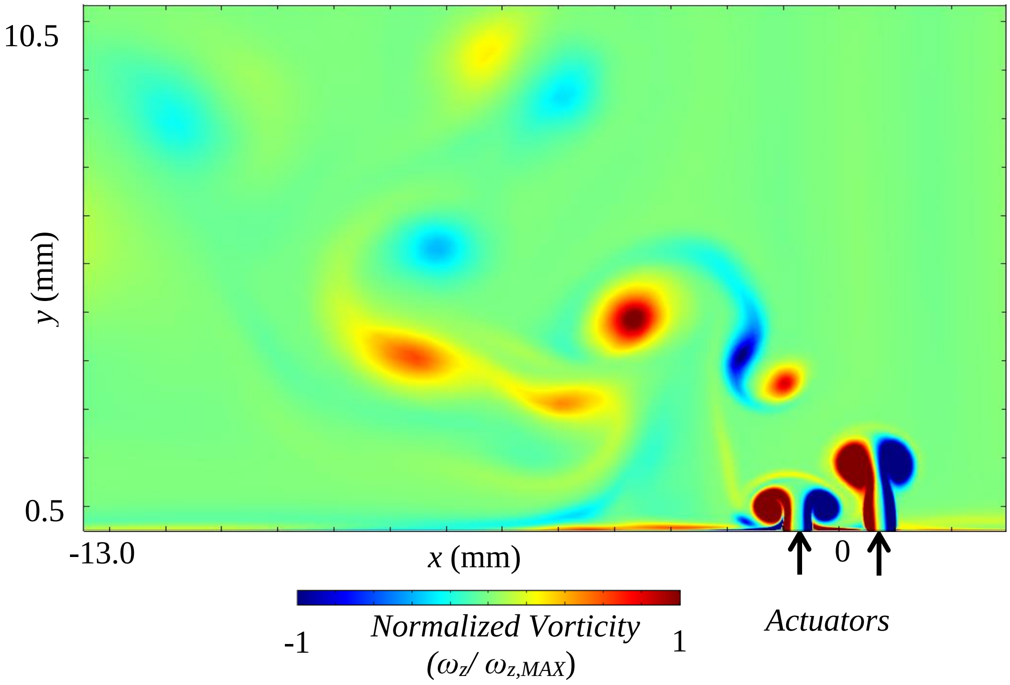

Figure 41 Vorticity contours for dual SJA operating at φ = 30° @ t/T = 78.28

Just as the ejection phase is about to end vortex pair from actuator 2 causes the pair from actuator 1 to stretch (Figure 42). As the process continues CW1 and CW2 (blue vortices) merge and pair with CCW1 resulting in a new pair and a single counterclockwise vortex (CCW2) as shown in Figure 43. The newly formed vortex pair begins to reverse its orientation and advect away from the orifice as the next cycle begins. The process then repeats itself (Figure 44).

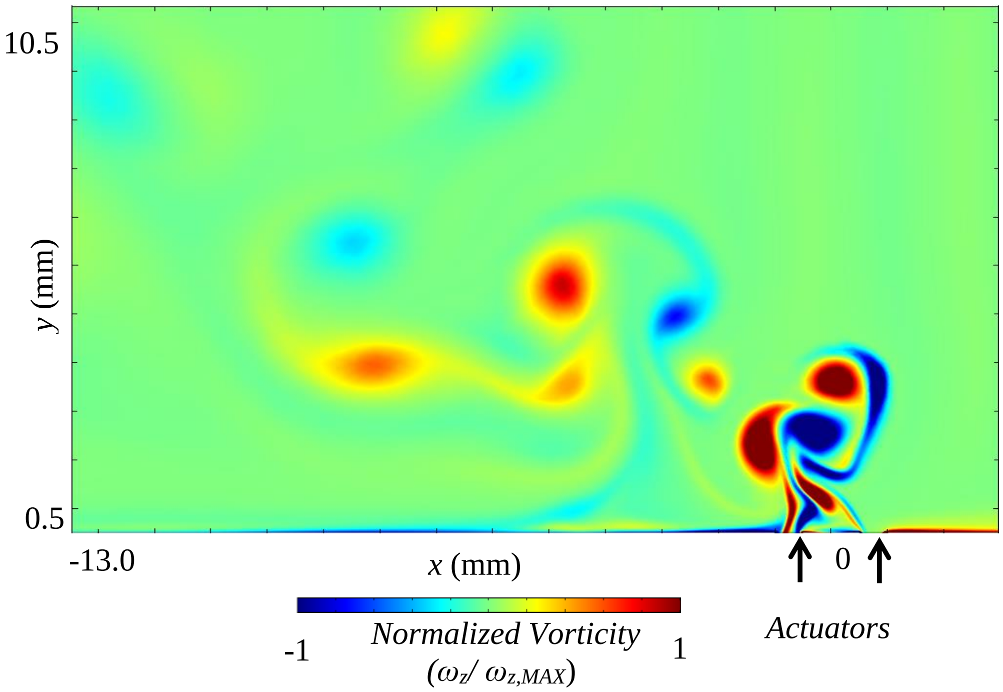

Figure 42 Vorticity contours for dual SJA operating at $\varphi = 30°$ @ $t/T = 78.45$

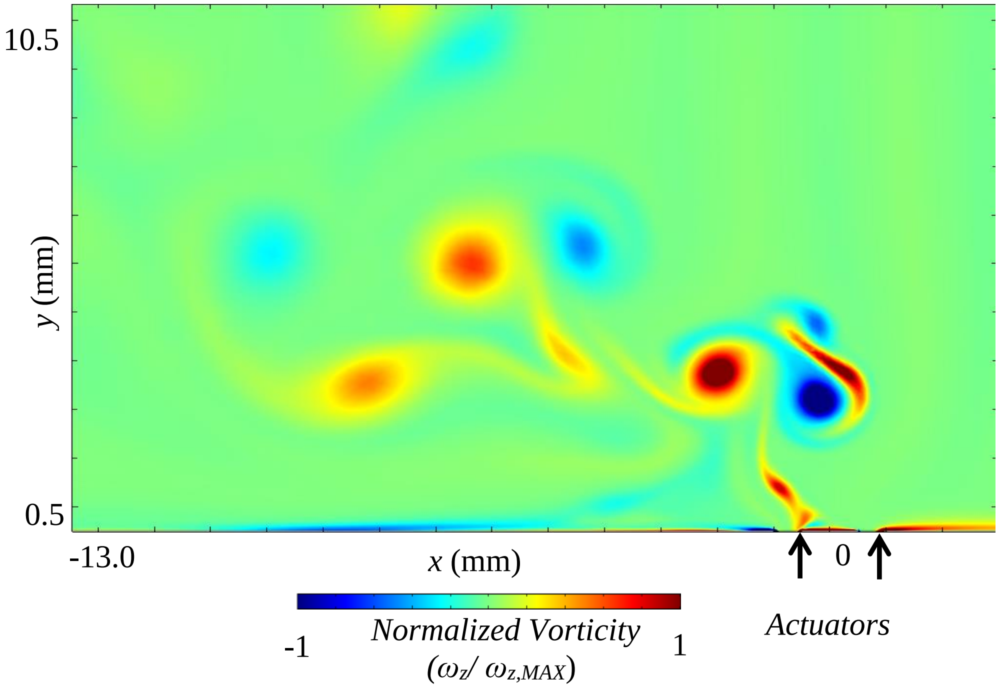

Figure 43 Vorticity contours for dual SJA operating at $\varphi = 30°$ @ $t/T = 78.89$

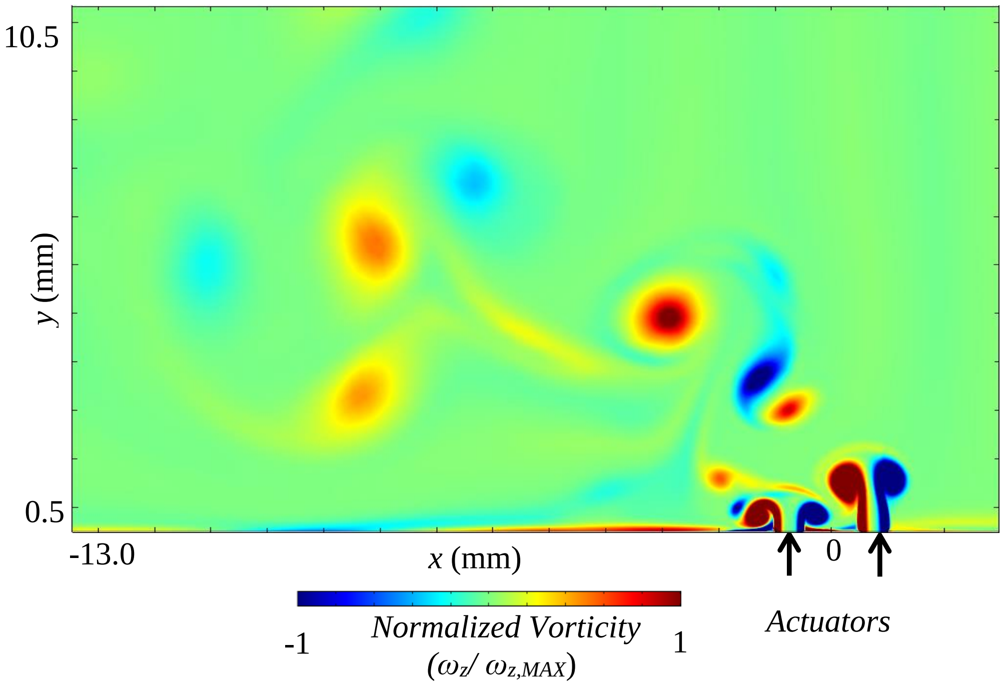

Figure 44 Vorticity contours for dual SJA operating at φ = 30° @ t/T = 79.22

2.3.2: Perturbation prediction of flow features

Modeling the actuator as a perturbation through the stream and vorticity formulation resulted in a solution that was very similar to the CFD solution with a significant computational cost advantage. Shown below are the results for the case of $\varphi = 30°$, $s = 2.5$ b and $R = 2.4$. The results shown in Figure 45 are for $t/T = 78.30$, which is similar to the time instant shown in Figure 42. A mesh identical to that used for the CFD calculations was utilized. Modeling the actuators as a perturbation on a surface instead of the full cavity resulted in results that were similar to CFD predictions close the orifice. The development and evolution of the two vortex pairs was very similar for the two techniques. However the results in the far field were not identical. The difference between the two techniques is discussed in the quantitative results section.

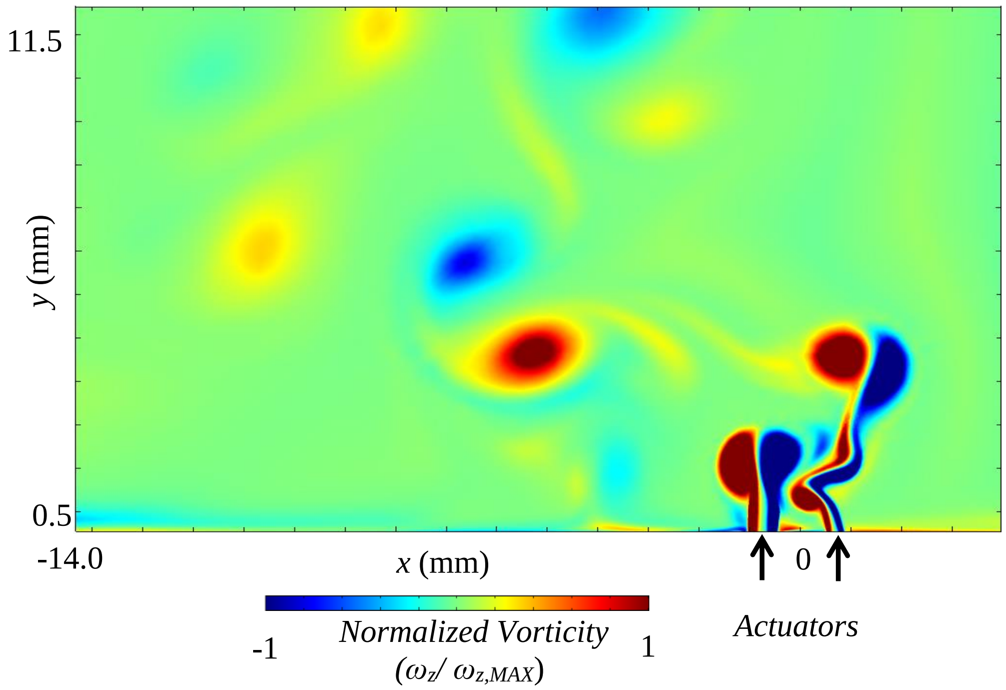

Figure 45 Vorticity contours as predicted through numerical perturbation method for dual SJA operating at φ = 30° @ t/T = 78.30

2.3.3: Analytical solution prediction of flow features

Since the analytical solution is a limited version of a linearized solution for periodic suction and blowing over a flat plate, it does not capture the flow features in the same detail as the numerical perturbation model and the full 2D unsteady turbulent CFD. It is therefore not suited for studying and understanding the physics of the interaction through flow features. The analytical solution assumes that actuation results in a perturbation linearly imposed on a cross-stream flow. The magnitude of the perturbation decays in time and varies in space in way that is specified by the boundary conditions. The only effect of actuation is therefore a harmonic oscillation in local velocity components. While this makes the analytical solution unsuitable for prediction of flow features, the time averaged characteristics of the flow field that are predicted by this method do agree with experimental results as will be shown subsequently. Shown in Figure 46 is a quiver plot of the velocity vectors close to the orifice.

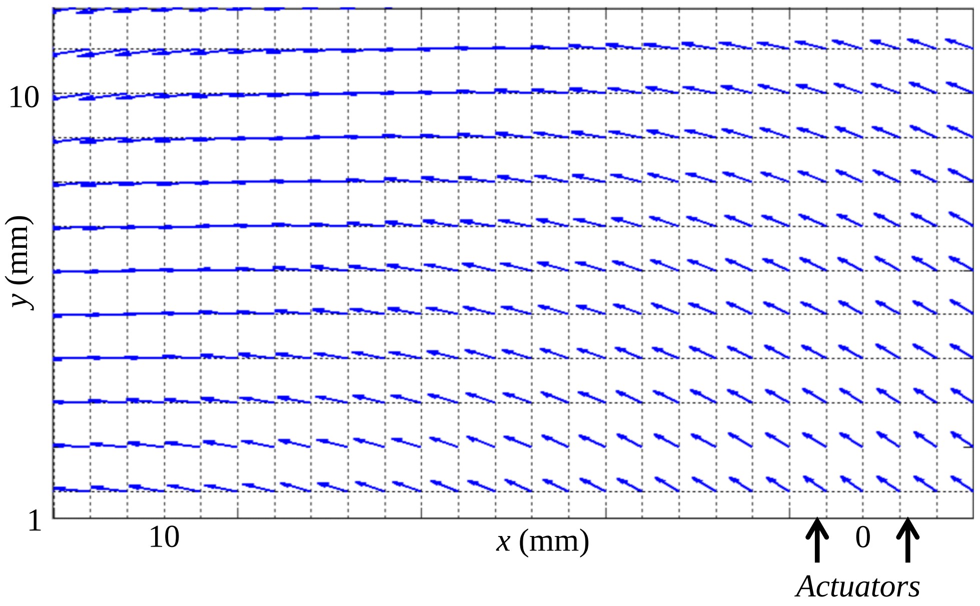

Figure 46 Velocity contours as predicted by analytical solution to perturbation method for dual SJA operating at φ = 30° @ t/T = 78.30

2.3.4: Summary of qualitative analysis of modeling results

The three modeling techniques were used to compute the flow field and there results were analyzed in a qualitative sense. The 2D unsteady CFD method adequately resolved the vortex pairs emanating from both orifice. For a single actuator the CFD was also able to reproduce the vortex pair switching phenomenon observed by Li and Sahni (Li & Sahni, 2014). For the case of two actuators vortex pair switching and splitting was observed which for a phase angle of φ = 0° resulted in enforcing the exit velocity at the second orifice. The numerical perturbation method also was successfully able to reproduce the vortex pair, and in the immediate vicinity of the orifice produced results similar to the 2D CFD. Although phenomenon such as vortex switching and splitting was also observed using this method, the results varied from those predicted by the CFD. The analytical solution to the perturbation method was unable to reproduce any of the flow features that would be useful to study and understand the interaction. A quantitative analysis of the results in presented in the following section.

2.4 Quantitative analysis of modeling results

2.4.1: Quantifying the magnitude, direction and decay rate

In order to compare the flow field results of two different sets of parameters a new coordinate system along the jet centerline axis was used. This was done to reduce the flow field to a single quantity or curve or that could be compared easily from one set of parameters to another. Three performance metrics were selected to quantify the control authority of the jets. These were based upon the quantities analyzed by the studies referenced in sections 1.4 and 1.5. The first measure of control authority deals with the absolute magnitude of the momentum being added to the flow. The standard quantity used to measure this is the momentum coefficient, C_μ. The momentum coefficient is usually calculated through knowledge of the spatial and temporal distribution of the velocity along the orifice during the exit phase of the cycle. While this information can be obtained from modeling results, it is difficult to obtain experimentally. Since the model results needed to be validated through the experiments, a different approach to calculating the velocity was employed. The coordinate system along the centerline axis is shown below in Figure 47.

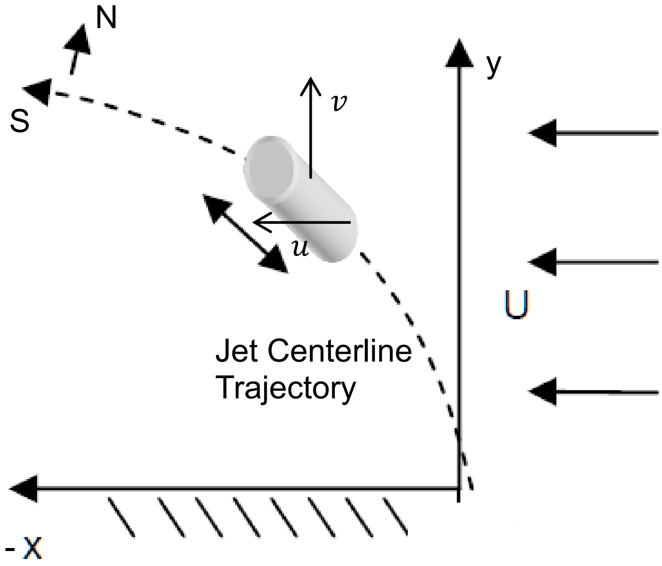

Figure 47 Depiction of jet centerline trajectory and reference coordinate system

The jet centerline trajectory is defined as the locus of points of maximum velocity inside the plume. Along the centerline trajectory we define our *NS*-coordinate system such that the *S*-coordinate lay along the centerline trajectory and *N*-coordinate represents the direction normal to it. The trajectory is constructed using the time averaged flow field information. The centerline trajectory is therefore the locus of points of maximum time averaged velocity. This is necessary for validating the model through experimental data which cannot be accurately time resolved close to the orifice. For dual actuators that are closely spaced the plumes merge and result in single jet, therefore a centerline trajectory can be identified. Within the trajectory the time resolved velocity amplitude is largest closer to the orifice and decays while moving away from it. However the magnitude of the time averaged velocity vectors behaves differently as shown by Figure 48 (experimental results shown to illustrate measured decay). The velocity magnitude appears to increase from a small value and reaches its peak close to, but not at the orifice. It then decays to a steady value of velocity associated with the cross-flow. The magnitude of the time average velocity vectors along the centerline is referred to as V_{CL}, with $V_{CL,Max}$ being the maximum value in the plume. Very close to the orifice ($S < 4b$) the velocity magnitude is large, however the time average of the vectors is small (suction and blowing are more symmetric). This means that the magnitude of the time averaged velocity vectors is not the same as the time average of the magnitude of the same velocity vectors. For purposes of error reduction in the experimental data, the former quantity will be used to characterize the plume behavior for this study.

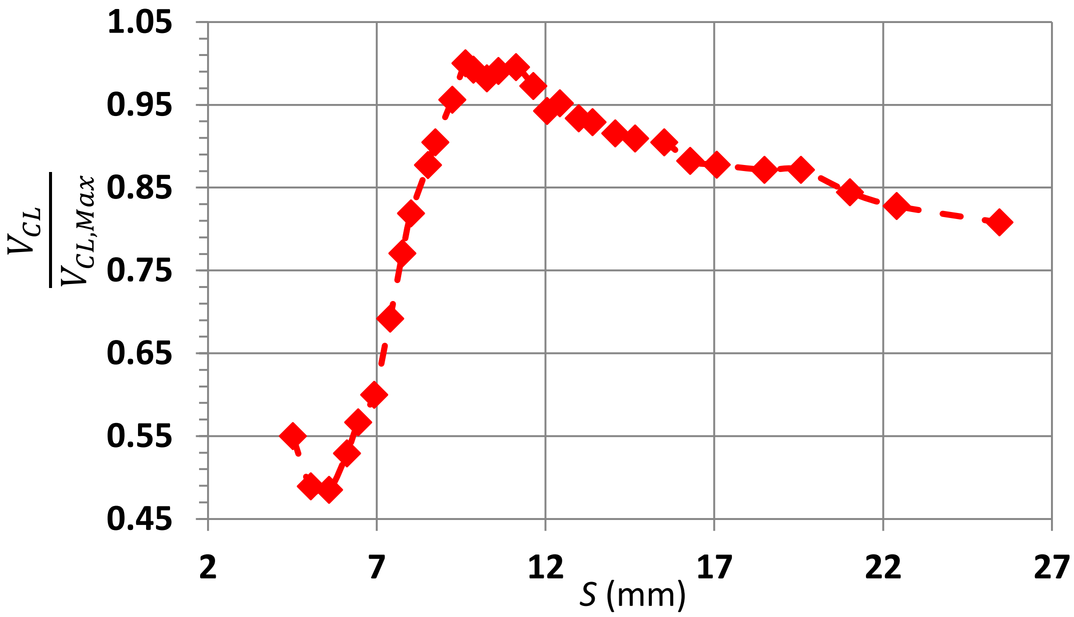

Figure 48 PIV measured Decay of velocity along centerline trajectory for *R* = 2.4, *φ* = -120° and *s* = 2.5*b*

The path length along the *S* axis at which the velocity peaks is a function of the parameters *φ*, *s* and *R*. It is also related to the amplitude of the velocity at the orifice. Since this value can be calculated more accurately than the time average expulsion velocity at the orifice, this value is used to calculate the momentum coefficient for this study. Going back to the definition of momentum coefficient from Equation 4 we now have the expression that we use to calculate the momentum coefficient for this study.

$$C_\mu = \frac{\rho {V_{CL,Max}}^2 b}{\rho U^2 c}$$

Equation 27

The exact algorithm used to compute the centerline and the maximum value along the centerline is detailed in the Appendix. The actuator length scaling used to compute the momentum coefficient for the case of two actuators is 2b. The factor of ½ in the denominator of Equation 4, therefore disappears.

While the momentum coefficient is a measure that allows us to compare the magnitude of momentum coming out of the jets it does not provide us information about the direction. The direction of the flow of momentum is important in determining what the distribution of the blockage effect of the jet is. The blockage effect is directly responsible for displacing the streamlines and hence virtual shaping. Therefore for the purpose of this study it is desirable to obtain and compare a path along which the momentum travels. One way to characterize this path is through the use of the jet centerline trajectory as was done by Ugrina (Ugrina, 2007). While it does not provide a measure of exactly how the streamlines are displaced it can be used to compare cases of different parameters to obtain a general idea of the direction of the displacement.

In addition to the peak magnitude and the direction of the flow of momentum, it is also desirable to evaluate how quickly the velocity inside the plume decays (either through diffusion, or through pressure gradient). This provides an estimate of the impedance that the jet faces as it emerges and travels in the cross-flow. This could be important for an application that does not require directional control over the plume, but seeks to maximize the jet output.

The interaction of the array is now characterized for the entire parameter space using the three models and above mentioned performance metrics. The remainder of this chapter deals with some of the important observations of the parameter space study.

2.4.2: Quantitative analysis of the effects of Velocity Ratio (*R*)

The velocity ratio at which the jet operates determines ability of the jet to penetrate the cross-flow. Typically for higher velocity ratios the jet is able to retain its *y*-velocity component for longer. The effect of the velocity ratio on the array momentum coefficient is coupled to the phasing therefore will be studied in Section 2.4.4. The directional effects predicted by each model for two different velocity ratios, *R* = 2.4 and *R* = 0.95 are presented in Figure 49 and Figure 50 below.

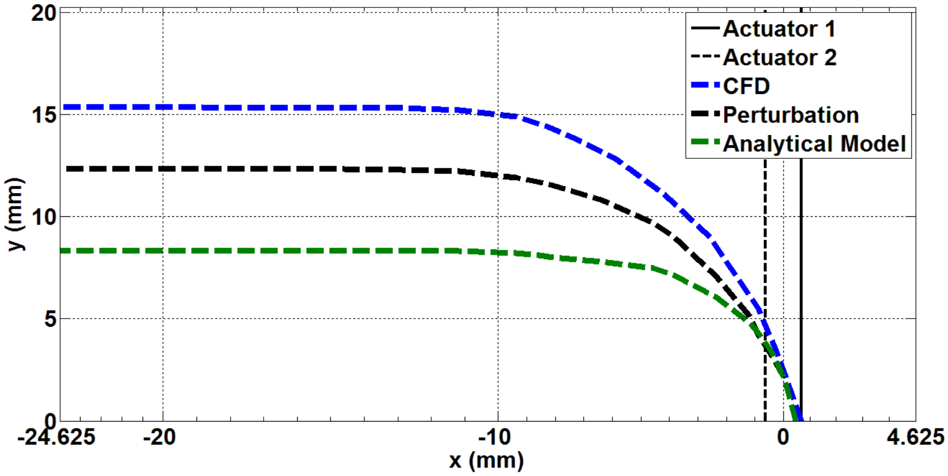

Figure 49 Modeling predictions for jet centerline trajectory for *R* = 2.4, *s* = 2.5*b* and *φ* = 0°

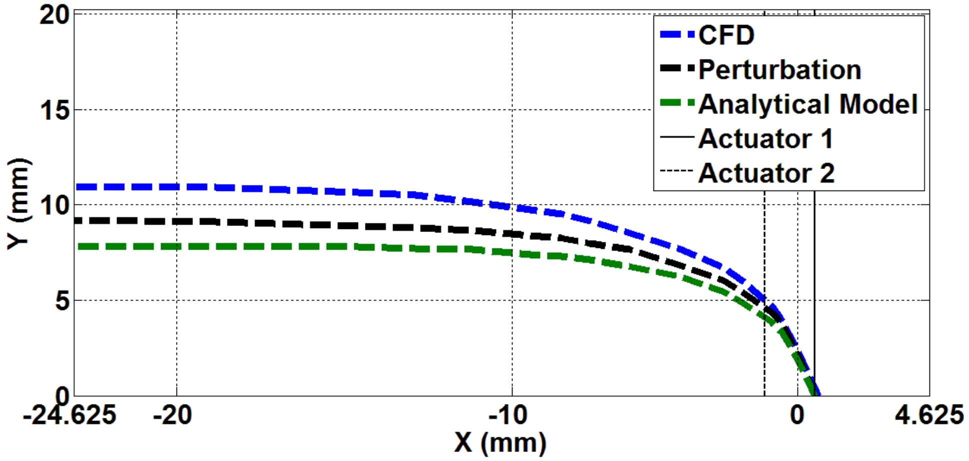

Figure 50 Modeling predictions for jet centerline trajectory for *R* = 0.95, *s* = 2.5b and *φ* = 0°

For a velocity ratio of $R = 2.4$, all three models predictions are within 10% of one another for a height of less than $10b$ above the orifice after which they begin to diverge. The full CFD model predicts a higher deflection resistance in comparison to both the perturbation and analytical solutions. All of the models suggest that the jet is completely horizontal at some downstream distance. According to the full CFD and perturbation model this distance is around 12 mm downstream of the actuators. The analytical solution suggests that this happens sooner (around 8 mm). For a velocity ratio of $R = 0.95$, the results from the three models are diverge less but they start diverging earlier. Figure 50 shows that the predications begin to diverge at a height of about 3 mm above the orifice. Figure 51 shows the comparison between the CFD predicted results for both velocity ratios. The CFD was chosen for the comparison due to the higher accuracy of this modeling method compared to the others (this will be established in the validation section). The results indicate that the penetration power of the jet is proportional to R. An interesting observation from Figure 51 is that for the lower velocity ratio case the CFD results seem to indicate that vertical velocity component seems to die out slower that it does for the higher velocity ratio case.

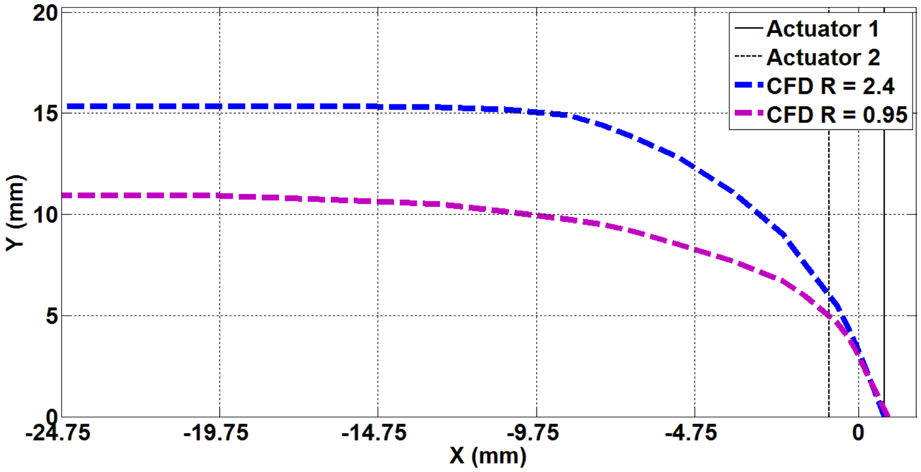

Figure 51 CFD predictions for jet centerline trajectory for *R* = 0.95 & 2.4, *s* = 2.5*b* and *φ* = 0°

In addition to the path of the centerline trajectory of the jet we also observe how the magnitude within it changes as a function of velocity ratio. The results for the velocity decay are shown below in Figure 52.

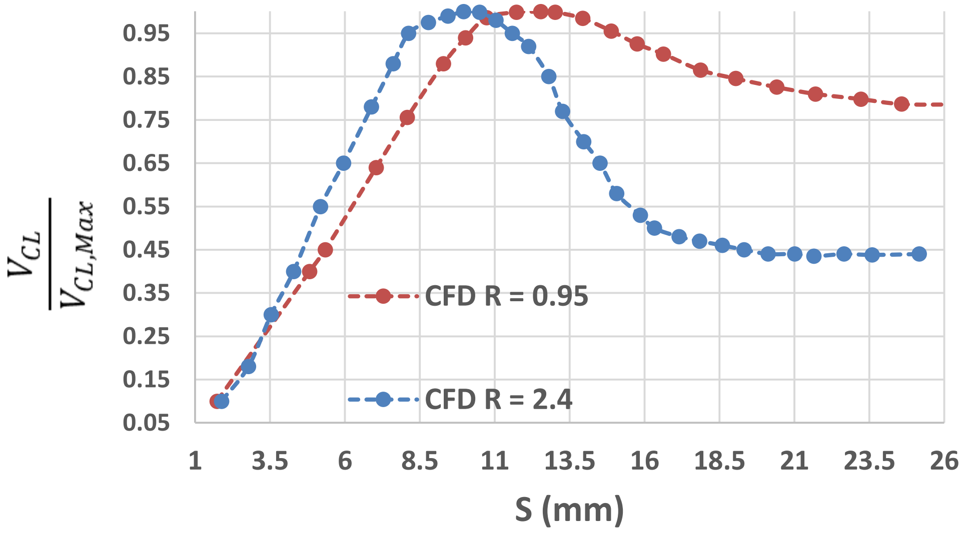

Figure 52 CFD predictions of normalized velocity decay for *R* = 0.95 & 2.4, *s* = 2.5*b* and *φ* = 0°

The results indicate that for R = 2.4 the jet reaches its peak magnitude closer to orifice and the velocity appears to decay faster close to the orifice in comparison to the R = 0.95 case. This indicates that there is a region of a higher close to the orifice for the higher velocity ratio whereas the momentum is more evenly distributed along the centerline.

2.4.3: Quantitative analysis of the effects of Spacing (*s*)

The jet centerline trajectory for cases of s = 2.5b and s = 4.5b are shown in Figure 53. The effect of increasing the spacing between the jets is similar to that of decreasing the velocity ratio. The jet deflection increases as the actuators are spaced apart. The amount by which the jet is deflected is smaller in comparison to what was observed when the velocity ratio was changed.

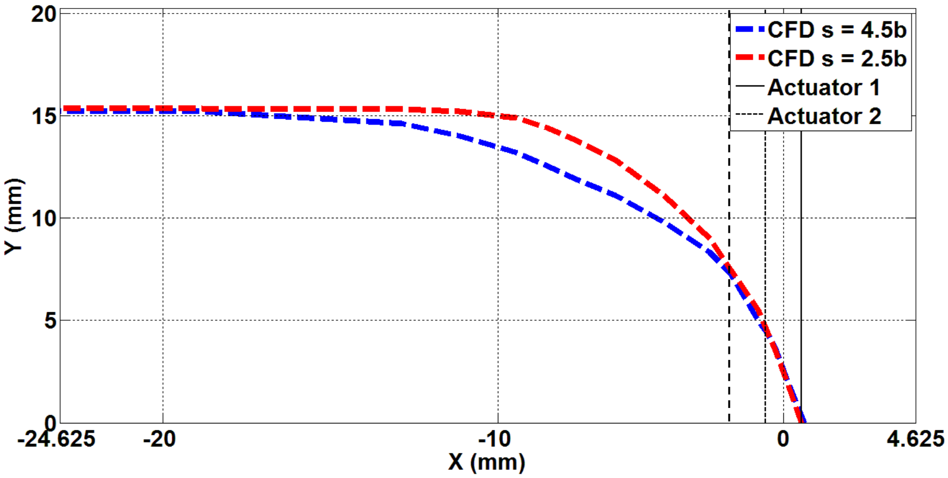

Figure 53 CFD predictions for jet centerline trajectory for R = 2.4, s = 2.5b and 4.5b, φ = 0°

The velocity decay is shown in Figure 54. The decay pattern is similar to that observed for altering the velocity ratio. Spacing the actuators apart results in the peak velocity value being located further along the centerline. In addition to that rate of change of velocity along the *S*-coordinate is different. The velocity increases and decreases slower resulting in a broader peak. The results for *s* = 2.5 b show that the jet decays to near cross-flow values at about *S* = 20 mm. The *s* = 4.5b case still appears to be decaying at around *S* = 26 mm.

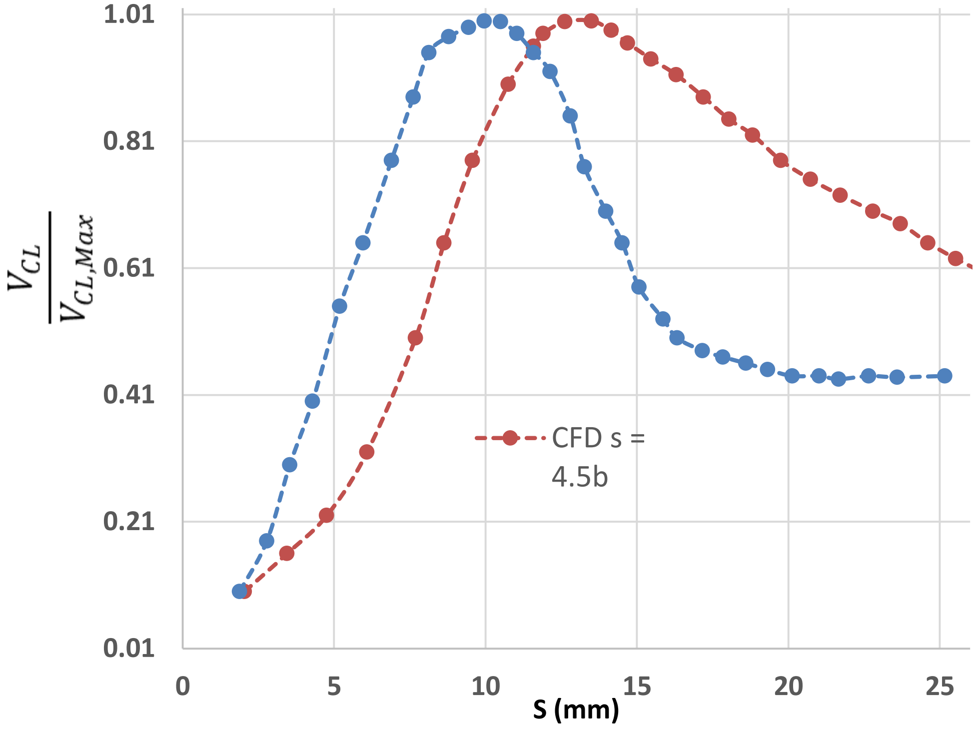

Figure 54 CFD predictions of normalized velocity decay for *R* = 2.4, *s* = 2.5*b* and 4.5*b*, *φ* = 0°

2.4.4: Quantitative analysis of the effects of Phasing (φ)

The effects of phasing are studied in this section with emphasis on direction, decay as well magnitude. The selected performance metrics displayed the highest sensitivity to this particular parameter. The results of section 2.3.1 suggested that altering the phase could potentially altered the total momentum being imparted by the jets. In order to see whether or not that is the case the momentum coefficient as predicted by the CFD and numerical perturbation solution are shown below. The results for the analytical solution are not included here. This is because of the way the boundary condition was formulated for the analytical solution. The actuation is modeled as a time periodic spatially distributed velocity. The amplitude and distribution of this velocity are fixed, and while the jet plume velocity does change in response to a change in parameters the variation was not significant. The jet plume velocities as predicted by the CFD and numerical perturbation solution are dependent on the impedance the flow faces as it exits the nozzle. This impedance is a function of the spacing, velocity ratio and phase and therefore the momentum coefficient changes in response to change in any of these parameters.

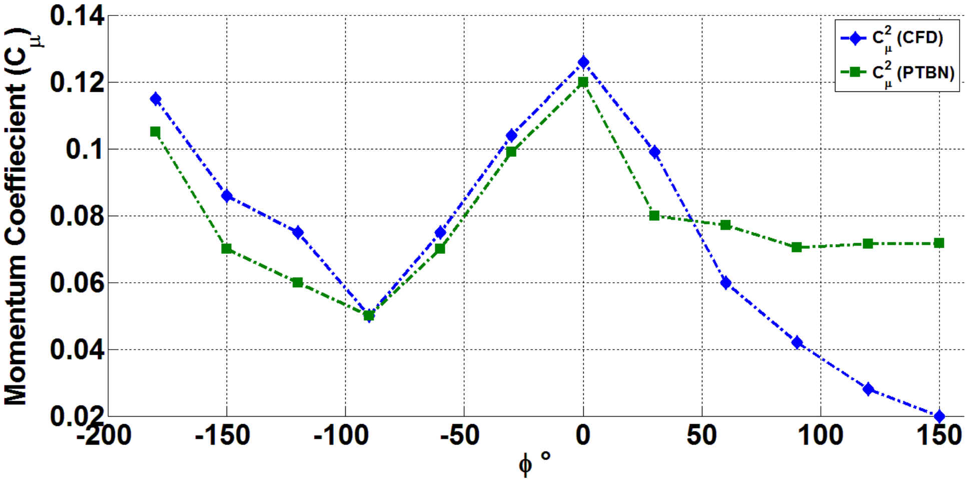

Figure 55 CFD and Perturbation predictions of momentum coefficient for R = 2.4, $s = 2.5b$ and $\varphi = 0°$

The results indicate that for this specific velocity ratio and spacing the momentum coefficient can range from a low of 0.02 to a high of approximately 0.12 (according the CFD predictions). The 2D CFD and the perturbation method predict a similar trend for the momentum coefficient for phase ranging from -180° to 0°. After which the trend diverges significantly. Both models show that there is an approximate inverse linear dependence of momentum coefficient on the phase angle for -180° < φ < -90°. Past this point the momentum coefficient begins to increase linearly from -90° to 0°. After this point the CFD model predicts a steady drop whereas the perturbation method predicts that the momentum coefficient levels out. These results will be revisited and studied in more detail in the validation section. The results for the jet centerline trajectory as predicted by the three models is presented in the sequence below. The points along the centerline trajectories were identified using the algorithm discussed in Section 2.4.1. Once the points were obtained a curve was fit to them using the MATLAB curve fitting tool and spline interpolation.

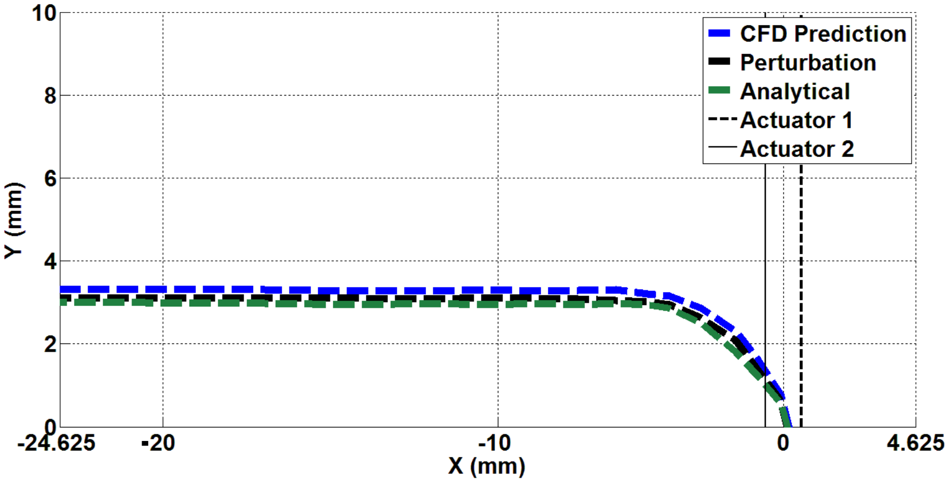

Figure 56 Modeling predictions for jet centerline trajectory for R = 2.4, s = 2.5b and φ = -180°

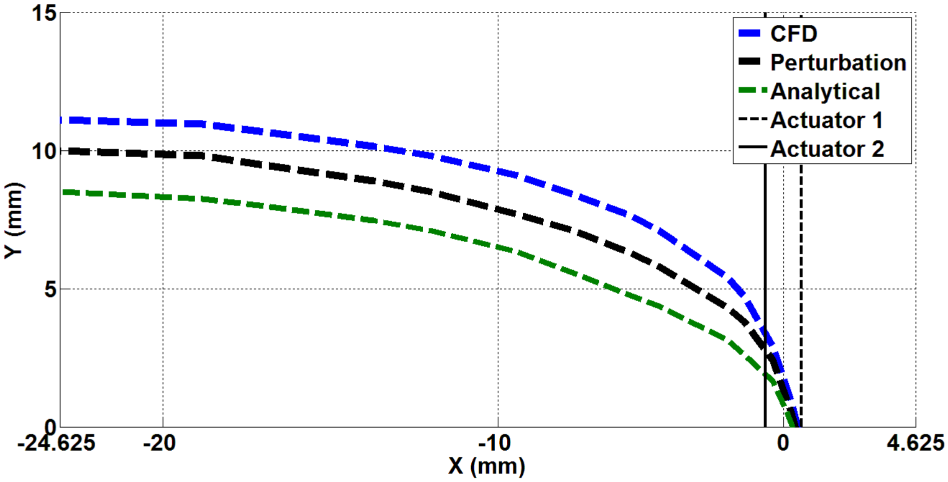

Figure 57 Modeling predictions for jet centerline trajectory for *R* = 2.4, *s* = 2.5*b* and *φ* = -120°

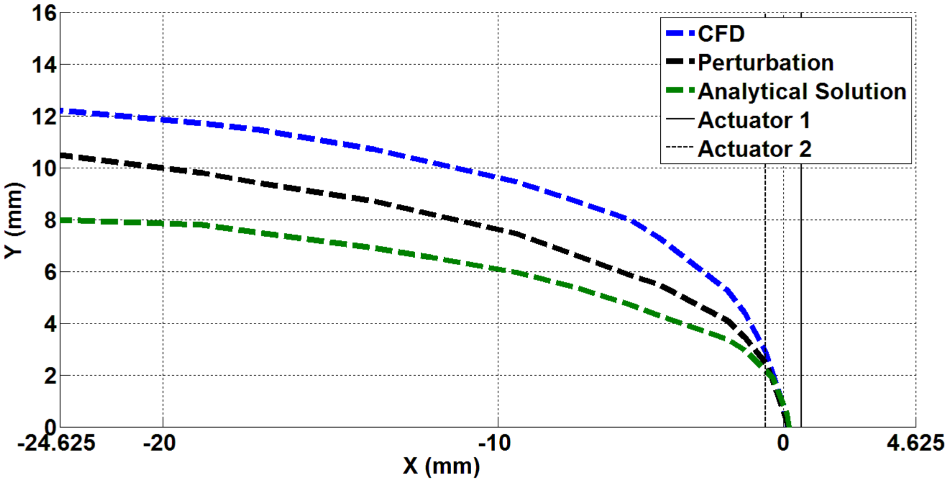

Figure 58 Modeling predictions for jet centerline trajectory for *R* = 2.4, *s* = 2.5*b* and *φ* = -60°

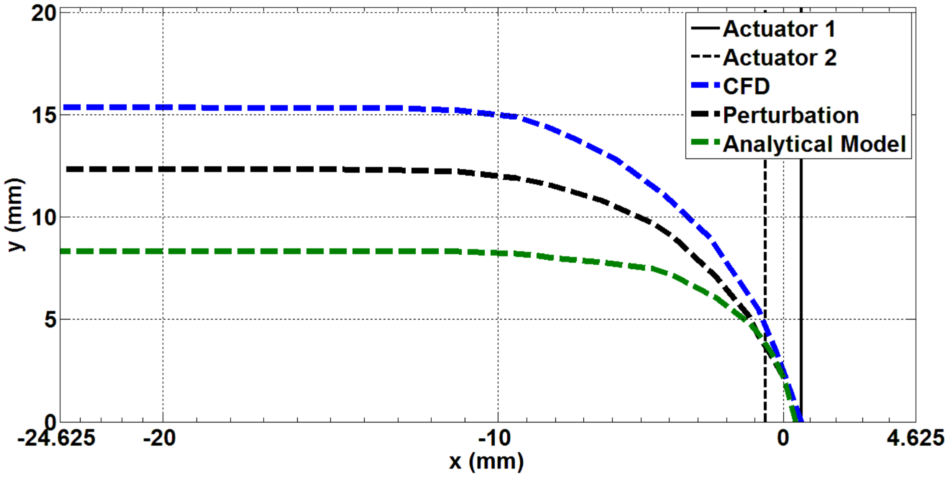

Figure 59 Modeling predictions for jet centerline trajectory for *R* = 2.4, *s* = 2.5*b* and *φ* = 0°

The three models predict similar behavior for case of *φ* = 180° as shown in Figure 56. All three trajectories deflect immediately and settle around a maximum height of 3.75 mm. As the phase angle increases the trajectories for the three prediction begin to diverge from one another, with the CFD always predicting a smaller deflection, followed by the perturbation model and the analytical solution for which the highest deflection was observed. All three models predict a trajectory that is vectoring into the cross-flow up until a phase of -60° (Figure 57 and Figure 58). As the phase increases past this value the jet still appears to vector into the cross-flow however the jet appears to lose its vertical velocity and flatten around a downstream distance of *x* = 10 mm. This could be due to the increased force the jet experiences as it tries to vector into the cross-flow. This behavior is seen for all cases at and past 0° (Figure 59 and Figure 60).

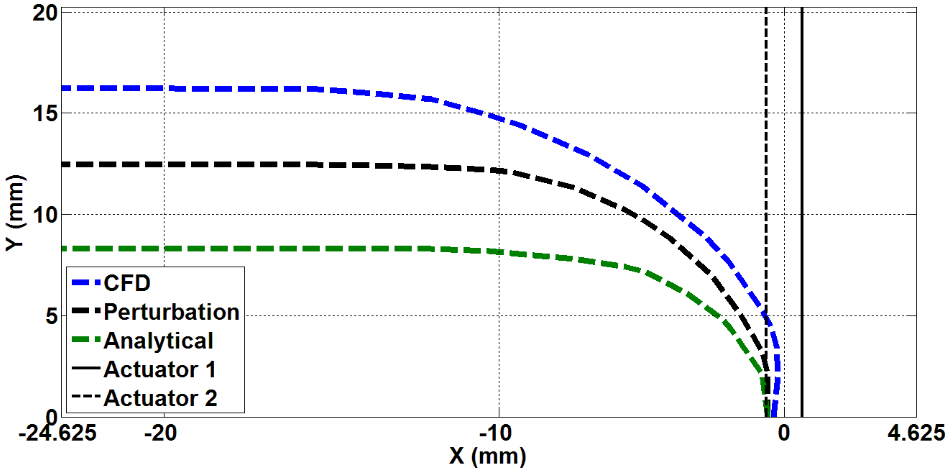

Figure 60 Modeling predictions for jet centerline trajectory for *R* = 2.4, *s* = 2.5*b* and *φ* = 60°

In addition to this we observe that trajectories predicted by all three models for *φ* = 0° and *φ* = 60°, vary close to orifice but flatten at similar locations. The analytical results for the two phase angles to do not vary by much, except for close to the orifice.This observation will be discussed in more detail in the validation section. In addition to the trajectories the decay rates for two phase angles are also compared. The velocity behaves similar for the growth part of the curve. Both jets attain peak velocity around 10 mm away from the orifice. However the decay rates beyond that point differ. The -120° case has a response similar to that of increased spacing or decreased velocity ratio. The decay is spread over a larger distance. The reason for this behavior has to do with the fact that the jet is vectored in the direction of the cross-flow. It therefore develops along a favorable pressure gradient as opposed the 0° case. Vectoring into the cross-flow results in a sharper drop after the velocity peaks. This is also the reason why a jet that is vectored into the cross-flow "flattens out" or deflects closer to the orifice as was seen in Figure 59 and Figure 60.

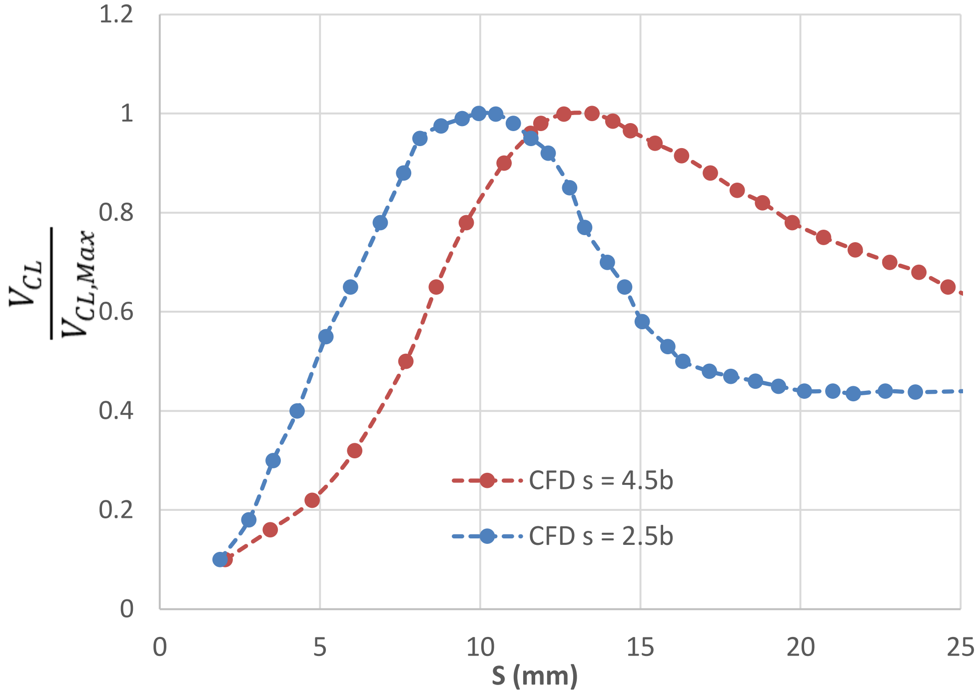

Figure 61 CFD predictions of normalized velocity decay for *R* = 2.4, *s* = 2.5*b*, *φ* = -120° and 0°

2.5 Summary of modeling

The behavior of an array of two interacting synthetic jet actuators in the presence of a cross-flow was simulated. Three modeling methods were used. The first method involved a numerical solution of the 2D unsteady Navier-Stokes equations through a commercial flow solver. Two complete actuators (cavity and orifice nozzle) were simulated. The second method involved a numerical solution to the stream and vorticity formulation of the Navier-Stokes equations. Instead of modeling the complete actuator, the effect of actuation was modeled as a sinusoidal perturbation applied at the bottom of a nozzle. A third method involving a linearized solution to the stream-vorticity equations was utilized. The actuators were modeled as perturbation boundary conditions. The effect of the actuators was spatially and temporally decaying perturbation flow superimposed on to a cross-flow. The models were used to study the physics of the interaction of an array of two synthetic jets with a cross-flow quantitatively. Three velocity and momentum based performance metrics were defined to compare the results of the models. These metrics were used to study the effect of phasing, spacing and velocity ratio on the flow field.

Chapter 3: Design, Build and Characterization of a Synthetic Jet Actuator

3.1 Developing SJA for model validation

3.1.1: Design criteria

In order to validate the model a synthetic jet actuator that could satisfy the modeling constraints had to be developed. Since the models were all 2D the first and most significant requirement was that the actuators must produce a flow that is 2D, or 2D in some region of the flow. Based on the information obtained from previous studies (detailed in chapter 1), this requirement could be satisfied by a high aspect ratio finite span synthetic jet actuator. A very small orifice width b (less than 1 mm) would result in a high aspect ratio (> 20) for any actuator of length l greater than 20 mm, however the region of which the flow is 2D is very small for this aspect ratio. Based on the size of the vortices observed in the modeling section a 2D region of at least 20 mm above the orifice was desired, this meant that the aspect ratio had to be higher (above 50). The actuators also had to be small enough to satisfy the spacing constraint as well. This meant that two orifices had to be able to come to within 2.5 orifice widths of each other. In addition to this the actuators had to meet the velocity ratio requirement, which required a velocity output that could lead to the desired R values of 2 and above.

3.1.2 Synthetic Jet Actuator design

Based on the requirements prescribed in the section above, a pre-existing asymmetric actuator design first developed by NASA (Rumsey, 2004) was selected for modification. Their design was modified in two major ways. The first modification was based upon the size of the available driver. The piezo-ceramic brass disc used by NASA was 50 mm in diameter. This dimension was the design constraint for the cavity diameter. The commercially available low cost piezo-ceramic brass disc used for the SJAs in this study was 41 mm in diameter. The diameter of the cavity was therefore constrained by this dimension. 3D unsteady laminar CFD was used to optimize the nozzle aspect ratio and cavity depth through a parametric sweep. The constrained parameters were the depth of the cavity, the aspect ratio and cavity wall thickness (to satisfy spacing constraint). The external dimensions of the final design are shown in Figure 62. The internal dimensions are shown in Figure 63. The overall assembly is shown in Figure 64.

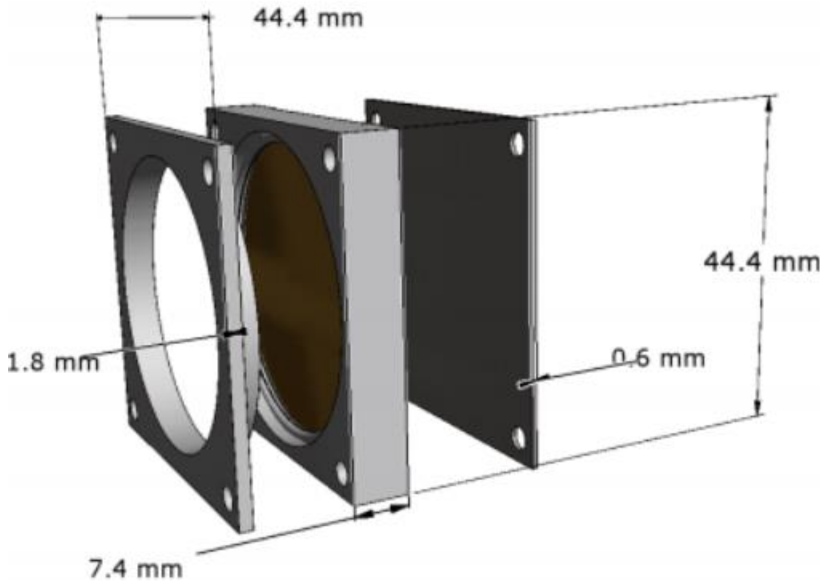

Figure 62 External dimensions of the synthetic jet actuator

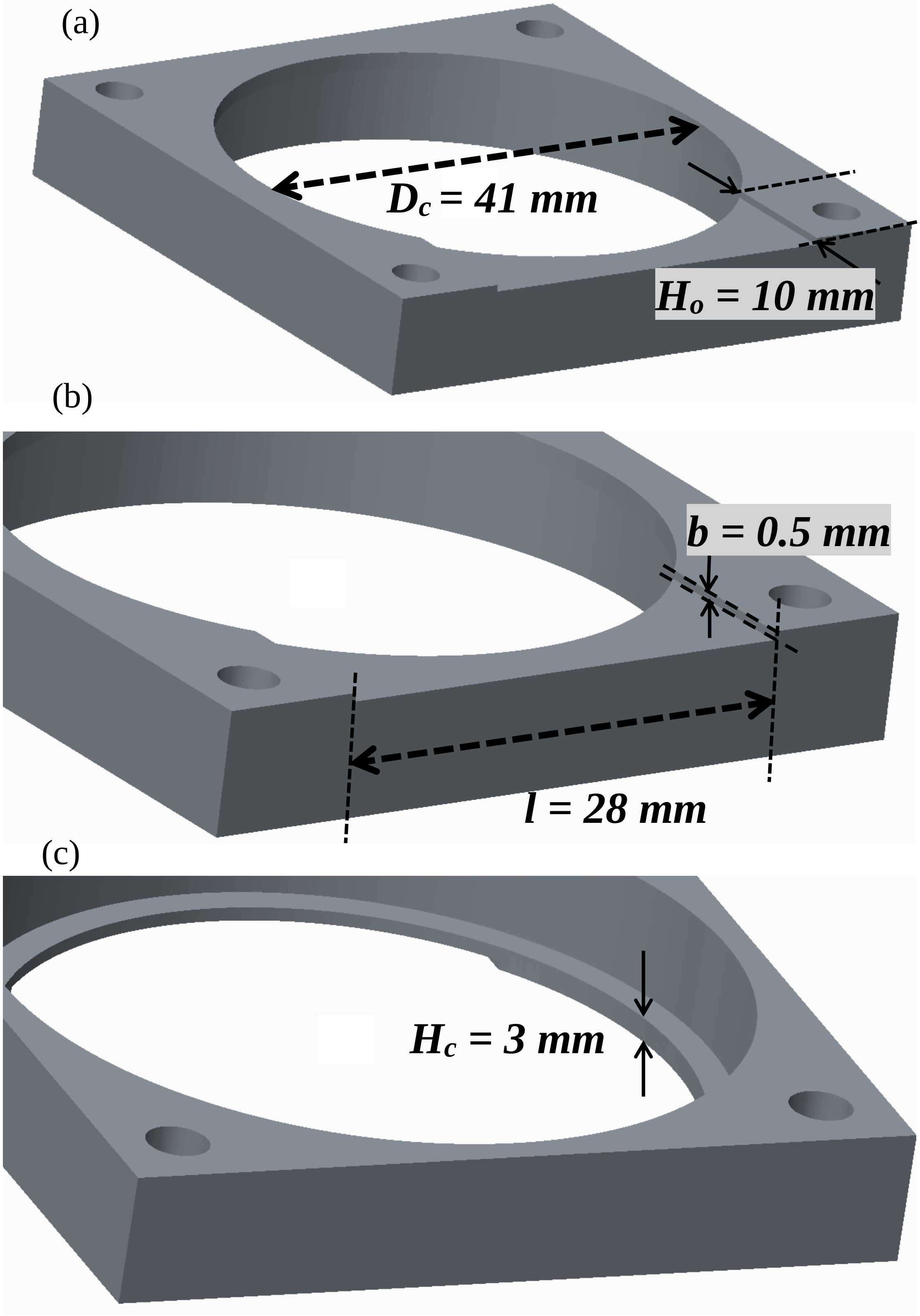

Figure 63 Internal dimension of synthetic jet actuator

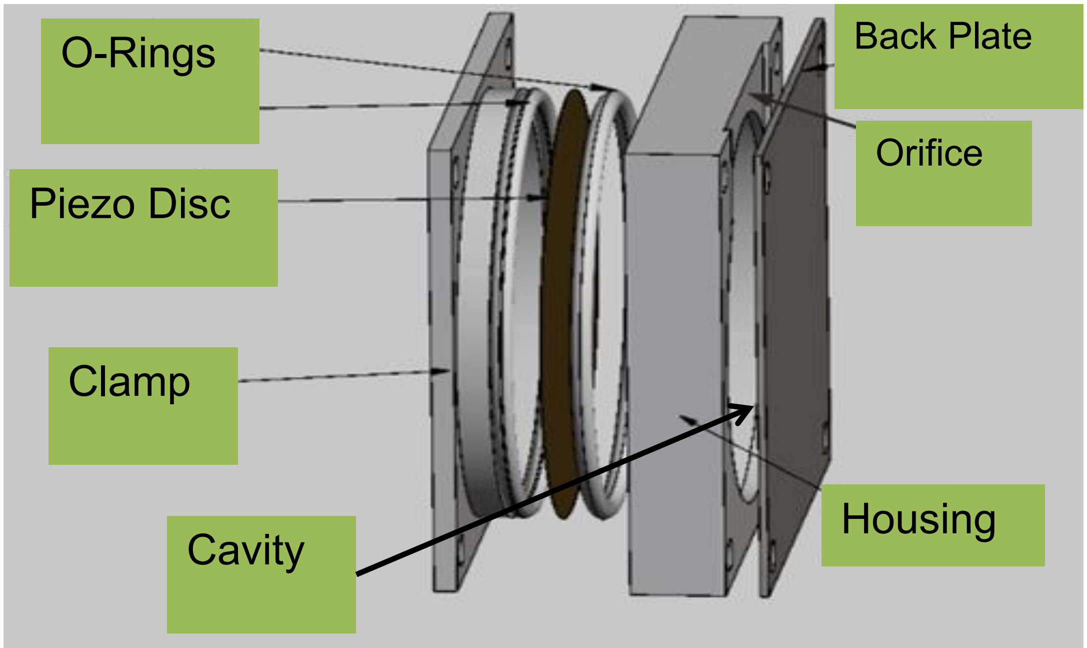

Figure 64 Synthetic jet actuator assembly

The piezo-ceramic brass disc used as the driver was manufactured by Murata electronics, part number 7BB-41-2C, and is shown in Figure 65. It consisted of a piezo ceramic element bonded to a brass disc. The diameter of the element was 26 mm. The diameter of the brass disc was 41 mm. The thickness of the brass disc was 0.40 mm whereas that of the piezo element was 0.63 mm. This particular driver was chosen due to its low cost and extended life cycle. The driver is commonly used in audible alarms and can be driven for extended periods of time at voltages in excess of 100 V. The resonance frequency of the disc under free conditions is around 2200 Hz. At resonance the electrical impedance of the disc is 250 Ω for free conditions. Typical current draw for the required operating conditions was in the range of 0.25-0.5 A. The power drawn by the actuators when operating under these conditions was in the range of the 20W-30W.

The disc was installed with the piezo facing the opposite direction of the cavity. The disc was inserted between two Teflon O-rings to provide a pinned boundary condition as opposed to a clamped one. This allowed for greater deflection towards the circumference and therefore higher velocities. A 0.6 mm thick steel plate was used to seal the other end of the cavity. A thin layer of silicone vacuum grease was applied to ensure a proper seal on both ends of the cavity. The assembly was held together using 4 nuts and screws, one at each corner of the assembly. The screws were then torqued to a value of 0.35 N-m. This value was determined by observing the velocity response to the changing the torque from 0.1N-m to 0.5 N-m in increments of 0.05 N-m. The results indicated a peak at 0.35 N-m.

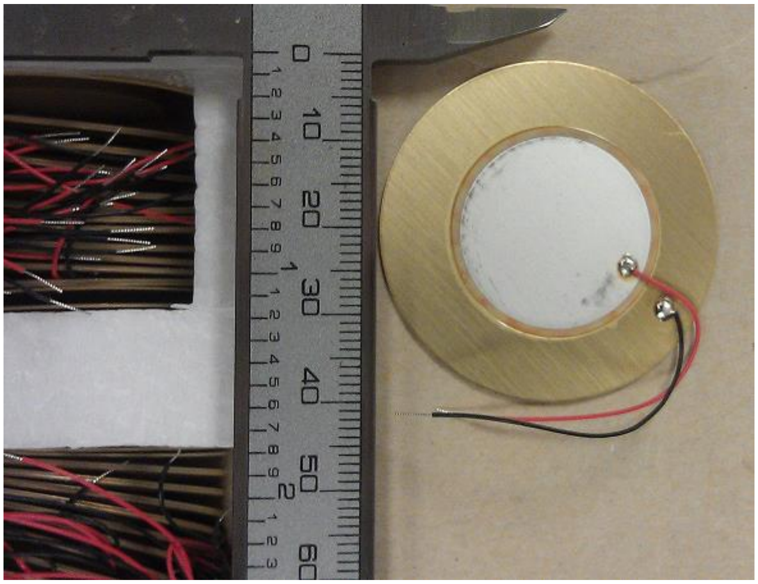

Figure 65 Piezo ceramic brass disc used as driver for Synthetic Jet Actuators

The actuators were controlled through a NI LabView code that had multiple outputs that were synchronized to allow control over the phase of each output channel. The LabView signal was amplified using two Trek piezo amplifiers. The voltage output from each of the amplifiers was monitored to ensure that they were not introducing any phase lag/lead to the signal. The amplified signal was then used to drive the disc to create the synthetic jet. The final assembled array is shown in Figure 66.

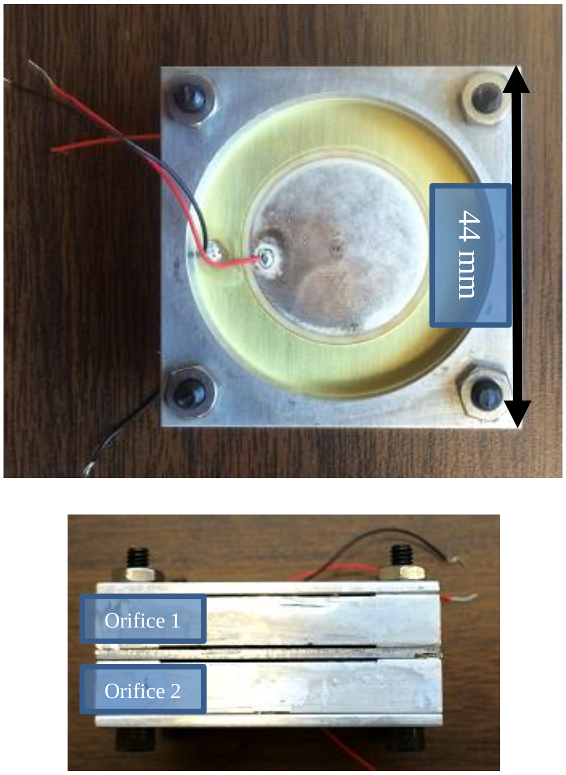

Figure 66 Assembled array of two Synthetic Jet Actuators

3.2 Characterization of synthetic jet actuators

3.2.1: Frequency and voltage characterization of the synthetic jets

Even though each synthetic jet is fabricated with small tolerance of ±0.05 mm the resultant output velocity can be significantly different from one actuator to another. In order to obtain two jets with identical velocity output it is therefore necessary to characterize them to identify an operating frequency and voltage at which they are as similar as possible. The frequency aspect of characterization is particularly important as it determines the strength of the jet produced. The cavity of the jet is an acoustic chamber that is connected to an exit orifice. This acoustic chamber is being excited by the driver. When excited at the Helmholtz frequency of the cavity, the velocity response will achieve its maximum value for a fixed excitation voltage. It is therefore desirable to operate close to, but not exactly at this value of frequency.

The piezo driver that is responsible for actuating the fluid inside the cavity has structural characteristics similar to that of a thin plate. When actuated it response has characteristics similar to that of a thin plate. This includes resonance at various frequencies corresponding to each excited mode. If the cavity is designed such that the Helmholtz frequency associated with it is close to one of the excitation modes of the disc, the output velocity magnitude is amplified significantly. Since the cavity has a fixed geometry the Helmholtz frequency cannot be altered. However the resonance frequency of the driver was dependent on the boundary conditions it was subjected to which were dependent on the torque value to which the screws were tightened. The selected value of 0.35 N-m corresponded to the case where the Helmholtz frequency and the mechanical frequency of the driver were close to one another, resulting in a higher velocity output.

The actuators were then characterized for frequency response for a fixed voltage value of 85 V. The frequency of the sinusoidal input was swept from 400 Hz to 1600 Hz in increments of 40 Hz. The response was measured using a TSI double channel IFA 300 Constant Temperature Anemometer (CTA) with a TSI single channel hot film probe, model #1210-20. The system was capable of sampling velocities at frequencies of up to 80 KHz, and therefore was able to fully resolve the actuation velocity waveform. The uncertainty associated with measurements based on calibration errors was ±0.2 m/s. The setup is shown below in Figure 67. The probe was placed 2 mm above the surface of the orifice at the mid-span location as shown below. The frequency response for both actuators is shown below in Figure 68.

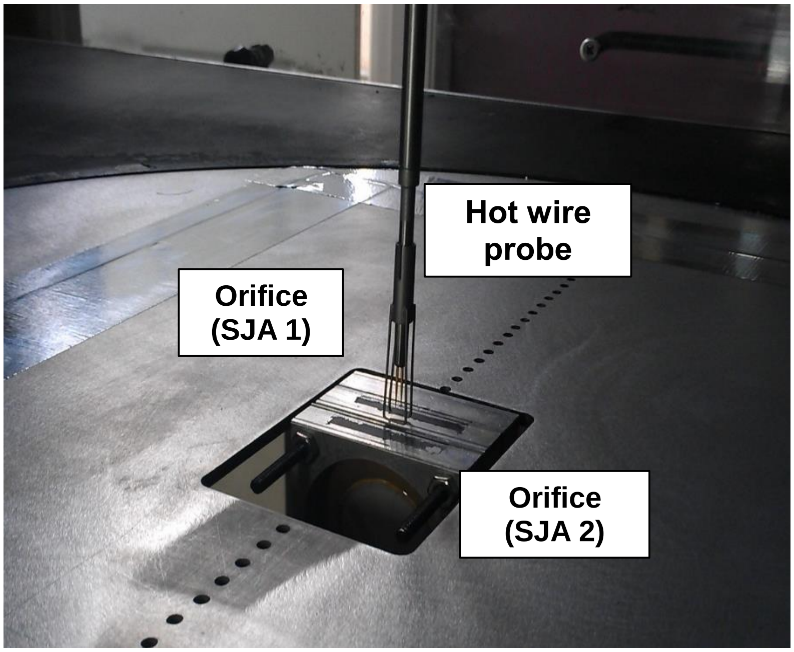

Figure 67 CTA frequency characterization setup

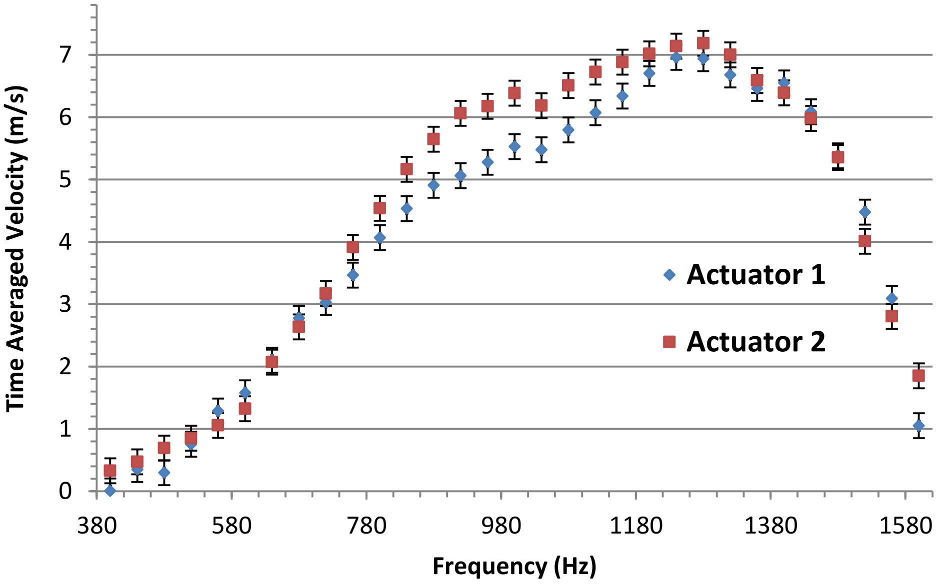

Figure 68 Frequency response of synthetic jet actuators

As shown in Fig, the characterization process was done while the actuators were installed in the wind tunnel they were to be tested in. This was done to ensure that the characterization conditions such as boundary loads, temperature, humidity and pressure, would be as similar as possible to the actual test conditions. The velocity results presented in Figure 68 are time averaged over 10 seconds. Each point on the curves is then calculated as the average of five time averaged sets of data. The maximum standard deviation within each of the five sets was approximately ±0.1 m/s. The error bars shown in Figure 68 are therefore based on the calibration error which is twice that value. The frequency response exhibits some important characteristics. Initially both actuators have a very similar response. Between 780 Hz and 850 Hz, the two curves begin to diverge slowly. Both curves attain a local maximum between 750 Hz and 1100 Hz. After 1150 Hz both curves exhibit similar behavior once again as they approach resonance at around 1290 Hz, and go past it to 1600 Hz. Dynamic laser displacement testing performed on the driver revealed the first two bending modes were around 780 Hz and 1260 Hz. The Helmholtz resonance frequency of the cavity can be calculated using the classic formula for cavity resonance shown in Equation 28.

$$f_{resonance} = \frac{c}{2\pi}\sqrt{\frac{A_o}{V_C L_o}}$$

Equation 28

Here A_o is the orifice area, V_c is the cavity volume, L_o is the length of the orifice nozzle and c is the speed of sound. Using this formula the cavity resonance was calculated to be approximately 1330 Hz. The observed system resonance was around 1290 Hz, within one increment of the calculated resonance. The overlap of the mechanical and acoustic resonance results in the jet mode corresponding to the large increase in velocity seen at 1290 Hz. Operating at this frequency would result in the highest velocity output for any given voltage. It would therefore be logical to fix the operating frequency for all sets of test to this value. However operating as resonance presents an issue with regards to phase locking. By comparing the driver voltage signal and velocity output it was observed that close to resonance the two signals would be out of phase by almost 75°. Furthermore the exact amount by which they the two curves were different varied for each actuator. Operating above the acoustic resonance condition also produced a phase lag. In addition to this the velocity response drop off past resonance was steep due to the fact that we are now operating at a frequency that is far from the mechanical resonance as well as acoustic resonance. In order to avoid these issues, an operating frequency of 1120 Hz, well below the acoustic resonance, where a phase difference of 23° (between the input voltage signal and the output velocity signal) was measured, was selected.

In addition to performing a frequency characterization the actuators also needed to be characterized for operating voltage response. This was necessary to determine the operating voltage necessary for each actuator to produce the similar velocity values. The results are shown in Figure 69.

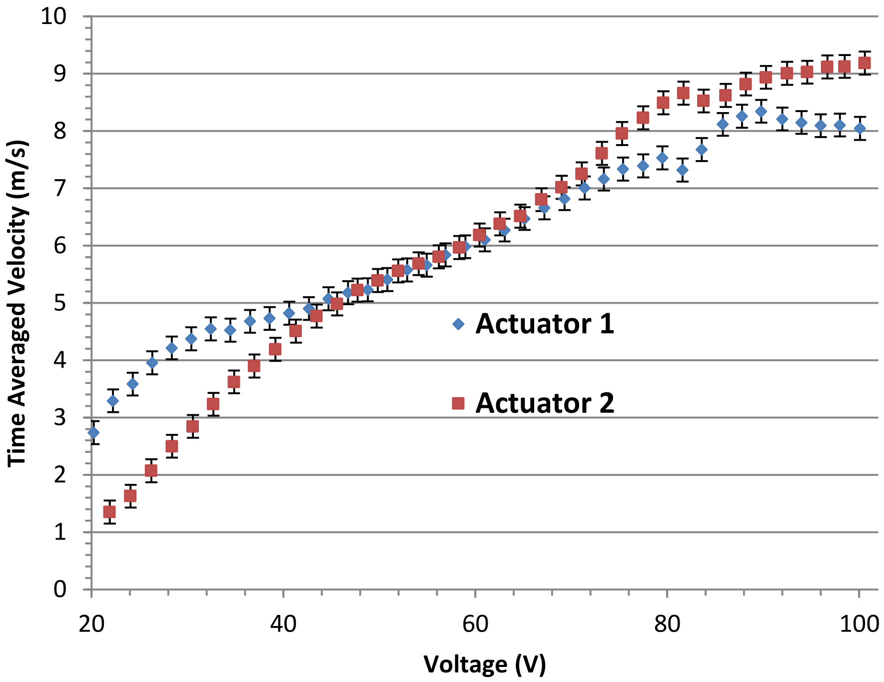

Figure 69 Voltage response for actuator characterization at *f* = 1120 Hz

The velocity response curves for voltage indicate that a similar and almost linear response within the 45 V to 70 V range, which is where the curves diverge. In order to obtain the desired velocity ratio values of $R = 0.9$ and 2.4, without overloading the actuators for extended periods of time, a minimum time averaged value of 7.5 m/s was required. In order to obtain that value Actuator 1 had to be operated at approximately 80V, whereas Actuator 2 required 74V. With these two voltage values the jet Reynolds number, Re_J, was identical for both jets and had value of 227.

3.2.2: Power Spectra analysis

While the CTA system was used to characterize the actuators under quiescent conditions due to directional resolution, point measurements and blockage constraints, PIV was performed to characterize the cross-flow interaction of the array. Since PIV is complicated measurement technique, a limited set of quiescent data was taken using both methods for purposes of comparison. This included a frequency domain analysis of the velocity at different heights above the orifice. The main reason why this was performed was to make sure that the PIV would be able to resolve the time averaged velocity accurately for the high frequency velocity waveform. While the PIV results will be presented in the model validation section, here we discuss the CTA measurements of how the frequency content changes as the height above the orifice changes. The results from tests at three different heights of 2 mm, 4 mm and 6 mm above the orifice are presented. The data was acquired at 40 KHz.

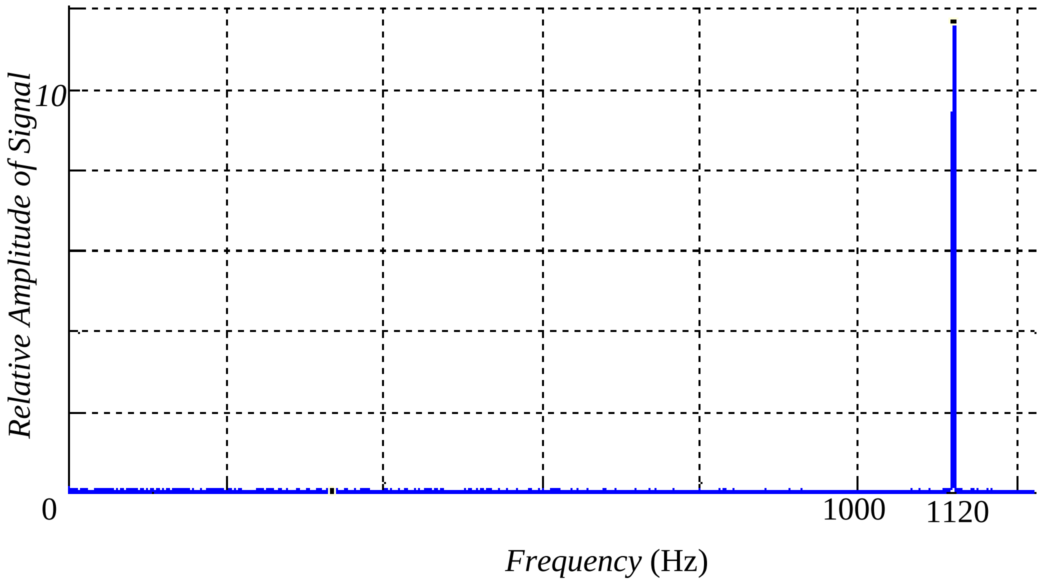

Figure 70 Frequency content analysis of CTA measured velocity 2 mm above the orifice

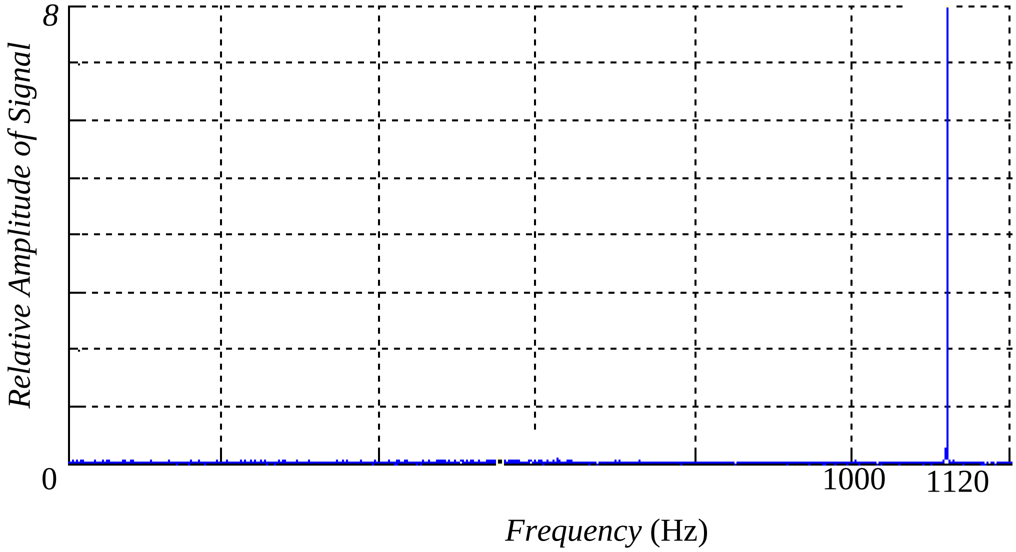

Figure 71 Frequency content analysis of CTA measured velocity 4 mm above the orifice

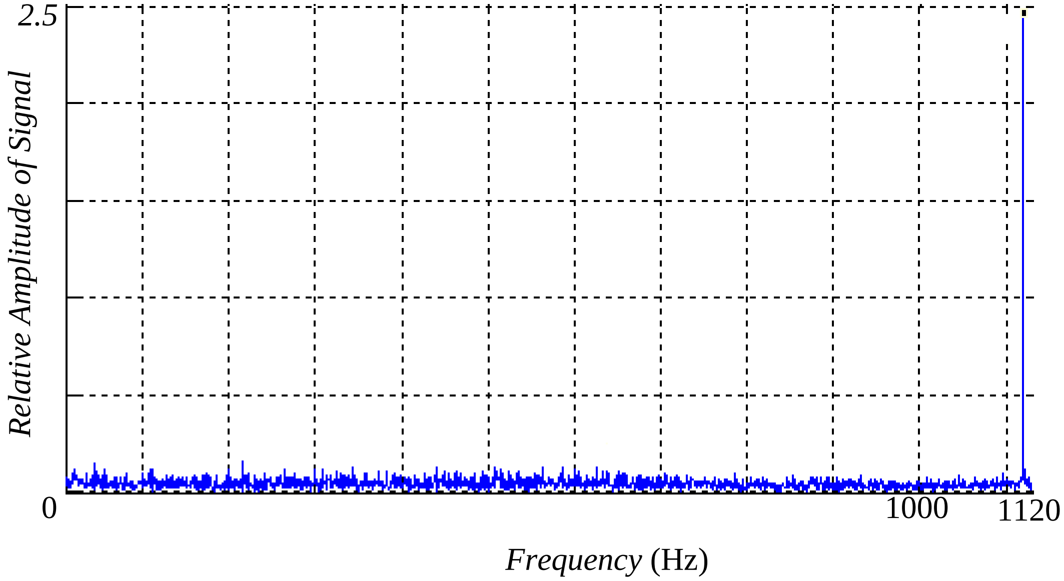

Figure 72 Frequency content analysis of CTA measured velocity 8 mm above the orifice

The frequency analysis reveals that 1120 Hz actuation waveform is the dominant one in the flow from a height of 2 mm to at least 8 mm above the orifice. However, the plots also reveal that the relative strength of the 1120 Hz waveform with respect to all other waveforms decreases almost five fold going from 2 mm to 8 mm. This information will vital in establishing the region above the orifice in which the PIV can accurately time resolve the velocity, and where it fails to do so.

3.3 Summary of design and characterization process

Based on a NASA design high aspect ratio finite span SJA were designed to validate the modeling techniques. The actuators were designed to have a 2D flow field in a region of at least 20 mm above the orifice and satisfy velocity ratio and geometric requirements of the modeling methods. CFD was used to calculate the appropriate cavity depth and aspect ratio to meet these requirements. The final design was used to build two actuators that were than characterized for frequency, voltage and velocity characteristics using CTA measurements. The characterization was used to select the operating frequency and voltage for each actuator in order to match the jet Reynolds number. Once the operating parameters were fixed the jets were characterized in terms of their frequency content as a function of height above the orifice. The results revealed that the amplitude associated with actuation waveform decreases fivefold going from 2 mm above the orifice to 8 mm.

Chapter 4: PIV Measurements for Model Validation and Flow Field Characterization

4.1 PIV and experimental setup

4.1.1: PIV specifics

Particle Image Velocimetry (PIV) was used to study the flow field produced by an array of interacting jets operating in a cross-flow. A high speed PIV system was used to obtain time averaged flow field velocities for the jets. Since the region of interest in the flow field was expected to be 2D, planar PIV was performed using a 4 MPx Phantom V641 camera, a Litron high speed Nd:YLF 10 KHz laser. The images were acquired and processed using DaVis software. The images were acquired at a rate of 200 Hz, for a time period of 1.4 s. The time duration, *dt,* between individual images of the pair was 30 μs. The images were processed in DaVis through a multi-pass decreasing interrogation window size algorithm. The first pass window size was 32 x 32 pixel at 50% overlap and the second pass window size was 16 x 16 pixels at 50% overlap. The window shape was square. A median filter was utilized to detect and remove outliers. A convergence criteria similar to that used for the CFD modeling was applied. The time average velocity was calculated for each point in the entire field. The change in this quantity as function of number of images was calculated for each point in the field. The sum of these residual values for the entire field was then plotted vs. the number of images used. The plot for the case of R = 2.4, s = 2.5b and φ = 0° is shown below in Figure 73. The results indicate that average value converges at around

100 image pairs. Which is the equivalent of 0.5 s of data acquisition. A more thorough analysis on PIV error is presented in the Appendix.

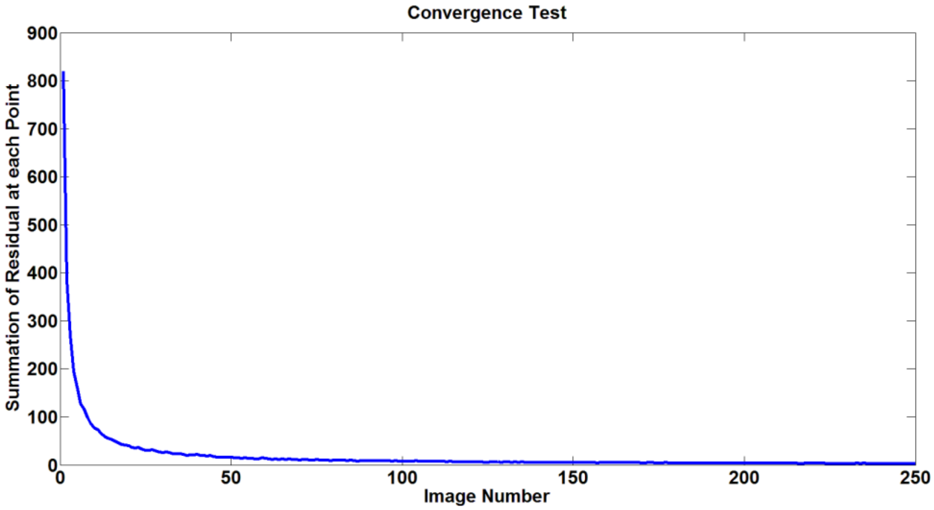

Figure 73 Convergence of the residual of the sum of time averaged velocities for the flow field

4.1.2: Experimental setup

An AeroLab suction type wind tunnel with a 0.71 m x 0.51 m x 1.21 m test section was used to perform the cross-flow tests. The actuators were flush mounted in the bottom floor of the wind tunnel. A 0.47 m diameter circular disc installed in a cutout at the bottom of the wind tunnel allowed for the actuators to be yawed with respect to the cross-flow streamwise direction. Although this was not one of the tested parameters this degree of freedom was necessary to orient the actuators in a direction that would allow for the analysis of 3D effects in SJA flow fields. This analysis will be presented in the following section. A schematic illustrating this setup in shown in Figure 74 and Figure 75.

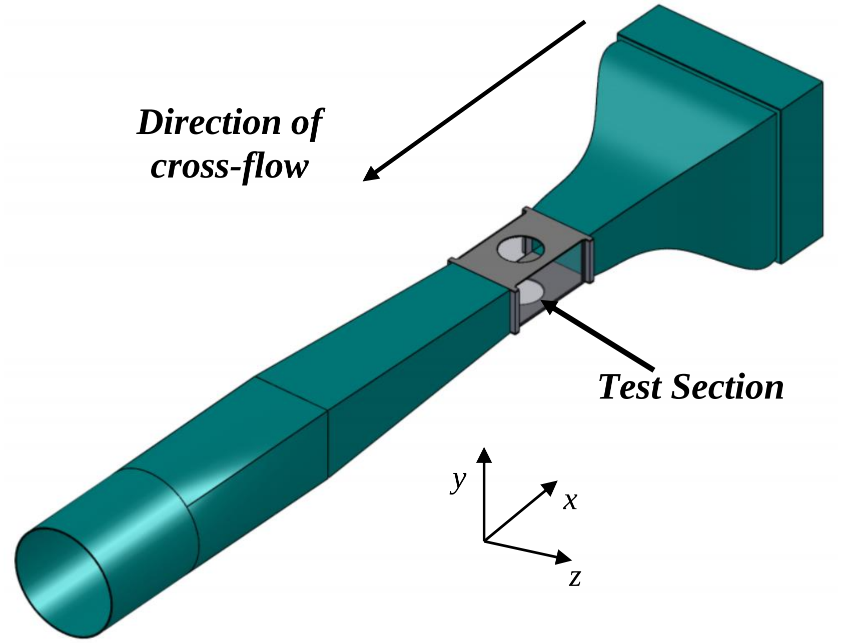

Figure 74 Schematic of wind tunnel showing direction of flow, test section and coordinate system

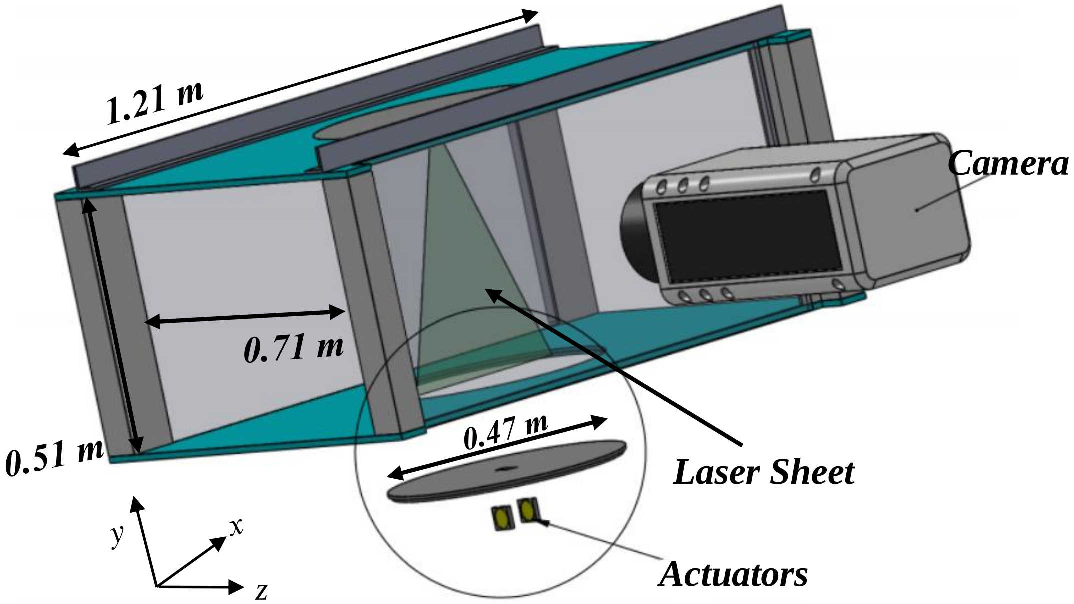

Figure 75 Expanded view of test section showing laser sheet, PIV camera and actuators

The wind tunnel was operated at velocities of 3.2 m/s and 7.7 m/s in order to achieve the desired velocity ratios. The manufacturer specified turbulence levels under these conditions were less than 2% and were measured to be less than 3.5% at peak.

The location of the first actuator was fixed with respect to the origin, and that of the second actuator was varied according the required spacing. PIV was performed in a 40 mm long and 30 mm high field of view (FOV) using a 200 mm fixed focal length Nikon lens. The camera was located such that the FOV would start 12 mm upstream of the first actuator. A schematic illustrating this setup is shown in Figure 76.

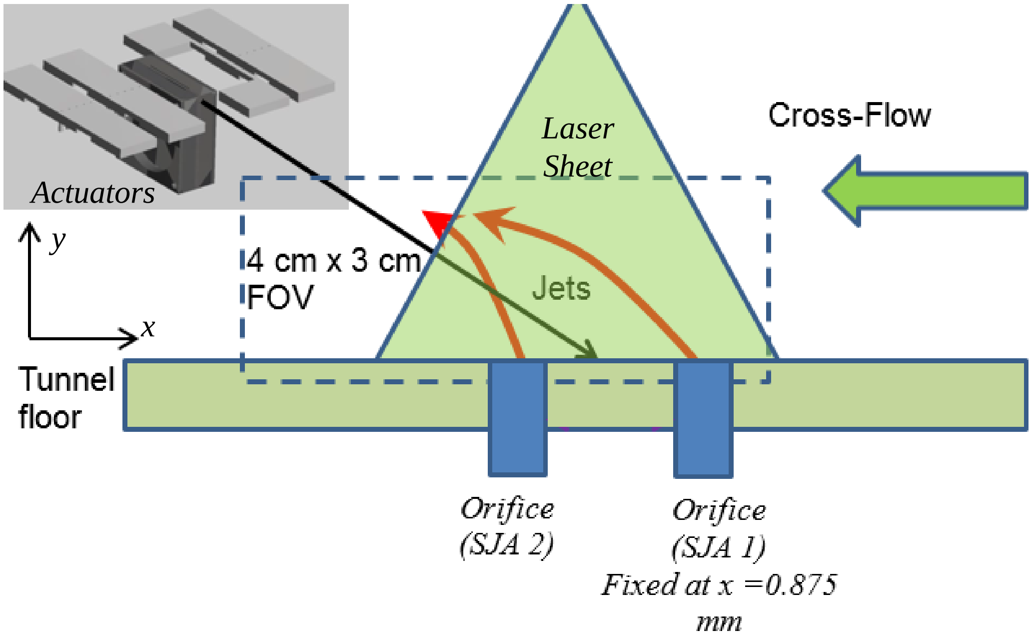

Figure 76 Illustration of PIV field of view and actuator setup

4.2 PIV vs CTA comparison of Synthetic Jet flow fields

Accurately measuring flow fields using PIV is complex process. There are several acquisition and processing parameters that must be tuned in order to obtain reliable results. In addition to this there are difficulties associated with the actual setup of the experiment as well. These include reflection and seeding issues. Such issues can lead to inaccurate results especially close to reflective and solid surfaces. In order to use the PIV to validate the models it was necessary to establish some type of bounds on the accuracy of the PIV results. The results from the CTA characterization of the single jet were used for this purpose. A magnitude and frequency content analysis was performed.

4.2.1: Comparison of velocities

The information obtained from PIV is in the form of velocities for an entire field. The CTA on the other hand returns point information. In order to compare the two results several points directly above the orifice were selected. Since the CTA system does not resolve flow direction or components, only magnitude results were compared. The RMS velocity for both PIV and CTA measurements was calculated over a fixed time. The results are shown below in Figure 77.

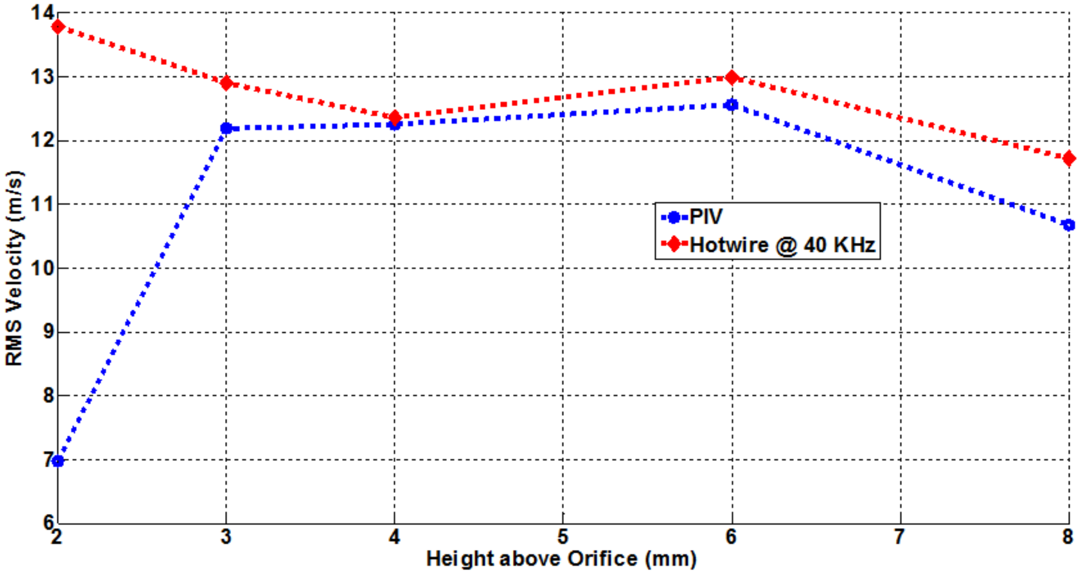

Figure 77 Comparison of RMS velocities measure by CTA (hotwire) vs. PIV

The PIV results are significantly different from the CTA measurements at a height of 2 mm above the orifice. There are several causes that could lead to these discrepancies. Right at the surface of the orifice, the PIV is plagued with reflection issues. In addition to that without the use of very expensive optics it is hard resolve the velocity along a 0.5 mm (orifice width) slot with sufficient spatial resolution. The hotwire results in this region are also subject to constraints. Very close to the orifice the jet has not undergone significant expansion in the *x*-direction. Placing the hotwire in this narrow stream displaces it significantly in relation to width of the jet. This displacement could cause a bias in the velocity. The results for both methods begin to agree within 10% as we move from 3 mm above the orifice to 6 mm above the orifice. Past this height the results appear to diverge slightly however up until the measured 8 mm the maximum deviation is approximately 12%.

4.2.2: Comparison of frequency content

Since the two acquisition systems operated at significantly different sampling rates a comparison of the frequency content of the results was performed. The PIV data was acquired at a maximum of 500 Hz whereas the hotwire was sampled at 40 KHz. The actuation waveform had a frequency of 1120 Hz. Based on the Nyquist-Shannon sampling criteria the PIV sampling frequency is not high enough to fully resolve the actuation waveform. This does not however imply that the PIV cannot measure the time averaged effect of actuation. A frequency analysis similar to the one performed in Section 3.2.2 was performed on the PIV data to obtain better insight into the frequency content of the PIV data. The results for different heights are shown in the figures below.

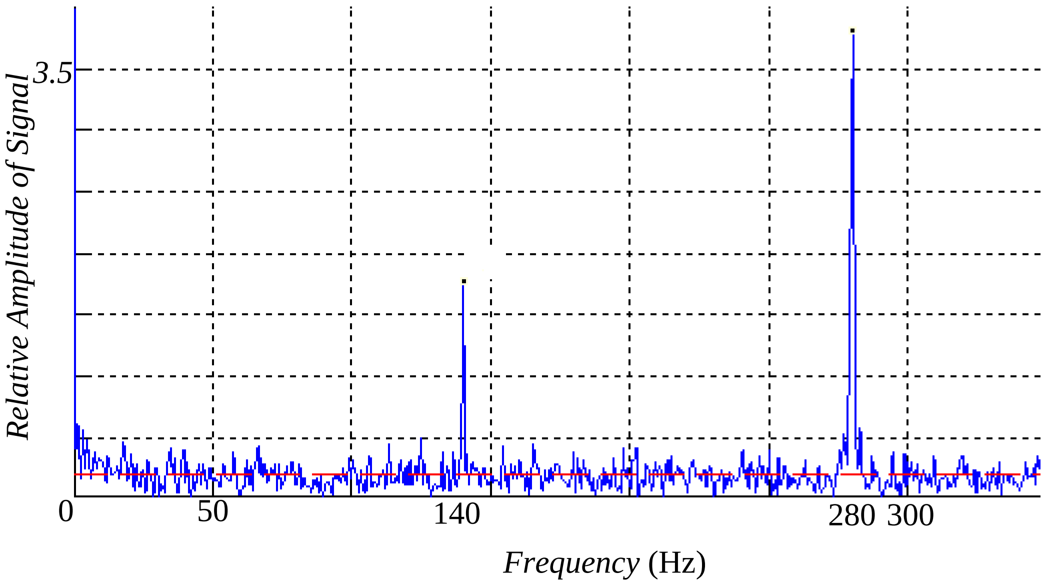

Figure 78 Frequency analysis of PIV data obtained at 2 mm above the orifice (red line indicates average magnitude)

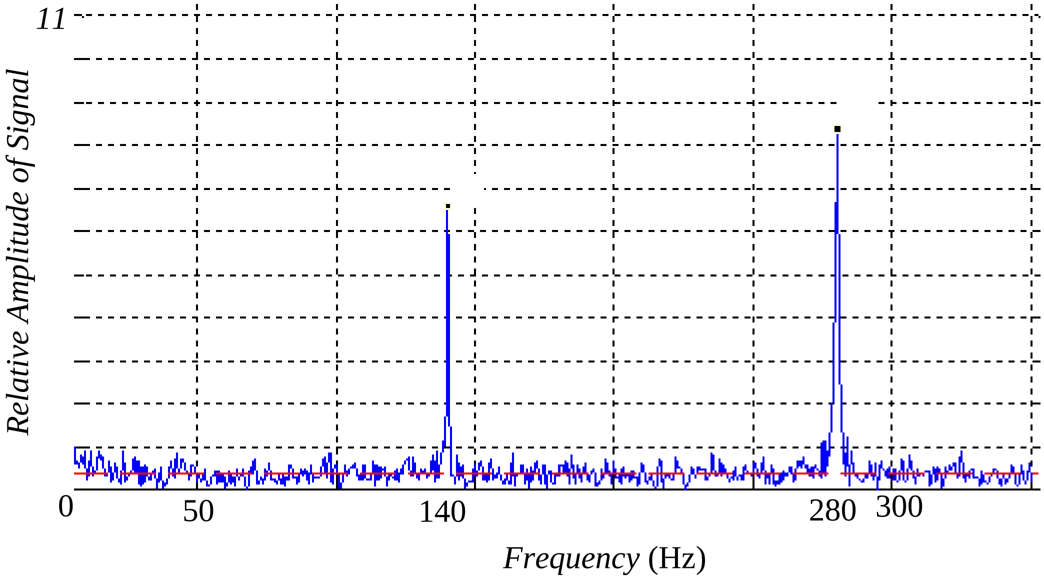

Figure 79 Frequency analysis of PIV data obtained at 4 mm above the orifice (red line indicates average magnitude)

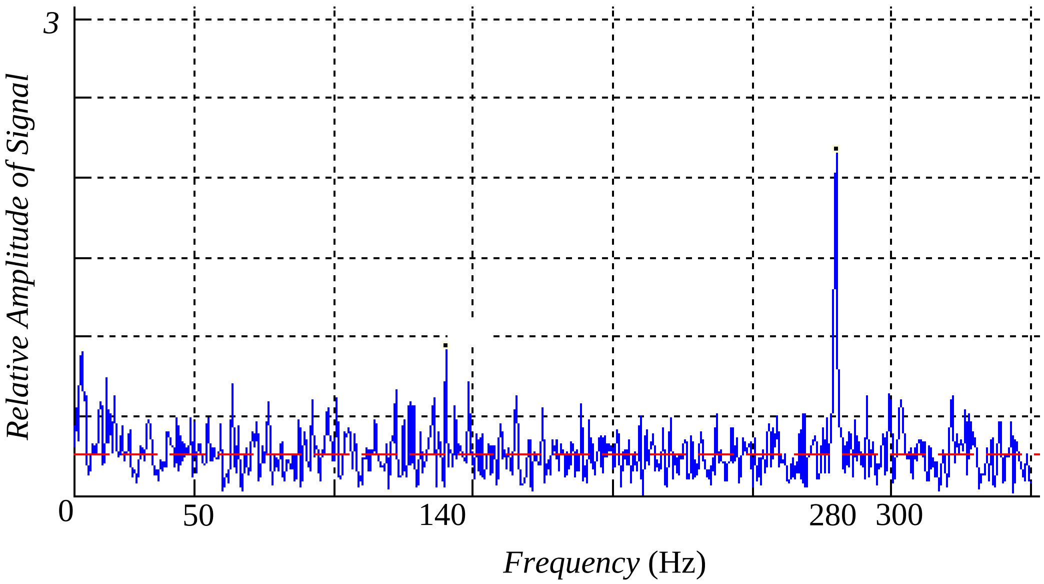

Figure 80 Frequency analysis of PIV data obtained at 8 mm above the orifice (red line indicates average magnitude)

The frequency analysis reveals that 1120 Hz waveform is aliased by the 500 Hz and appears as a 1/4th and 1/8th multiple at 280 Hz and 140 Hz respectively. The aliased waveform first shows up at a submultiple that satisfies the Nyquist-Shannon criteria. The lower frequency waveforms for the PIV power spectrum have a higher relative amplitude in comparison to the CTA power spectrum. This could be possible to the introduction of low frequency noise due to spurious vectors introduced in the PIV processing. Unlike the CTA results where the strength of the actuation waveform decreased as a function of height away from the orifice, for this case the relative magnitude first increases going from 2 mm to 4 mm. This suggests that very close to the orifice the signal to noise ratio is high for PIV acquired data implying that the reflections are in fact adding noise during the processing. The relative strength of the aliased actuation waveform increases by factor of 2 at a height of 4 mm indicating a reduction in noise level. At a height of 8 mm above the orifice the relative strength decreases but this is not due to the presence of noise at this location. As we move away from the orifice the frequency content of the flow shifts from high to low due to shear layer interactions, which is what we observe in Figure 80.

The results shown above and in Section 4.2.1 indicate that the PIV results are not very reliable very close to the orifice (2 mm). As we move away from the orifice the accuracy improves. This information will be used to establish a region for the flow field in which the modeling results can be validated.

4.3 PIV study of the 3 dimensionality of a SJA

In order to validate the 2D flow assumption PIV was performed in the *yz*-plane at three different *x* locations and the *z*-component of velocity was calculated. The time averaged *z*-velocity component was plotted as a function of the height above the orifice for mid-span location. The time averaged velocity field is shown in Figure 81.

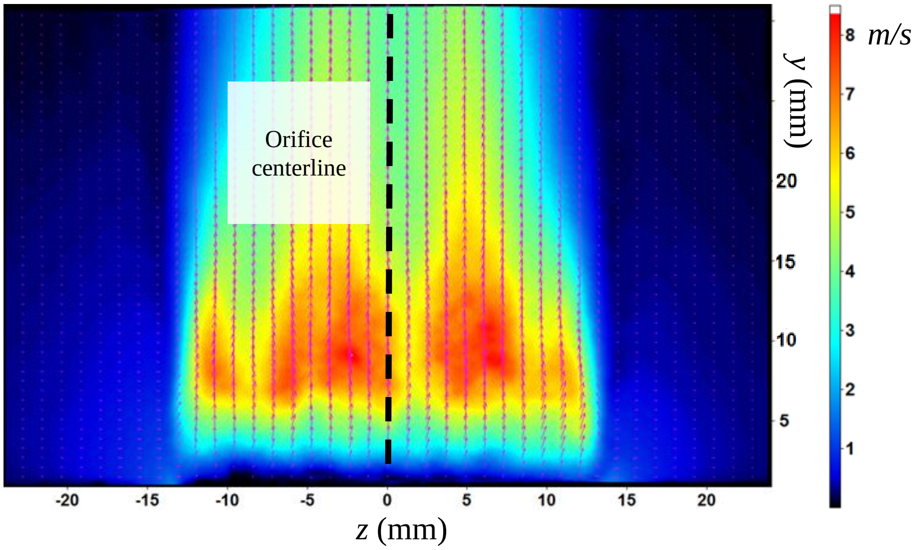

Figure 81 Time averaged velocity vector and magnitude plot (*yz*-plane along the span of the orifice)

The velocity vectors indicate a very small component in the *z* direction with most of the velocity in *y* direction. The *z*-component slightly increases towards the end of the span which causes a slight contraction of the jet in the spanwise direction as we move away from the orifice. The contraction however is small and mostly limited to the outer edges of the plume. Going from a height of 0 mm to 15 mm the jet appears to have contracted about 1 mm on each of the ends. The actual *z*-component of velocity (*w*) as a function of height is plotted in Figure 82 for different offsets about the span. Each curve was obtained from PIV performed along the span and at two locations 1 mm and 2 mm away from the center of it.

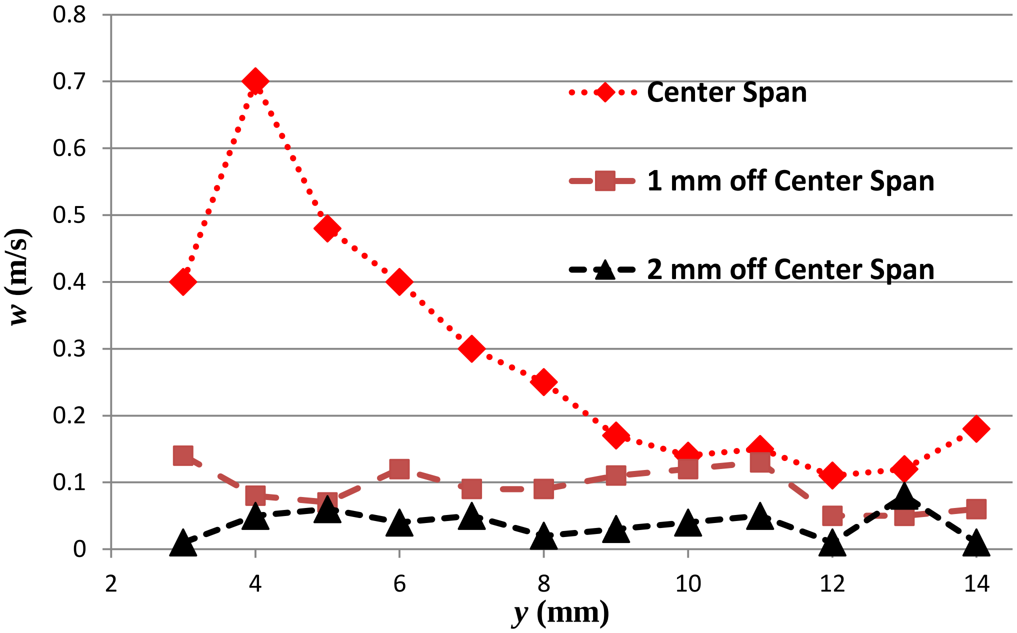

Figure 82 *z*-component of time averaged PIV velocity at varying locations

The results indicate that the out of plane component (*z* velocity) was always less than 10% (peak on the red line at y = *4* mm) and most of the times less than 5% of the *y*-velocity. The 2D flow assumption for modeling purposes is therefore justified and 2D PIV can be used to validate the models.

4.4 Model validation and flow analysis through PIV

4.4.1: Validating model predictions of spacing effects

In Section 2.4.3 the effects of spacing as predicted by the CFD model were presented in terms of the influence of spacing on the jet centerline trajectory. CFD predicted that spacing the jets apart resulted in a slightly increased trajectory deflection. In this section the modeling results from the three models are compared to PIV and their ability to predict is compared. Since sensitivity to parameters is one of the features that the modeling was used to analyze, the focus of this section would be on the effects of spacing only. Coupling effects between various parameters will be studied in subsequent sections. The velocity ratio R, and the phase angle φ are therefore fixed at 2.4 and 0° respectively. We start by comparing PIV results of spacing effects.

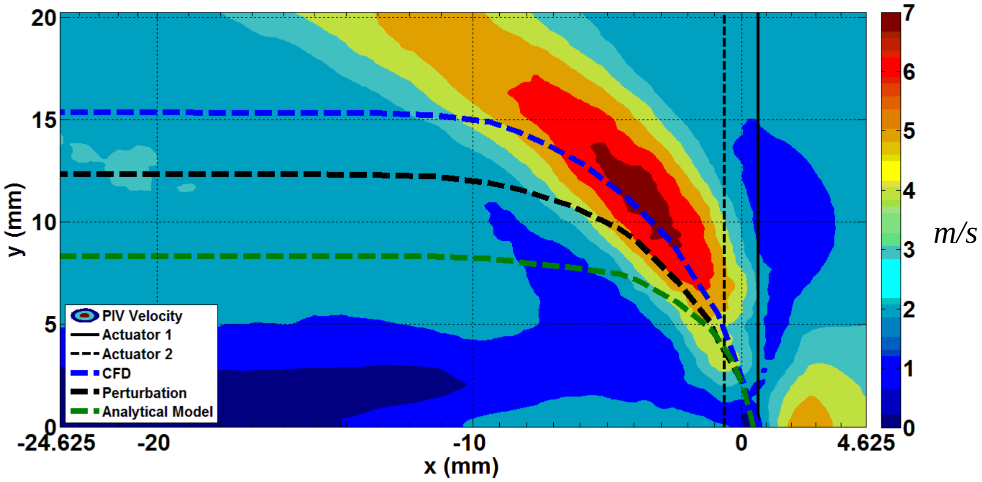

Figure 83 PIV validation of predicted jet centerline trajectories with PIV for *R* = 2.4, *s* = 2.5b, *φ* = 0°

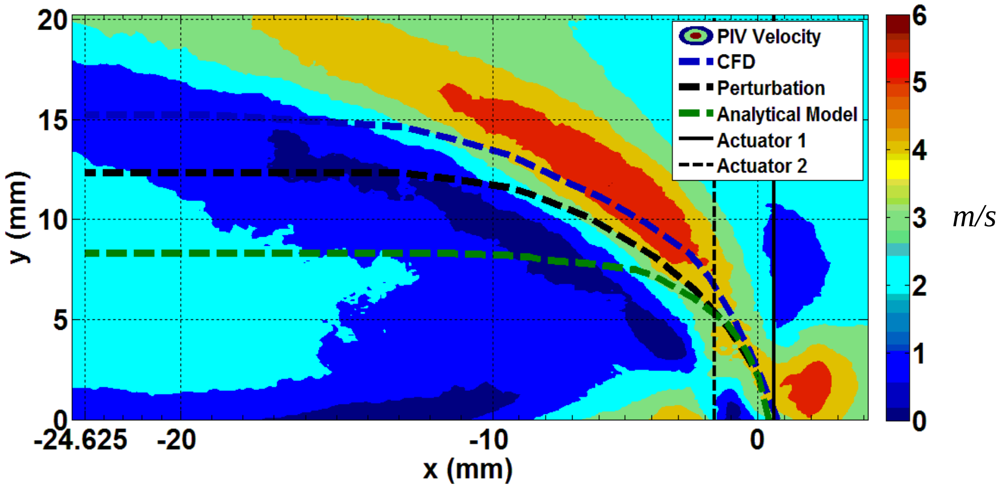

Figure 84 PIV validation of predicted jet centerline trajectories with PIV for *R* = 2.4, *s* = 4.5b, *φ* = 0°

Shown in Figure 83 and Figure 84 are the PIV time averaged velocities with the three predicted trajectories superimposed on them. Comparing the two PIV results the we notice that the peak velocity magnitude in the plume has decreased from around 7 m/s to 6 m/s. That represents a 14% decrease. In addition to the decrease in magnitude the direction of the trajectory is also different. Increasing the spacing leads to a higher deflection of the jet trajectory in the direction of the cross flow. Comparing the experimental results to modeling predictions, the CFD model is by far the more accurate. For the case of *s* = 2.5*b* it tracks the center of plume with less than 10% error to height of 12 mm (24*b*) above the orifice. For heights of less than 10 mm (20*b*) the difference is less than 7%. For the case of *s* = 4.5*b* the full cavity CFD represented the more accurate solution again. It tracked the trajectory within 10% error up to a height of 12 mm (24*b*) above the orifice. The perturbation solution was less accurate then the full CFD in general. For both spacings the model tracked the centerline within 10% up until a height of 5 mm (10*b*). Past this height the solution would still follow the general direction of the trajectory, however the accuracy decreased to about 17% error going from a height of 5 mm (10*b*) to 12 mm (24*b*) above the orifice. The analytical solution follows the trajectory to within 12% only up until a height of 5 mm (10*b*) above the orifice for both spacings. After this height the prediction rapidly diverges. Predictions from all models suggest that jet is completely deflected in the direction of the cross-flow within the observation window. The PIV results suggest that this is not the case. A possible explanation for this observation is the fact that although the flow from the jet may be 2D within the observed window, the cross-flow itself is not as it encounters the jet. For a purely 2D problem the orifice span would have to be close to the width of the test section, which is not the case for the experimental setup. When the cross-flow encounters the jet, it is either entrained in it, or deflected around it due to the blockage effect. For the experimental setup used in this study the cross-flow had the option of going around the jet (*z*-direction deflection) as well as going over it (*y*-direction deflection). As a result the actual vertical blockage effect of the cross-flow on the jet is smaller than what is predicted by the models. The comparisons in Figure 83 and Figure 84 seem to suggest that any change of parameters (spacing in this case) that leads to the plume deflecting in the direction of the cross-flow leads to a degradation in modeling predictions for the location of the centerline trajectory. It will be shown in the following sections that directional changes do in fact influence the accuracy of the prediction. The effect of directional changes on the behavior of the centerline trajectory location differs for the decay rates and the momentum coefficient. This characterization will be detailed as function of trajectory angle in section 4.4.4.

With an estimate of the accuracy of the three models available, their predictions were also used to study the parameter sensitivity. The spacing results for s = 2.5b and

4.5*b* are presented in Figure 85 for the perturbation model results. Like the CFD comparison which was presented in Figure 53 they indicate a very small increase in deflection for the change in spacing. The spacing results from the analytical model showed almost no sensitivity to the parameter over the given range. In addition to this results for the spacing *s* = 3.5*b* showed very little change in the path of the centerline.

The PIV results for these two cases shown above indicate that while there is a change in the path of the centerline trajectory, it is not that significant. The magnitude however changes by almost 14% at the core of the plume. This effect will be analyzed in more detail when studying the coupling effects of parameters in sections to follow.

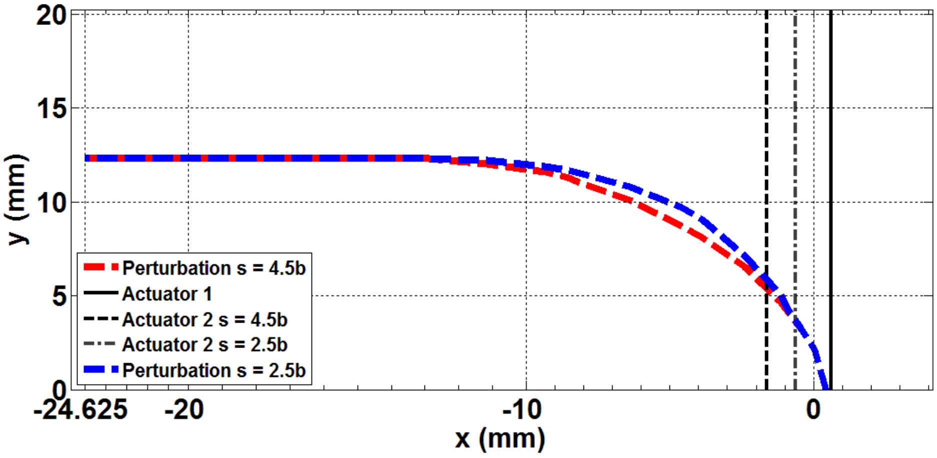

Figure 85 Perturbation predictions for jet centerline trajectory for *R* = 2.4, *s* = 2.5*b* and 4.5*b*, *φ* = 0°

4.4.2: Validating model predictions of velocity ratio effects

For the two velocity ratios analyzed all the models predicted a significant increase in deflection in response to a decreasing velocity ratio. In order to study and validate the effect of velocity ratio only, the spacing and phasing parameters for this section are fixed to 2.5*b* and 0° respectively. The model predictions for the centerline trajectory along with the PIV data for a velocity ratio of 0.95 are shown below in Figure

86. For this case the CFD results track the trajectory within 10% to height of 12 mm (24*b*) above the orifice. For the case of the high velocity ratio the CFD predicted trajectory would start out close to the experimental results and then would flatten out relatively quickly. The explanation as provided in the previous section as to why this happens was that the 2D modeling led to an increased blockage effect. For the case of the low velocity ratio shown in Figure 86 below, we see that since the trajectory is vectoring in the direction of the cross-flow, the actual physical blockage it experiences is reduced, and hence the predicted results tend to agree with the experiment for larger *S*-coordinate values (further along the trajectory).

For this velocity ratio the CFD is over predicting the resistance of the trajectory to deflection (measured deflection is greater than calculated deflection). The perturbation solution on the other hand does not over predict the resistance and follows the plume center most accurately (error less than 8%) until a height of 7 mm (14*b*) above the orifice. The analytical solution also predicts the trajectory to within 13% of the experimental results for heights less than 7 mm above the surface.

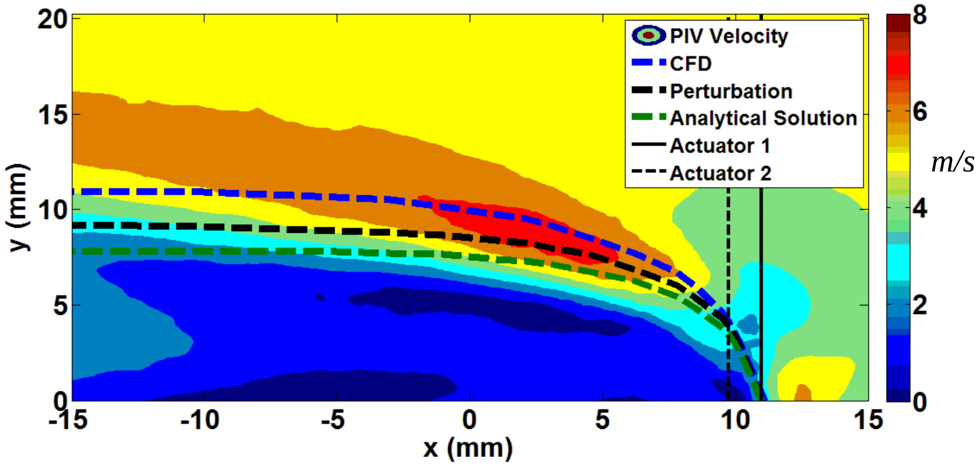

Figure 86 PIV validation of predicted jet centerline trajectories with PIV for *R* = 0.95, *s* = 2.5b, *φ* = 0°

The results for R = 2.4 were presented in Figure 83.The decay curves for the two velocity ratios, along with the model predicted decay rates are shown below in Figure 87 and Figure 88 for R = 2.4 and 0.95 respectively. For the high velocity ratio we observe that neither of the models predicts the decay rate accurately. The CFD is the closest of the three solutions to the actual experimental curve. According to all three models the velocity reaches its peak value and decays to the nominal cross-flow for S < 20 mm. Whereas the experimental results indicate that the velocity inside the plume maxes out at around S = 14 mm and does not fully decay to cross-flow value within the observation window. The results for all three modeling curves predict a faster decay than the measured values for the high velocity ratio (smaller jet deflection). In general the more resistance a jet faces the faster it decays. The over predicted decay rate for R = *2.4* is thus an indicator that the blockage predicted by the models is higher than the blockage in the wind tunnel.

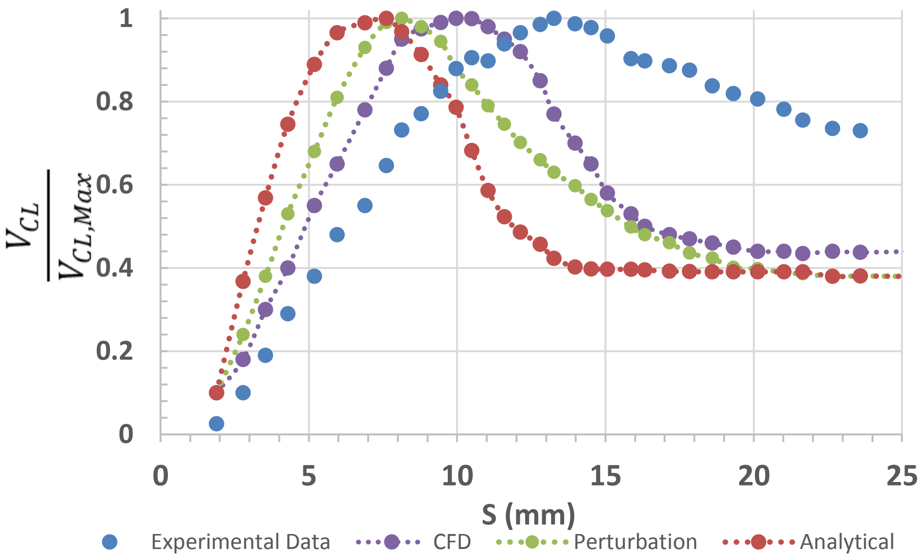

Figure 87 Velocity decay predictions and PIV measurements R = 2.4, s = 2.5b and φ = 0°

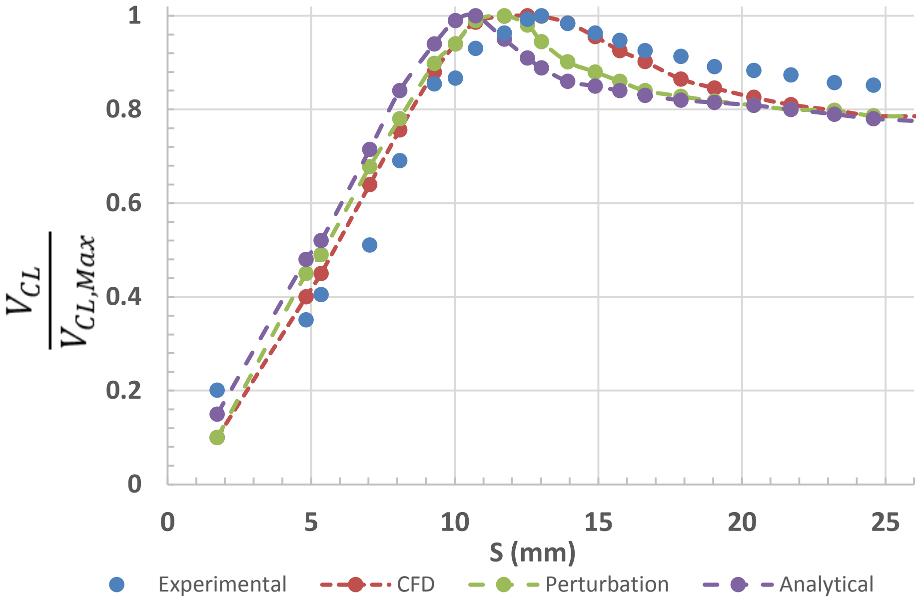

Figure 88 Velocity decay predictions and PIV measurements *R* = 0.95, *s* = 2.5*b* and *φ* = 0°

All modeling results for the low velocity ratio case agree with the experimental results throughout the observation domain to within 13% for all *S*. All three models suggest that the jet velocity peaks at an *S* value of around 12 mm. The experimental results indicate that the measured peak was at *S* = 13 mm. The decay after the peak is also modeled fairly accurately in terms of trend by all three models, with the CFD being accurate to within 9%. For the experimental results the centerline velocity decay exhibits fluctuation as it approaches maximum value. This is because towards the high velocity region of the plume the velocity gradients are large. PIV post-processing exhibits sensitivity to these gradients in sense that if the interrogation window over which the processing is done is not small enough, the particles can be moving in different directions within the window. The interrogation window size was limited by the observed pixel displacement and was chosen to be the smallest possible while trying to satisfy the pixel displacement constrains.

4.4.3: Flow analysis and model validation of phasing and coupling effects

The modeling results of section 2.4 predicted that flow field exhibits the highest sensitivity to the relative phase operation. While going over the range of phase angles the plume direction and strength varied significantly. The model results predicted a significant change in the value of the momentum coefficient associated with the flow field. The momentum coefficient for the experimental results is calculated using the same method as that for modeling results. Shown in Figure 89 are the predicted and measured results.

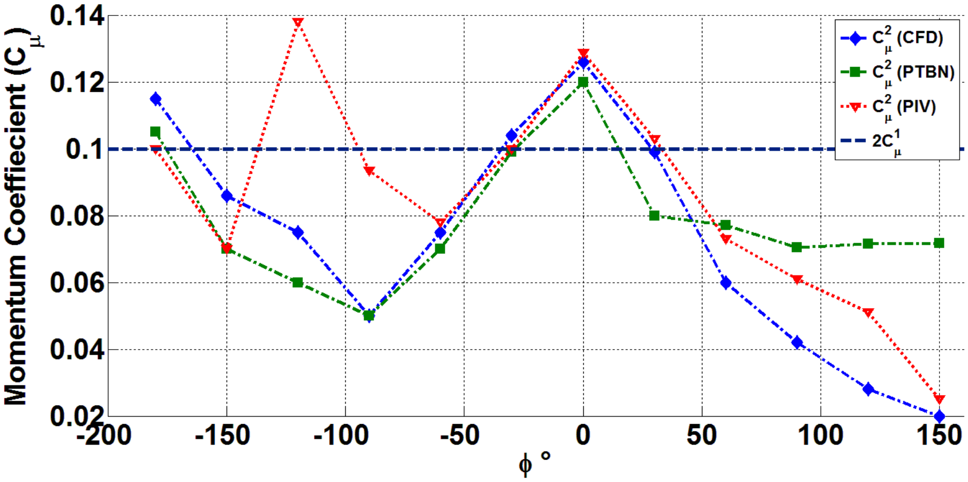

Figure 89 Momentum coefficient validation and analysis *R* = 2.4 & *s* = 2.5*b*

For φ = -180° the predictions from both models are within 12% of the experimental results. From $\varphi > -180°$ to $\varphi < -50°$ both models predict a steady decline in the value of momentum coefficient. The experimental results however indicate a local maximum at $\varphi = -120°$. The reason for this discrepancy between predicted and measured values is the presence of a strong recirculation region that was observed in the immediate wake of the jet (detailed in the flow field results). This recirculation region feeds high momentum flow back into the jet causing the observed increase. A well-defined recirculation region was observed for the case of φ = -120° whereas for φ = -90° this feature was not well defined, instead a region of high velocity feeding back into the jet in the immediate wake was observed. This recirculation region is not predicted by any of the models. It is possible that the increased blockage and jet deflection predicted by the models force the jet closer the flat plate boundary sooner, hence suppressing this recirculation region. The model and experimental results thus vary significantly within this range for φ. For -30° < φ < 30° the CFD and perturbation model results are within 10% of the experimental results. Beyond this range the experimental results suggest that the momentum coefficient drops of at an almost linear rate. The perturbation model predicts a drop as φ approaches 30° but the values level out after that point. The values predicted by the CFD continue to decrease and the results match the experiments to within 15% up until φ = 60°. Past this value of φ they differ significantly (up to 25%) from the experimental results with the models under predicting the deflection. This observation is consistent with over prediction of blockage for these values of phase angle. The observed discrepancies that occur in Figure 89 for φ = 120° and φ > 30° will be explained using the PIV velocity magnitude field plots below. The most significant result of changing this parameter occurs at value of φ = 0°. Shown in Figure 89 is a line that represents two times the momentum coefficient for a single actuator. For phase angles other than zero (and -120° as indicated by the experimental results) the predicted and measured values of the momentum coefficient are below this line. This means that the sum of the momentum coefficients of the two actuators is less than 2 times that of an individual actuator operating under similar conditions. However, for this particular value of φ, s and R, the interacting actuators in an array can operate more efficiently than an individual actuator. This phenomenon happens due to vorticity induced reinforcement and was predicted and explained for this particular case of parameters in section 2.3.1. The vortex pairs generated by both actuators split and repair in such a way that at the onset of the ejection phase there are two vortex pairs above the orifice that are inducing a positive velocity component (reinforcing ejection) at the orifice Figure 40. This results in momentum coefficient value increases of around 30%. The sensitivity of this phenomenon to these parameters is very high. Altering either the spacing or the velocity ratio results erases these gains. Physically this can be explained in terms of the advection velocity of the vortices (dependent on jet velocity and cross-flow velocity), the distance between the two orifice, and the arrangement of vortices with respect to the orifice. As the vortex pairs split and repair, (Figure 38, Figure 39, Figure 40) they advect away from the orifice and in the direction of the cross-flow. Their final arrangement at any given time depends on how long and how fast they advect. If this time and velocity are such that the CCW and CW vortices arrange themselves around the downstream orifice to enforce the ejection phase the velocity output is increased. Altering any one of these quantities alters this balance and could result in detrimental effects. This fact can be observed for most of the cases of phase angle shown in Figure 89.

The response of the centerline trajectory to the change in phase is shown in the figures below. The cases presented below are in increments of 60° to emphasize the differences in the flow between two successive phase angles. The trajectory results predicted by all three models for φ = -180° are in excellent agreement with the experimental data as shown in Figure 90. For this particular phase angle, the jets are strongly vectored in the direction of the cross-flow meaning the exerted blockage is small. Moving to the -120° the curves for all three predictions begin to diverge from the experimental results. In Figure 91 we see that CFD and perturbation solution follow the core of the plume fairly accurately in the observation window. The analytical solution follows the trend in general but the values are off by as much as 15%.

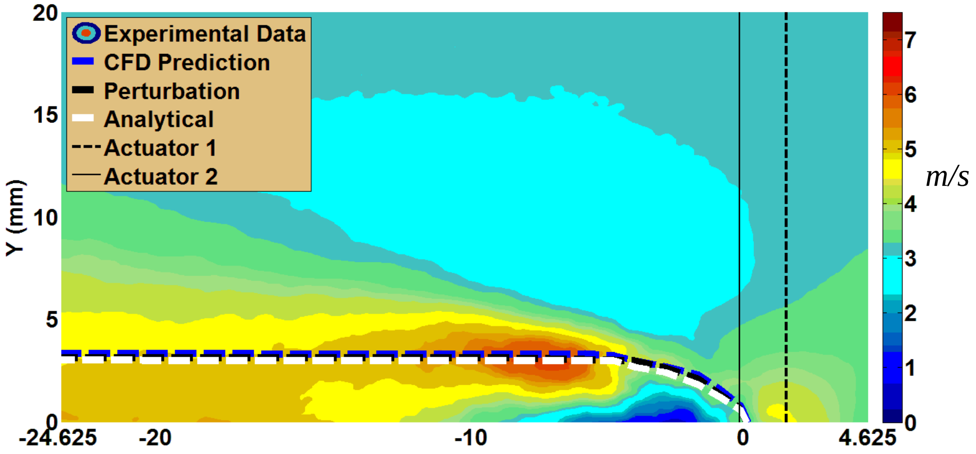

Figure 90 Model validation and flow field analysis for phasing effects φ = -180°

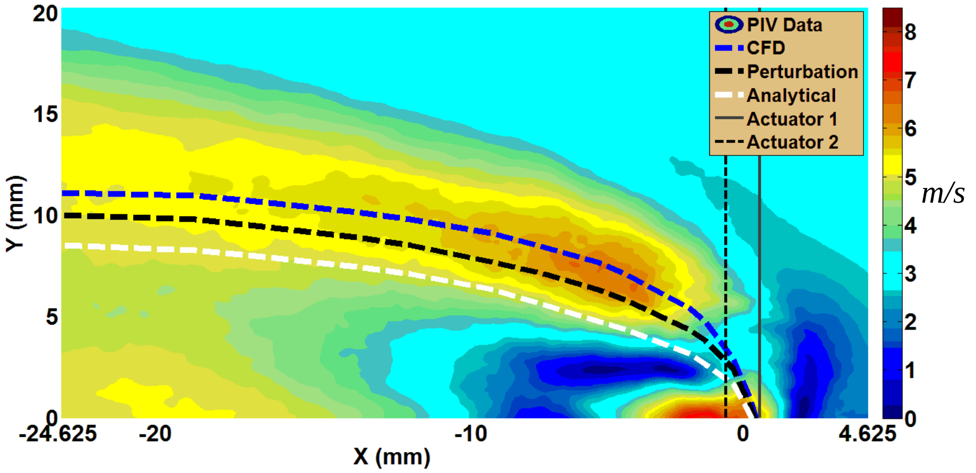

Figure 91 Model validation and flow field analysis for phasing effects φ = -120°

As phase angle is increased we observe that the trajectory begins to vector in the direction of the cross-flow. Shown in Figure 92 and Figure 93 are the results for -60°and 0°. For the -60° case the CFD and perturbation solution track the trajectory to within 10% for y-values less than 10 mm (20*b*). The analytical solution at this phase angle is has a 10% accuracy for heights less than 5 mm only. Beyond that value it follows the general direction of the plume however the values are significantly off.

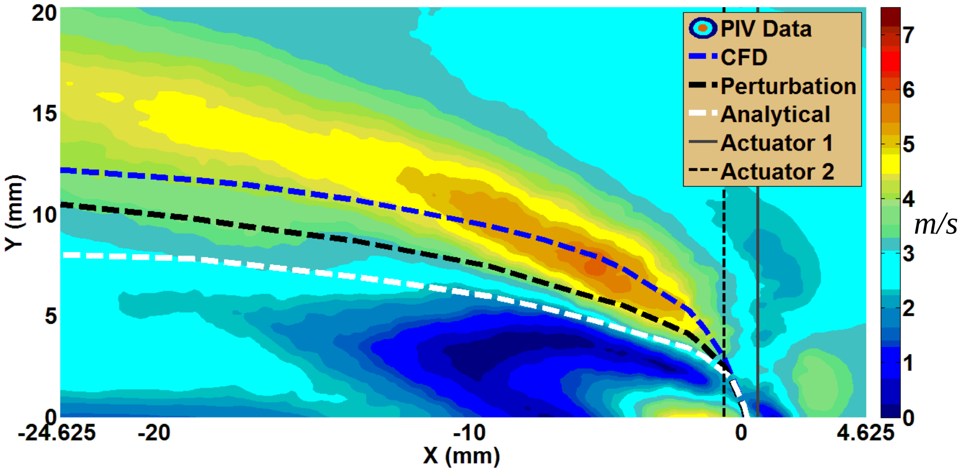

Figure 92 Model validation and flow field analysis for phasing effects *φ* = -60°

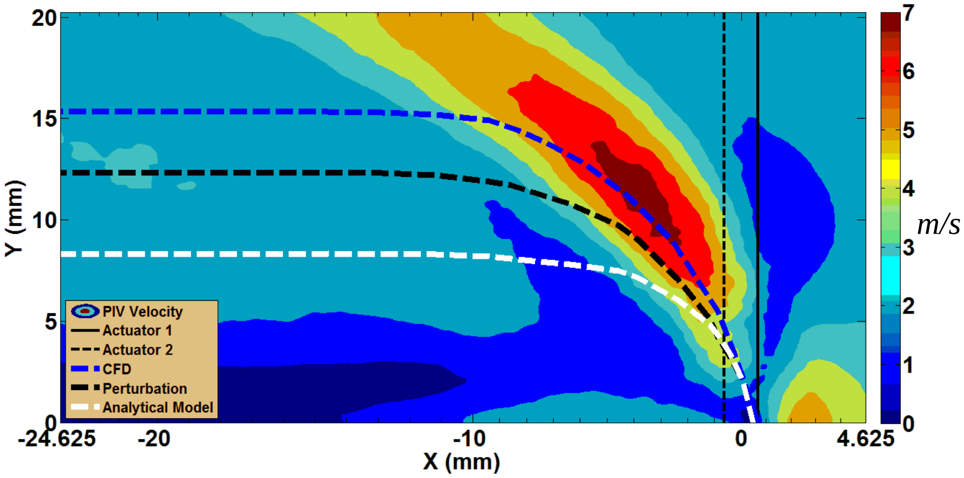

Figure 93 Model validation and flow field analysis for phasing effects φ = 0°

At a phase angle of 0° all models start out close to the experimental values. The analytical and perturbation solutions begins to diverge around 5 mm. The CFD however follows the plume to within 12% accuracy as far as 11 mm (22*b*) away from the orifice. For the case of positive 60° shown below in Figure 94 all the models became less than 15% at heights of 5 mm (10*b*) or less.

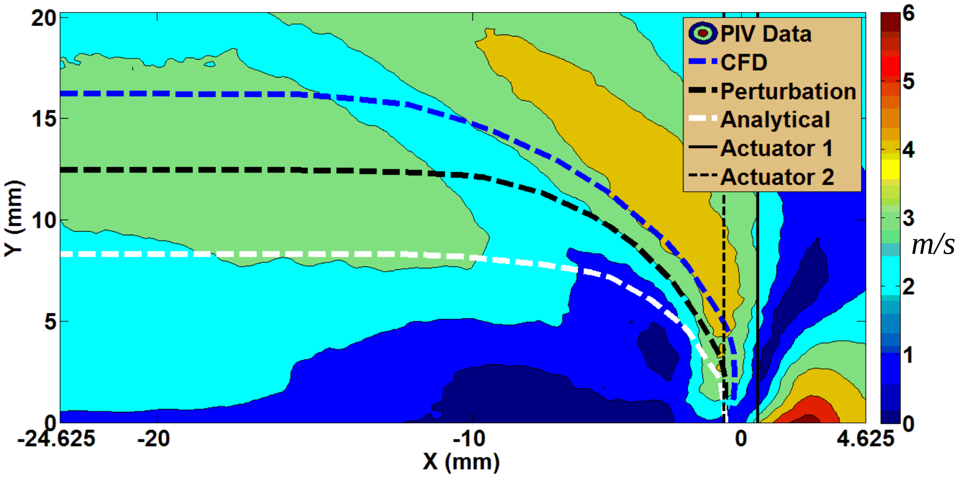

Figure 94 Model validation and flow field analysis for phasing effects φ = 60°

The experimental results provide insight into why the momentum coefficient drops drastically going past 30°. As the trajectory vectors into the jet the impedance that it faces is increased significantly. This causes the jet flow to slow down resulting in weaker plumes. For the experimental results high deflections correspond to weaker jets, however the amount by which they weaken is less than what it would be for a purely 2D flow (physically corresponding to actuators spanning the length of the wind tunnel). While the data has value in contributing to understanding of flow field physics, past a phase angle of φ = 0° the qualitative value for validation is minimal. Comparison of the predicted and measured deflections highlight the significance of the blockage effect and the range over which the experimental data is useful for validation purposes. With increasing phase angle the jet begins to vector in the direction of the cross-flow causing it to displace in ways that cannot predicted by the 2D models. The case for φ = 60° is shown for the purposes of illustrating this effect. The jet initially deflects into the cross-flow as shown by the experimental results. Neither the perturbation nor analytical model reproduced this. The CFD initially does suggest that this is the case but the prediction decays rapidly for increasing height above the orifice. The validation process was thus limited to parameters that had deflected trajectories in the direction of the cross-flow.

The increase in momentum coefficient shown by the experimental results at a phase angle of -120° will now be explained using the experimental flow field results. Figure 91 shows the presence of a recirculation region in the wake of the jet. This recirculation region feeds back into the jet close the orifice resulting in an increased jet velocity and higher momentum coefficient. Given the influence of that the phase angle has on the flow field of a developing SJA, it is deemed as the most important parameter of this study. Altering the phase angle lead to significant changes in the flow field with a response that exhibited high sensitivity to even the smallest increment tested.

The modeling results in general appear to be accurate for negative phase angles, or for when the jet bends in the direction of the cross-flow as opposed to vectoring into it. For all the cases where the jet is close to vectoring into the cross-flow, or actually vectoring into it, the models over predict the deflections and the decay rates.

4.4.4: Modeling limitations and blockage effects

The results from the previous sections revealed that for cases in which the jet was vectored into the cross-flow the predicted results differed from the measured results. The trajectory deflection angle as predicted by the CFD and measured by experiments are shown below in Figure 95 for several phase angles. The angles are measured with respect to the positive *x*-axis. The results indicate that modeling and prediction results are very close to one another until a phase angle of approximately 30°. Going from 30° to 60° the error in the model increases from 5% to almost 12%. This phase angle marks the transition from where the modeling results begin to deviate from experiments due to incorrect estimation of blockage.

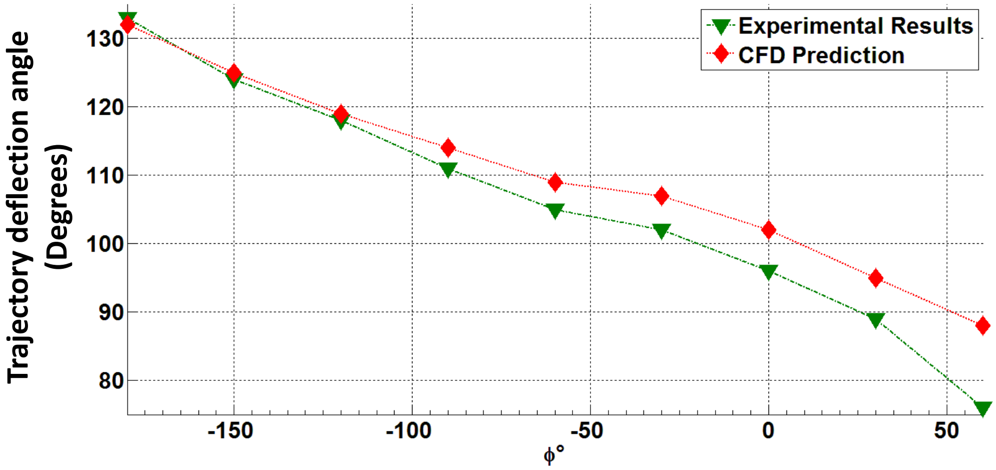

Figure 95 Modeling predictions vs. experimental results for initial jet trajectory deflection angle

When a 3D cross-flow encounters a synthetic jet, it causes it to deflect. This process is referred to as the blockage effect of the cross-flow exerted on the jet. It causes the jet trajectory to deflect in the streamwise direction. As the cross-flow first encounters the SJA, two things happen: (a) part of the cross-flow is entrained by the jet and is responsible for formation of the jet (b) the remainder of the cross-flow will be deflected around the jet or above it. The decreased accuracy in prediction for increasing deflection angle hint as to how the blockage effect is responsible for the degradation of the modeling results. As the jet vectors into the cross-flow, more of the flow tends to deflect around it as opposed to going above it. Since all the models are 2D they do not account for this dimension of flow. By simple conservation principles the 2D models predict that all of the deflected fluid must be deflected over the jet it, resulting in an over prediction of jet deflection. This effect is proportional to the amount of cross-flow that is displaced by the jet, which increases as the jet vectors into the cross-flow. Therefore the accuracy of the predictions deteriorate for all cases in which the jet vectors increasingly into the cross-flow. These cases include positive phase angles and high velocity ratios.

4.4.5: Dynamic virtual shaping through phasing

One of the original goals of the project was to identify array parameters that were suitable for dynamic virtual shaping. The results of the validation section indicated the flow field exhibits high sensitivity to the relative phase angle. The effect of phase angle for purposes of virtual shaping was thus investigated. The time averaged streamlines were plotted as a function of three different phase angles.

Three significantly different flow field patterns are observed for the three different phase angles. Staring with Figure 96 (a) for the case where the phase angle was 0° the effect of actuation was to deflect streamlines away from the surface of the plate. For the case where the phase angle is -90°, shown in (b), the streamlines do not project or deflect into the cross-flow. Instead they are pulled closer to the surface, indicating the jet is not displacing the cross-flow as much as it was for the 0° case. Finally in (c), the case for which the phase angle is -180° we observe that the streamlines are pulled even closer to the surface. In qualitative terms the deflection over a 15 mm span of streamwise distance goes from (a) greater than 20 mm away from the surface (b) between 10 mm and 20 mm away from the surface (c) less than 10 mm from the surface of the flat plate over actuation is performed. This modification in apparent shape was achieved only by manipulating the relative phase of operation as opposed to geometric modifications.

The streamline plots indicate that an array of two actuators can allow for shape control over any aerodynamic surface. For the cases studied changing the phase resulted in different patterns of displacement of streamlines. While the exact nature of this effect would depend on the nature of the application and the aerodynamic surface that the jets are applied to for the flat plate studied, phasing created an effect similar to that of thickening the aerodynamic profile of the plate by displacing streamlines away from it. The amount by which this profile thickens can depended on the particular phase angle used between the two actuators forming the array.

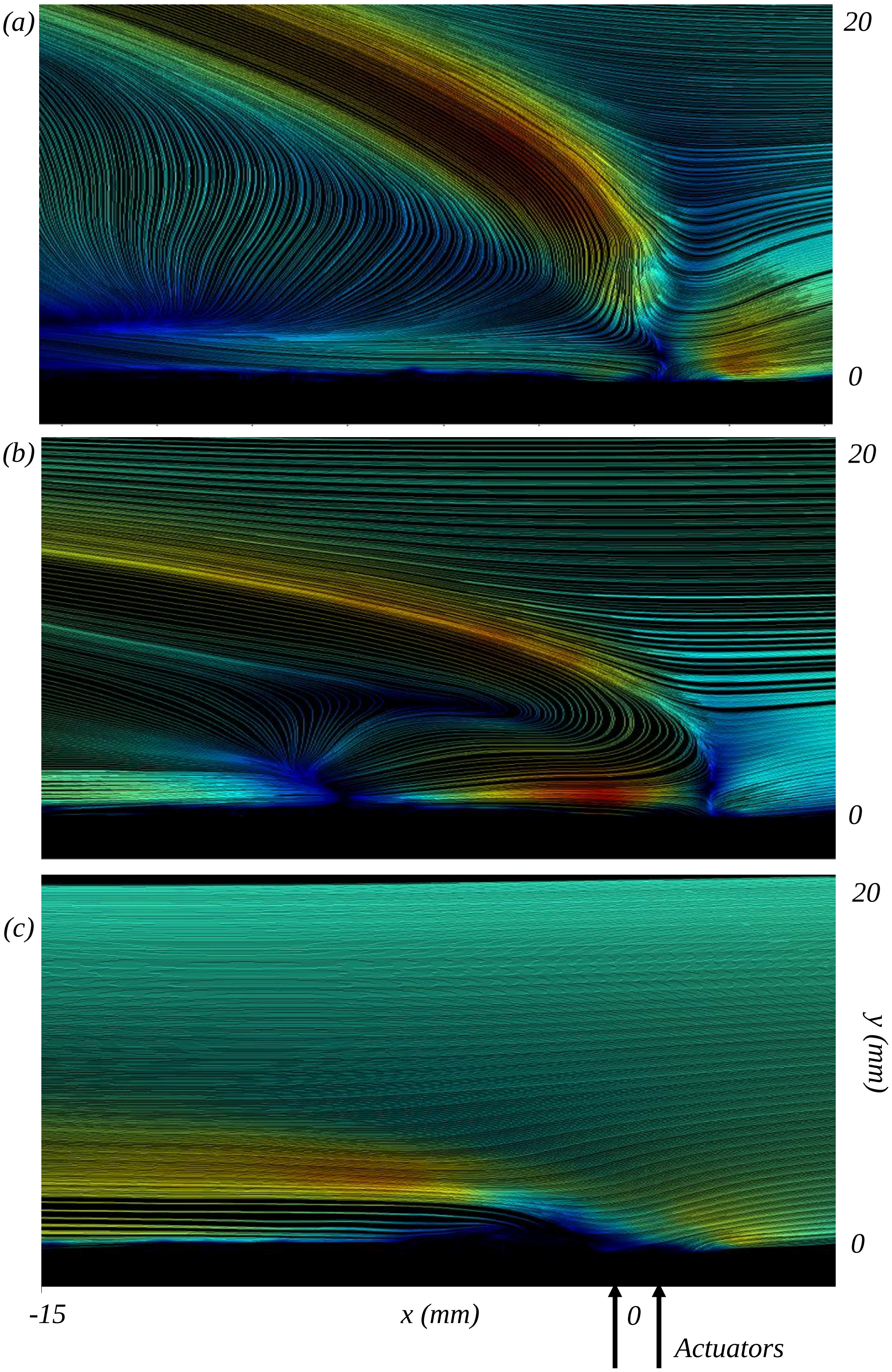

Figure 96 Streamlines for R = 2.4, s = 2.5b and φ = (a) 0° (b) -90° and (c) -180°

4.5 Summary of model validation and experimental analysis

Quiescent and cross-flow synthetic jet actuator flow fields were characterized to validate the models studied in Chapter 2. PIV measurements were first validated against hotwire results, then used to establish the 2D nature of the synthetic jet. PIV was then used to validate the three models. The results indicated that the CFD and perturbation model perform well for cases in which the jet deflection is in the direction of the cross-flow. The analytical solution to the perturbation model worked well for only a limited set of phase angles and velocity ratios. All three models predicted the centerline trajectory reasonably well until heights of 8*b* and below for negative phase angles. Past that point the CFD solution was the only prediction that worked with reasonable accuracy.

The experimental results also validated the model prediction for increased momentum coefficient at specific values of the parameters. This increase was significant because it demonstrated that the interaction of the two jets can be used to enhance their individual performance. Increases of up to 30% were seen.

The analysis revealed the phase angle to be the most significant parameter for control over the flow field. Altering the phase led to significantly different flow fields in terms of magnitude as well as deflection of streamlines.

Chapter 5: Summary, Conclusions and Future Work

5.1 Summary and conclusions

5.1.1: Summary of contribution to the field

The major contributions of this research to the fields of experimental research and modeling techniques for SJA can be summarized as follows:

1) Predicting array behavior through modeling

While several modeling studies detailing the flow fields of single SJA exist, knowledge on how an array of SJA interacts with cross-flow is limited. The flow physics associated with the interaction of two synthetic jet actuators operating in cross-flow conditions was therefore analyzed using three different modeling techniques. 2D unsteady CFD was used to demonstrate that phenomenon such as vortex splitting and switching governed the dynamics of the flow. Based on literature review three parameters were identified as being critical in characterizing the array behavior. Models were used to study the sensitivity of important flow field features to these geometric and operating parameters. Limits under which the developed models were deemed accurate were also established and explained. An analytic solution with appropriate boundary conditions was also calculated and validated. While limited in accuracy and range of operating conditions, this solution can be used for closed loop control application. The developed analytical solution also the potential of being applied to more complicated flow fields with more than two actuators.

2) Developing and characterizing Synthetic Jet Actuators suitable for array use

The literature search revealed several designs for SJA that had been used to study the interaction of single jets with cross-flows. These designs however, were not suited for purposes of array implementation due to geometric constraints. A low cost finite span high aspect ratio (Sahni, et al., 2011) actuator that would satisfy the geometric constrains of array implementation as well as the modeling requirements of 2D flow was developed. Constant Temperature Anemometry was initially used to study the jet and characterize it for frequency and voltage response. The CTA data was then used to validate Particle Image Velocimetry results. PIV was subsequently used to establish the 2D nature of the jet to confirm that the SJA was 2 dimensional.

3) Model validation and enhancement through array operation

The field of flow control through SJA has been well studied from an application point of view. While there exist several studies that detail the physics of single SJA interaction with cross-flows, research on experimental analysis of the physics is lacking. PIV experiments were initially used to validate and establish bounds of operating ranges for the modeling techniques. These results also facilitated in understanding the time averaged characteristics of SJA array flow fields. Modeling and PIV results revealed that it was possible to control the amount of momentum that an array adds to a cross-flow. The benefits of array configuration were demonstrated through improved efficiency of actuators when operating under array conditions. Up to 30% increase in performance was measured. The experimental results verified that for an array of synthetic jets tuning the geometric and operating parameters appropriately would lead to an improvement in the momentum coefficient. A sensitivity study performed on arrays indicated that altering the relative phase of operation had the most impact on the flow field.

4) Demonstration of array operation for dynamic virtual shape control

Chatlynne et al. (Chatlynne, et al., 2001) first demonstrated the ability to virtually shape flow over aerodynamic bodies through SJA and passive obstructions. While they demonstrated that the lift and drag characteristics of a flow could be altered through actuation their work did not focus on using the SJAs to achieve dynamic shape control. Experimental results were used to study the effect of actuation on stream line displacement as function of phase angle. The results indicated that the streamline pattern could be altered significantly without having to alter any of the geometric parameters or adding passive obstructions.

5.1.2: Modeling summary and comparison, conclusions and limitations

The unsteady 2D turbulent CFD modeling method was the most accurate of the three models over all conditions. For a phase angle range of between -180° and -30° it predicted features such as the location of the centerline trajectory to within 10% for heights less than 10 mm (20*b*). Within this range of phase angle it also predicted the momentum coefficient with reasonable accuracy for most test cases. For cases in which the jet was deflecting in the direction of the cross-flow to a higher degree (e.g. high velocity ratio or negative phase angles) the CFD also predicted the decay rates most accurately. Since CFD has been established as a reliable model for SJA flow field prediction the technique was used to study and understand the response in terms of flow features. Li and Sahni (Li & Sahni, 2014) determined in order to characterize the interaction of a synthetic jet with the surrounding flow field it was essential to understand the vortex interaction. CFD was used to qualitatively analyze the time history of the vorticity field for a single actuator and an array of two actuators. The qualitative results predicted that the interaction of the vorticity field for an array could lead to performance enhancement or degradation. The results of Li and Sahni demonstrated that vortex switching played a role in how the flow field developed and behaved in terms of magnitude and frequency characteristics. The CFD results showed that this phenomenon was also responsible for altering the impedance that the flow coming out of the orifice encounters. The CFD model also used to establish the sensitivity of the flow field to the parameters.

While the CFD model produced the most accurate results it was the most resource intensive technique available. Despite the 2D flow field assumption the simulations took between 7-10 days each to complete when run for 350 actuation cycles on a desktop machine with 32 cores and 32 GB of available memory was utilized. The high resolution of the mesh inside & close to the cavity and nozzle placed the heaviest demand for computational requirements.

The 2D CFD was simplified by solving the Navier Stokes equations in terms of the stream and vorticity formulation. In addition to this instead of modeling the entire cavity the actuator was modeled as an orifice nozzle with a time periodic perturbation applied to it. The precise velocity values needed to determine the appropriate perturbation were obtained from the full cavity CFD model. Removing the two cavities reduced the mesh points by approximately 24%. In addition to a reduction in number points, since the solution involved computation of two unknowns (stream and vorticity) it was much faster to computer in comparison to the turbulent, 2D unsteady CFD. The disadvantage of this method was that the physics was modeled to a lesser degree of accuracy since the interaction is turbulent in nature. The simplification however leads to much faster computation time, in some cases up to an order of magnitude in comparison to the turbulent CFD. On average each case took approximately 26 hours to complete. Results from the perturbation assumption were very similar to that of the full CFD for the cases of negative phase angles. In general it was less accurate than modeling the entire cavity flow, but for quantities such as momentum coefficient, the results were in better agreement with the experimental values than those calculated through full CFD. The flow features predicted by the perturbation solution were similar to that predicted by the full CFD close to the orifice. Further away from it, differences were seen indicating that the turbulence effects breakdown and advection of the vortices predicted by the two methods. Also while similar shape of the structures was observed for both models, the strength as predicted by the two methods was slightly different.

The perturbation solution predicted the momentum coefficient results to within 10% for phase angles of -180°, -150°,-60°,-30° and 0°. It also tracked the jet trajectory to within 15% for heights of 10 mm (20*b*) or less for most negative phase angles. For the lower velocity ratio of R = 0.95 the method predicted the location of the centerline trajectory as accurately as the full CFD. The decay rates were also predicted with less than 12% error for this velocity ratio. Like the full CFD the perturbation assumption solution worked best for cases in which the deflection of the jet was in the direction of the cross-flow. For phase angles of 0° or above the modeling predictions diverge from the experimental results due to over predicted blockage. As the jet deflects into the cross-flow, more of it deflects around the jet as opposed to over it. This out of plane flow reduces the actual blockage that the jet experiences for the experimental case. The experimental data for $\varphi > 0°$ therefore cannot be compared to the models in a quantitative sense. Model validation and flow field analysis was thus limited to cases for appropriate phase angles.

In addition to the two numerical methods an analytical solution to the stream and vorticity equations was developed. This solution was based on a time periodic perturbation flow linearly imposed on a laminar cross-flow. The strength of the perturbation varied through the flow field based upon the boundary conditions. The effect of the actuators was modeled as a spatially distributed sinusoid. The magnitude, amplitude of the velocity components were determined through experimental and CFD modeling results.

The results predicted by the analytical solution agreed with the experimental results for specific set of parameters in general. Like the CFD and perturbation solutions, parameters that correspond to jet deflection in the direction of the cross-flow (e.g. $R = 0.95$ or $\varphi = -180°$) corresponded to better predictions for the modeling results. For the general case of all values of parameters if the phase angle was less than 0° the analytical solution was within 15% of the actual measured trajectory for heights less than 5 mm (10*b*).

All three models were subject to limitations in terms of phase angle and velocity ratio over which they were accurate, due to blockage. However the accuracy of each model varied in comparison to one another due to variation in the fundamental information these models require to work. The CFD used boundary conditions that are obtained directly from experimental results that were measured with a highly accurate laser displacement sensor. The perturbation model uses information from the CFD model. The analytical model relies on both the CFD and the PIV for its boundary conditions. The accuracy of each of these models relative to one another, depends on these boundary conditions.

In general the CFD was the most accurate, followed by the perturbation assumption and the analytical solution. This is because of the quality of the available empirical data used as the boundary condition for each of the models. The CFD was provided with boundary conditions that were directly measured using laser displacement methods. The CFD was then used to estimate what the velocity magnitude boundary condition for the perturbation assumption should be, as measurements inside the cavity nozzle were not possible. Since the CFD was setup with an actual measured value of velocity the resultant output velocity at the nozzle was more accurate in comparison to the perturbation assumption, which used a calculated value as a boundary condition. The analytical model required even more empirical information which therefore led to an error that was governed by the accuracy of this available data. The purpose of the modeling was to obtain a solution to the flow behavior that required as little empirical information as possible.

The relation between accuracy of the models and the amount of empirical information they require suggests that sensitivity of the models to the boundary conditions is of some concern. The main focus of this project was to understand and predict the underlying physics of interaction which all three models can do albeit in a limited sense. Improving the boundary conditions provided to each of the models would most definitely improve the results in a very limited capacity. The inaccuracies in the models begin to increase as the jet begins to vector in the +*x* direction (into the cross-flow). For deflections in the -*x* direction inaccuracies are small (in the direction of the cross-flow). This suggests the mechanism that is responsible for the deterioration of accuracy for all models is one that is not dependent on the boundary conditions. A sensitivity analysis to each of the models could be used to improve the accuracy marginally, however the physics that is responsible for the loss in accuracy would not be addressed by such an analysis. The contribution of such an analysis is therefore not in line with the objectives outlined in Section 1.7.

In addition to the differences induced by the boundary conditions, all three models differ slightly in the way calculate the flow field. The full CFD and perturbation assumption are viscous non-linear solutions, whereas the analytical solution is a viscous but linearized solution. The effect of this linearization is to limit the spatial extent over which solution is accurate. In order to expand the region over which the solution would be reliable, a solution technique similar to that of Schroeder and Fleeter (Schroeder, et al., 1989) can be implemented. A localized solution over a small region can be calculated. This process can be repeated for the entire flow field with each localized solution satisfying a small "cell" of the flow field "grid". The global solution can then be calculated by assembling the locally linearized solutions and applying the appropriate boundary conditions.

5.1.3: Experimental results and conclusions

CTA and PIV experiments were used to characterize and validate the mode predicted SJA flow field characteristics. The validation process revealed that modeling results were accurate for flow field cases in which the jets were vectored into the cross-flow. The explanation of why this happened can be given in terms of the blockage effect of the cross-flow as exerted on the jet. For a 2D flow there is no out of plane motion of the fluid. Any cross-flow that comes in the direction of the jet therefore has to either be entrained by it, or go over it. A 3D cross-flow is not subject to this limitation. The approaching cross-flow can either be entrained by the jet, it can deflect over it or it may go around it (out of plane motion). Since the 2D models do not account for this any case of parameters for which the jet deflects into the cross-flow will experience higher than actual blockage, and in turn results in smaller than actual deflection.

The experimental results also validated the two most important conclusions of the modeling section. The first being that array operation under the right set of parameters could lead to improved efficiency. The second one was that the relative phase of operation had the most influence over the SJA flow field. By altering this parameter it was possible to increase or decrease the momentum flux of an array of actuators, as well as control the direction in which the jet plume would develop.

Finally the experimental results were used to produce time averaged streamline plots. These plots indicated that by altering just the phase of operation, it was possible to significantly alter the streamline pattern over a flat plate. This result is important because it allows for dynamic virtual shape control i.e. allowing for modification of the apparent shape of an aerodynamic body without having to alter any geometric characteristics.

5.2 Future work

The modeling techniques that were used for this study were developed based on constraints that were put in place by computational resources. Ideally a full 3D unsteady turbulent CFD model would be desirable to study the complete SJA array flow field development. However with such a large and resource intensive model it would not be possible to study the response over the desired parameter space. 2D CFD was therefore initially used. The ultimate goal in modeling SJA arrays would be to have a pure analytical model that would have no empirical dependency, and that would allow us to accurately capture the effect of all parameters over any range of values. The analytical model and boundary conditions that were developed here was a first step towards that. It can be improved by modifying the boundary condition function to allow for modeling an array of more than two actuators. In addition to this the model can be improved to capture the blockage effect of the cross-flow more accurately. The way this could be achieved is through modifying the $\bar{U}\bar{y}$ term in Equation 26 (a). In its current form the equation predicts that the effect of actuation is that of a periodic perturbation that decays in time superimposed on a uniform cross-flow. By modifying the $\bar{U}\bar{y}$ term to account for out of plane losses, the blockage effect of the cross-flow can be modeled more accurately. This would require establishing the exact spatial dependency of the cross-flow on the parameter space. Once available this information could be used to calculate a blockage correction function that can then applied to the general case. Since the formulation of this solution is based on the stream and vorticity equations, solutions exist only in 2D. Certain assumptions can be utilized to model an axisymmetric 3D case, however that would not capture the 3D physics of the out of plane motion of the cross-flow.

Analytical models are mainly important because any use of synthetic jet arrays for closed loop control would require that the plant dynamics of the array be prescribed in closed loop form. This is a necessity which can only be satisfied only through analytical analysis. The model results can be used to formulate a transfer function that would provide information such as magnitude and direction of momentum flux for any given input of actuator operating conditions. This transfer function can then be used to design a controller for flow control processes such as separation mitigation and dynamic virtual shaping.

In addition to improving the versatility of the models, it is also important to accurately validate them. Based on the observations of the validation section, it would be desirable to stop the cross-flow from being able to deflect away from the center span location. This can be achieved through the installation of fences at the orifice ends. Fence installation would result in cross-flow physics that would be closer to that predicted by the models. In addition to making the physics more amenable it would be invaluable to understand the time accurate/transient response of the flow field experimentally. For the purposes of this study global time averaged data was collected and presented as a function of various geometry and operational parameters. To obtain a better understanding of the transient behavior it would be necessary to obtain phase locked information of synthetic jet flow fields and their dependency on parameters. Phase locked PIV can be used to study these properties. This information could also be used to validate the flow features and their behavior that was observed in section 2.3.1.

The three parameters that were selected as controls for this study were chosen from a space that consisted of more than 8 degrees of freedom. Studying other variables from this space could reveal how SJA flow fields develop in 3D over distances larger than the ones considered for this study. Parameters such as yaw angle with respect to cross-flow have been studied previously in relation to single SJA cross-flow behavior.

Studying one such parameter and characterizing array flow field dependency on it would be an important step towards understanding the 3D SJA array flows.

Finally this project demonstrated the viability of SJA for dynamic shape control and identified an operational parameter that had significant influence over the flow field. Studying the effect of an array of SJAs over the pressure distribution of an aerodynamic body would make for an excellent analysis to complement this research.

Appendices

A1: Error analysis for PIV

The uncertainty associated with the PIV data that was presented was calculated through method of propagation of uncertainty. According to studies[1] the uncertainty associated with PIV techniques similar to the one used for this study is 0.1 pixels. In other words the system is only able to resolve the location of a particle with a maximum of accuracy of 0.1 pixels. In addition to that the PIV system had an uncertainty associated with the time duration between the two pulses of light that were used to illuminate the flow. This was measured to be less than 1 μs. The velocity is then calculated as:

$$V = \frac{\Delta Pixel}{\Delta t} \tag{A.1.1}$$

Where $\Delta Pixel$ is the pixel shift between the two frames of the image pair and Δt is the time duration between the two frames. The uncertainty in the calculated velocity is therefore a function of the uncertainties in the pixel shift and the time duration. The units of the velocity calculated in Eq. A.1.1 are pixels/s which must be converted to m/s. In order to do that a calibration was performed before the experiments were conducted. The calibration relates the shift in pixels to displacement in m. There is an uncertainty associated with this calibration however it is small compared to uncertainty associated with other aspects of the experiments. For the purpose of this calculation it is therefore ignored. Using the method of propagation of uncertainty we can calculate the uncertainty associated with V, as:

---

[1] Adrian, R. J., and Westerweel, J., Particle Image Velocimetry, Cambridge Aerospace Series, New York, 2012

$$\delta V = \sqrt{(\frac{1}{\Delta t})^2 * (\delta\Delta Pixel)^2 + \left(-\frac{\Delta Pixel}{\Delta t^2}\right)^2 * (\delta\Delta t)^2} \tag{A.1.2}$$

Where the δX denotes the uncertainty associated in measuring any quantity X. Using the definition of the momentum coefficient from Eq. 3, and is given as:

$$\delta C_\mu = \sqrt{(2\alpha)^2 * \delta {U_J}^2 + \left(-2\alpha * \frac{U_J}{U}\right)^2 * \delta U^2} \tag{A.1.3}$$

Where $\alpha = n * \left(\frac{b}{c}\right) * (U_J/U^2)$. Using Eq. A.1.1 through Eq. A.1.3 and the values of all the quantities involved in these equations, a worse case combination was identified and used to calculate the maximum possible uncertainty associated with the momentum coefficient.

A2: Calculating array momentum coefficient from experimental data

Calculating the momentum coefficient in accordance to the classical definition requires knowledge of the spatial and temporal distribution of the velocity at the orifice. The CTA or PIV did not have the adequate spatial and temporal resolution and therefore a modified approach to calculating the array momentum coefficient was taken. The jet centerline trajectory was first identified as the locus of points inside the plume that had maximum velocity. In order to obtain a smoother curve a sweep was performed for all *x* values at a fixed height *y* for points located inside the plume. The sweep identified 5 points (corresponding to 2*b*, the length scale associated with the two orifices) at a time, across which the average velocity was calculated. The set of points with the highest average velocity was then used to calculate an average *x*-location of the jet centerline trajectory for the specific *y*. The sweep was then performed for all *y* within the plume. The process is illustrated in Figure A.2.1. Once the centerline trajectory was identified along with the velocity values at various locations along it, U_J was selected as the maximum value in the plume.

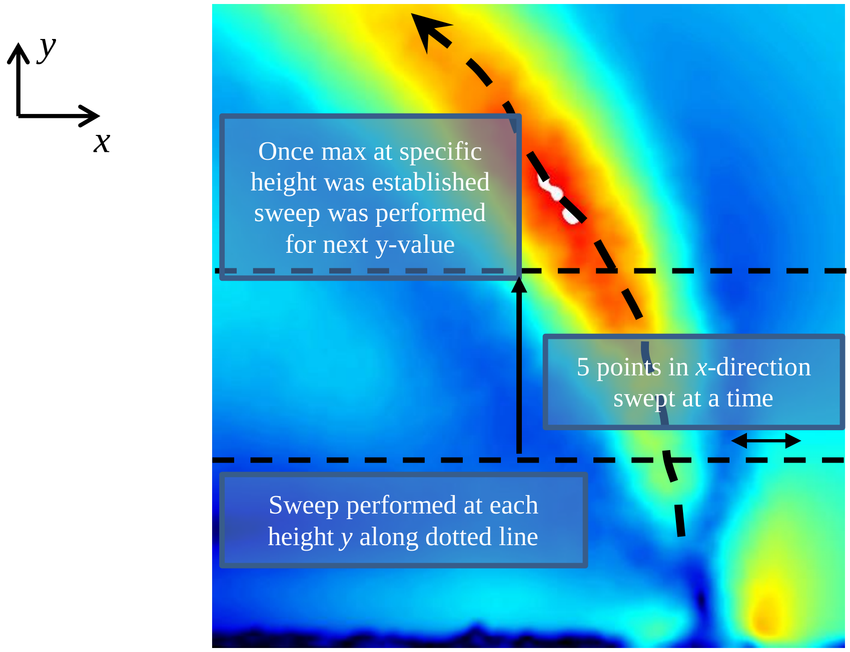

Figure A.2.1 Schematic illustration of algorithm to identify centerline trajectory and average jet velocity for momentum coefficient calculations

The unsteady effects on the momentum coefficient are strongest at the orifice and as we move away, they decay rapidly. This is why the time average velocity increases initially as we move away from the orifice. The momentum coefficient was calculated at a height of at least 3 mm or above the where the effects are small. This specific height was chosen based on CTA analysis of PIV results. The results of this analysis showed that PIV error due to surface reflections was mitigated significantly for heights of 3 mm and above.

A3: Applying synthetic jets in the real world

The application of synthetic jets to aircraft surfaces (and other aerodynamic bodies) has been the subject of many studies. The conditions under which their influence has been studied however, were limited to ground testing or flight simulation analysis. Boeing and NASA (Warwick, 2013) were the first to demonstrate the applicability of a SJA technology to a full size aircraft control surface. They are currently in the process of demonstrating SJA applicability on a full size 757 aircraft. The process faces some obstacles that are encountered by similar technology as it transitions from the lab to the real world e.g. impact of the environment on the technology. For SJA technology initially the biggest hurdle was power requirements. The actuating surface usually comprises of a piezo-metal composite, with the piezo being the driver. Piezoceramic drivers require high voltage to operate which usually requires heavy electrical equipment. More recently this problem has been addressed due to the advent of light weight op-amp circuits that can produce the required high voltage.

There is also a serious concern regarding the usage of SJA under high moisture conditions. When applied to a full scale aircraft that is under actual flight conditions, it is possible for the aircraft to encounter conditions under which moisture may affect the performance of the SJA. Such conditions may include the aircraft flying through a patch of rain, or in a region where there is high humidity there will be condensation as the aircraft ascends. Under these circumstances the moisture may affect the performance in several ways. If a piezoceramic actuator is used, moisture could possibly short the device rendering it useless altogether. Such a condition can however be avoided through reinforcing the seal inside the cavity. However there is still a distinct possibility that there may be accumulation of moisture inside the cavity itself. The impact of any such accumulation would depend on the amount. If the volume of water inside the cavity is comparable to the dimensions of the cavity it would alter the frequency characteristics of the device significantly. The flow inside the SJA would now be a multiphase flow and would require a completely different analysis for predicting the response of the system. It is possible that for SJA of geometries similar to what were used in this study moisture may not be an issue based on the small size of the orifice opening. Nonetheless it is a concern that warrants some thought and analysis before the technology can be applied to actual aircraft.

Bibliography

Amitay, M., Smith, B. L. & Glezer, A., 1998. *Aerodynamic Flow Control Using Synthetic Jet Technology*. s.l., AIAA Paper 98-208.

Amitay, M. et al., 2001. Aerodynamic flow control over an unconventional airfoil using synthetic jet actuators. *AIAA Journal*, 39(3), pp. 361-370.

Amitay, M., Washburn, A. E., Anders, S. G. & Parekh, D. E., 2004. Active Flow Control on the Stingray Uninhabited Air Vehicle: Transient Behavior. *AIAA Journal*, 42(11), pp. 2205-2216.

Bhatt, S. et al., 2014. *Design, Modeling and Testing of Synthetic Jet Actuators for MAV Flight Control*. National Harbor, MD, 52nd Aerospace Sciences Meeting AIAA Sci-Tech.

Bottomley, M. & Packwood, A., 2014. *Experimental Investigation of High-Frequency-Actuation Synthetic Jet Flow Control*. National Harbor, MD, 52nd Aerospace Sciences Meeting AIAA Sci-Tech.

Campbell, J. & Schetz, J., 1972. Flow Properties of Submerged Heated Effluents in Waterway. *AIAA Journal*, pp. Paper 72-79.

Chatlynne, E., Rumigny, N., Amitay, M. & Glezer, A., 2001. *Virtual aero-shaping of a Clark-Y airfoil using synthetic jet actuators*. Reno, NV, AIAA, p. 0732.

Courta, A. & Leclerc, C., 2013. Characterization of synthetic jet actuation with application to Ahmed body wake. *Sensors and Actuators A: Physical*, 192(1), pp. 13-26.

DeMauro, E. P., Leong, C. M. & Amitay, M., 2013. Interaction of a synthetic jet with the flow over a low aspect ratio cylinder. *Physics of Fluids*, 25(6), pp. 64-104.

Feng, L.-H. & Wang, J.-J., 2014. The virtual aeroshaping enhancement by synthetic jets with variable suction and blowing cycles. *Physics of Fluids,* Volume 26.

Flatt, J., 1961. The History of Boundary Layer Control in the United States of America. *Boundary Layer and Flow Control*, pp. 122-143.

Gad-el-Hak, M., 2000. *Flow Control.* Cambridge: The Syndicate of the University of Cambridge.

Gallas, Q. et al., 2003. Lumped Element Modeling of Piezoelectric Driven Synthetic Jet Actuators. *AIAA Journal,* 41(2).

Glezer, A., 1998. United States of America, Patent No. 5758823.

Goh, J. J. & Lee, A., 2013. Investigation of Phasing on Synthetic Jet Actuator Arrays. *Applied Mechanics and Materials,* Volume 465-466, pp. 541-545.

Greenblatt, D. & Wygnanski, I. J., 2000. The Control of Flow Separation by Periodic Excitation. *Progress in Aerospace Sciences,* pp. 487-545.

Greenblatt, D. & Wygnanski, I. J., 2000. The Control of Flow Separation by Periodic Excitation. *Progress in Aerospace Sciences,* pp. 487-545.

Hasnain, Z., Flatau, A. B., Hubbard Jr., J. E. & Mulinti, R., 2012. *Numerical Study and Experimental Validation of the Interaction of Multiple Synthetic Jet Actuators with Cross Flow*. Nashville, TN, 50th AIAA Aerospace Sciences Meeting including the New Horizons Forum and Aerospace Exposition.

Hasnain, Z. et al., 2013. *Experimental Analysis of the Effect of Interaction Parameters on Synthetic Jet Actuator Arrays.* San Diego, CA, AIAA, p. 2475.

Hassan, A., 2005. *On the Benefits of Active Flow Control (AFC) for Low Speed Unmanned Rotorcraft/Aircraft.* Chandler, AZ, AHS.

Hui, W. H., 1987. Exact solution of the unsteady two dimensional Navier Stokes equations. *Journal of Applied Mathematics and Physics,* Volume 38.

Hu, Y., Wu, N. & Liu, H., 2013. Numerical Simulation of Synthetic Jet Actuator and its Controlling Effect on the S-Inlet. *Applied Mechanics and Materials,* Volume 455, pp. 383-388.

Ingard, U. & Labate, S., 1950. Acoustic Circulation Effects and Non-Linear Impedance of the Orifices. *Journal of the Acoustic Society of America Vol. 22, No. 2,* pp. 211-218.

Jabbal, M., Liddle, S., Potts, J. & Crowther, W., 2013. Development of design methodology for a synthetic jet actuator array for flow separation control applications. *Journal of Aerospace Engineering* , 227(1), pp. 110-124.

Jabbal, M., Liddle, S., Potts, J. & Crowther, W., 2013. Development of design methodology for a synthetic jet actuator array for flow separation control applications. *Proceedings of the Institution of Mechanical Engineers, Part G: Journal of Aerospace Engineering,* 227(1), pp. 110-124.

Jee, S. et al., 2013. Simulation of Rapidly Maneuvering Airfoils with Synthetic Jet Acuators. *AIAA Journal,* 51(8), pp. 1883-1897.

Jin, Z., Wang, Y. & Yang, Z., 2014. An experimental investigation into the effect of synthetic jet on the icing process of a water droplet on a cold surface. *International Journal of Heat and Mass Transfer,* pp. 553-558.

Kral, L. D., Donovan, J. F., Cain, A. B. & Cary, A. W., 1997. Numerical simulation of synthetic jet actuators. *AIAA Journal,* pp. Paper No. 1997-1824.

Li, J. & Sahni, O., 2014. *Numerical Investigation of Flow Structures and Interactions due to a Pitched Synthetic Jet in a Laminar Boundary Layer.* National Harbor, MD, AIAA, p. 1140.

LiQun, M. & LiHao, F., 2013. Experimental investigation on control of vortex shedding mode of a circular cylinder using synthetic jets placed at stagnation points. *Science China Technological Services,* 56(1), pp. 158-170.

Mahalingam, R., Glezer, A., Heffington, S. N. & Lutz, R., 2013. *Synthetic Jet Ejector For The Thermal Management of PCI Cards.* USA, Patent No. US20130188307.

Menter, F. R., 1994. Two-Equation Eddy-Viscosity Turbulence Models for Engineering Applications. *AIAA Journal,* 32(8).

Milanovic, I. M. & Zaman, K. B. M. Q., 2005. Synthetic Jets in Cross Flow. *AIAA Jounral,* 43(5), pp. 929-940.

Mittal, R. & Rampunggoon, P., 2001. *Interaction of Synthetic Jet with Flat Plate Boundary Layer.* s.l., s.n.

Montoya, L. D., Jackson, J. L. & Amitay, M., 2010. Control of aerosol dispersion and removal in a room using synthetic jet actuators. *Building and Environment,* 45(1), pp. 165-175.

Nagappan, N., Golubev, V. V. & Habashi, W. G., 2013. *Parametric Analysis of Icing Control Using Synthetic Jet Actuators.* San Diego, CA, AIAA, p. 2453.

Orkwis, P. D. & Filz, C., 2003. *Characterization of Dual Two-Dimensional Synthetic Jets in Cross Flow at Low Mach Number.* Orland, FL, AIAA , p. 3457.

Perkins, C. D. & Hazen, D., 1953. *Some Recent Advances in Boundary Layer and Circulation Control.* s.l., s.n.

Persoons, T., 2012. General Reduced-Order Model to Design and Operate Synthetic Jet Actuators. *AIAA Jounral,* 50(4), pp. 916-927.

Poisson-Quinton, P., 1948. *Recherches Theoriques et Experimentales sur le controle de couche limites.* London, s.n.

Raju, R., Mittal, R. & Cattafesta, L., 2008. Dynamics of Airfoil Serparation Control using Zero-Net-Mass-Flux Forcing. *AIAA Journal,* 46(12), pp. 3103-3116.

Rathay, N., Boucher, M. J., Amitay, M. & Whalen, E., 2014. Performance Enhancement of a Vertical Tail Using Synthetic Jet Actuators. *AIAA Journal,* Volume AIAA Early Edition.

Rathay, N. W., Boucher, M. J., Amitay, M. & Whalen, E., 2014. Performance Enhancement of a Vertical Tail Using Synthetic Jet Actuators. *AIAA Journal.*

Rathnasingham, R. & Breuer, K., 1996. Characteristics of Resonant Actuators for Flow Control. *AIAA Journal,* pp. Paper 96-0311.

Ravachol, M., 1997. *Unstructured finite elements for incompressible flows.* Snow Mass, CO, AIAA.

Rizzetta, D., Visbal, M. & Stanek, M., 1999. Numerical Investigation of Synthetic Jet Flow Fields. *AIAA Journal,* 37(8).

Rumsey, L. C., 2004. *Proceedings of the 2004 Workshop on CFD Validation of Synthetic Jets and Turbulent Separation Control,* s.l.: NASA/CP-2007-214874 .

Sahni, O., Wood, J., Jansen, K. E. & Amitay, M., 2011. Three-dimensional interactions between a finite-span synthetic jet and a crossflow. *Journal of Fluid Mechanics,* pp. 254-287.

Sassoon, A., Hubbard Jr., J. E., Flatau, A. B. & Hasnain, Z., 2013. *Flow Over a Backward Facing Step Subjected to Multiple Synthetic Jet Actuators.* San Diego, CA, AIAA, p. 3166.

Savas, O. & Coles, D., 1985. Coherence Measurements in Synthetic Turbulent Boudary Layers. *Journal of Fluid Mechanics,* p. 421.

Schaeffler, N. W., 2003. *The Interaction of a Synthetic Jet and a Turbulent Boundary Layer*. Reno, NV, AIAA.

Schroeder, L. M., Wolff, J. M. & Fleeter, S., 1989. Locally analytical prediction of the viscous aerodynamics of an oscillating flat plate airfoil. *Mathematical and Computer Modeling,* 12(6), pp. 707-719.

Seifert, A. & Wygnanski, I., 1996. On the Delay of Airfoil Stall by Periodic Excitation. *AIAA Journal,* 33(4), pp. 691-699.

Silva, L. A. & Ortega, A., 2013. Convective Heat Transfer in an Impinging Synthetic Jet: A Numerical Investigation of a Canonical Geometry. *Journal of Heat Transfer,* 135(8).

Smith, B. L. & Glezer, A., 1997. *Vectoring and small-scale motions effected in free shear flows using synthetic jet actuators.* Reno, NV, AIAA.

Smith, B. L. & Glezer, A., 1998. The Formation and Evolution of Synthetic Jets. *Physics of Fluids,* pp. 2281-2298.

Smith, B. L. & Glezer, A., 2005. Vectoring of Adjacent Synthetic Jets. *AIAA Journal,* 43(10), pp. 2117-2124.

Smith, D. R., 2002. Interaction of a Synthetic Jet with a Cross Flow Boundary Layer. *AIAA Jornal*, 40(11), pp. 2277-2288.

Tang, H., Salunkhe, P., Du, J. & Wu, Y., 2014. Active Flow Control Over a Wing Model Using Synthetic-Jet-Actuator Arrays. In: *Fluid-Structure-Sound Interactions and Control.* Berlin: Springer-Verlag Berlin Heidelberg.

Tang, H. & Zhong, S., 2006. Lumped Element Modeling of Synthetic Jet. *AIAA Journal,* pp. Paper 2006-3696.

Tang, S. Q. & Huang, C. Q., 2013. Comparative Study of Synthetic Jet Numerical Simulation Methods. *Applied Mechanics and Materials I,* pp. 486-490.

Ugrina, S., 2007. *Experimental Analysis and Analytical Modeling of Synthetic Jet Cross-Flow Interactions.* s.l.:University of Maryland.

Utturkar, R., Holman, R., Sheplak, M. & Cattafesta, L., 2003. *A Jet Formation Criterion for Synthetic Jet Actuators.* s.l., s.n.

Vasile, J. D. & Amitay, M., 2013. Interactions of an Array of Finite Span Synthetic Jets and a Crossflow. *AIAA Journal*, pp. 2503-2512.

Vazquez, M., Ravachol, M., Chalot, F. & Mallet, M., 2004. The robustness issue on multigrid schemes applied to the Navier-Stokes equations for laminar and turbulent, incompressible and compressible flows. *International Journal for Numerical Methods in Fluids,* Volume 45, pp. 555-579.

Wu, C. & Ahmed, N.-E.-A., 2012. Application of Flow Control Techniques for Indoor Ventilation. *International Energy Congress,* Volume 49, pp. 135-141.

Wu, K. & Breuer, K., 2003. *Dynamics of Synthetic Jet Actuator Arrays for Flow Control.* s.l., AIAA Paper 2003-4257.

Wygnanski, I. J., 1997. *Boundary Layer Flow Control by Periodic Addition of Momentum.* Snowmass Village, CO, AIAA, p. 2117.

Xia, Q. & Zhong, S., 2014. Enhancement of laminar flow mixing using a pair of staggered lateral synthetic jets. *Sensors and Actuators A: Physical,* Volume 207, pp. 75-83.

Yamaleev, N. K., Carpenter, M. H. & Ferguson, F., 2005. Reduced-Order Model for Efficient Simulation of Synthetic Jet Actuators. *AIAA Journal,* 43(2), pp. 357-369.

Yao, C., Chen, F. J., Neuhart, D. & Harris, J., 2004. *Synthetic Jet Flow Field Database for CFD Validation.* Portland, OR, AIAA.

Zelenyak, A. et al., 2013. *Characterization of synthetic jet actuators used for jet noise reduction by flow control.* Pittsburgh, PA: 66th Annual Meeting of the APS Division of Fluid Dynamics .